

PDF hosted at the Radboud Repository of the Radboud University Nijmegen

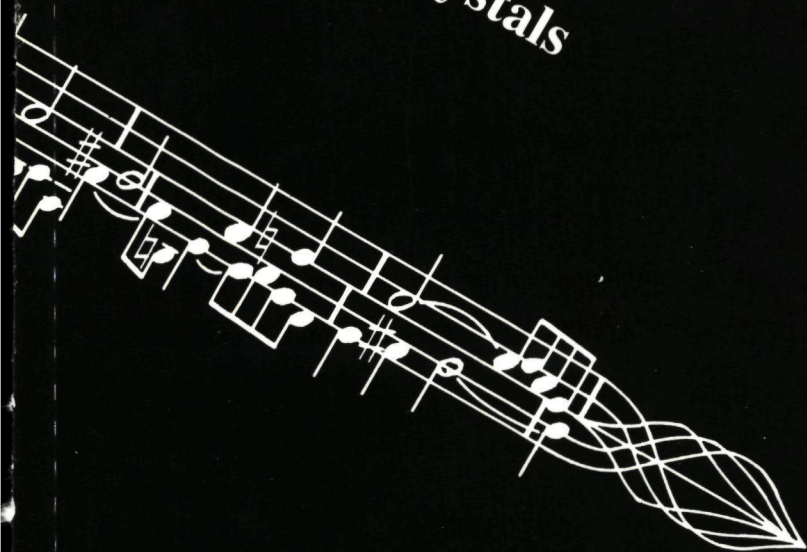
The following full text is a publisher's version.

For additional information about this publication click this link.

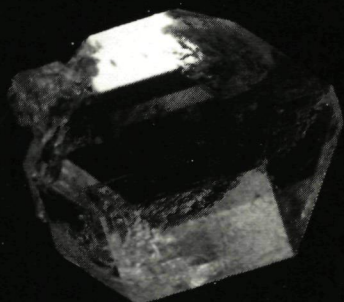
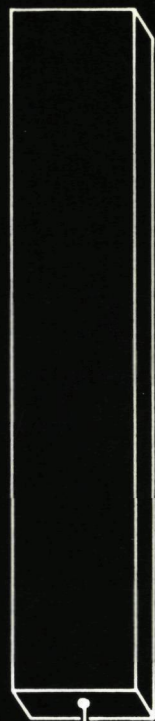
<http://hdl.handle.net/2066/113482>

Please be advised that this information was generated on 2018-07-08 and may be subject to change.

**Optical and Dynamical
Properties of
Modulated Crystals**



Hugo Meekes



**Optical and Dynamical Properties
of Modulated Crystals**

**Optical and Dynamical Properties
of Modulated Crystals**

**een wetenschappelijke proeve op het gebied van
de Wiskunde en Natuurwetenschappen**

Proefschrift

**ter verkrijging van de graad van doctor
aan de Katholieke Universiteit te Nijmegen,
volgens besluit van het College van Decanen
in het openbaar te verdedigen
op dinsdag 23 februari 1988,
des namiddags te 3.30 uur**

door

Hugo Leonard Marie Meekes

**geboren op 15 januari 1959
te Lichtenvoorde**

1988

druk: Krips Repro, Meppel

Promotores:

Prof. Dr. A.G.M. Janner

Prof. Dr. P. Wyder

Co-referent:

Dr. Th.W.J.M. Janssen

Cover:

First eight bars of

Contrapunctus I from *Die Kunst der Fuge* by J.S. Bach (1685 - 1750) (BWV 1080), adapted to obtain an incommensurate modulated fugue with a longitudinal polarisation. The periodicity and amplitude are given by $q \approx 2\pi/17 \text{ bar}^{-1}$ and $A = 0.2 \text{ bar}$, respectively.

Op deze plaats wil ik graag een aantal mensen danken voor hun directe dan wel indirecte bijdrage aan dit proefschrift.

Beginnend binnen de werkomgeving, met name Aloysio voor zijn nimmer aflatende enthousiasme en de vele nieuwe ideeën, Ted voor zijn vaak broodnodige heldere uitleg ook van zaken die ik eigenlijk al behoorde te weten en Peter voor de welgemeende schouder-strikes alsmede het lichtelijk wantrouwende: "Echt waar?".

Riki en Maria dank ik voor alle niet-fysische zaken. Kees, Jan, Jan en Albert voor alle vormen van technische ondersteuning. Erwin en Harrie voor de plezierige samenwerking en Tom voor de foto's.

Hans, George, Jo en Casper voor de vele fysische maar ook andere discussies in het triumviratenhok.

Verder dank ik de mensen van theoretische vaste stof II en die van experimentele natuurkunde IV voor de prettige werksfeer. Vooral de laatsten voor hun aandacht wanneer de koffietafel of sluitingstijd weer eens werden beheerst door verhalen over hoe het nou echt moet volgens de audiofielen.

Het microcanoniek ensemble ben ik dank verschuldigd voor het dulden van al mijn incommensurabele solo's en ritmes.

Tenslotte ben ik alle ondersteunende diensten van de faculteit zeer erkentelijk voor hun verscheidene bijdragen.

Ich danke den Leuten der Festkörperphysik Gruppe von Professor Günter an der Eidgenössische Technische Hochschule Zürich, für ihre Gastfreundschaft. Im besonderen möchte ich meinen Dank aussprechen an Herbert und Marianne Looser für die grosszügige und ungezwungene Art mit welcher sie mich in ihrem Haus aufgenommen haben. Mit viel Genügen denke ich an Diskussionen über Physik und vielen anderen interessanten Fragen die ich mit Enrico Colla gehabt habe.

Buiten de fysica zijn er verschillende mensen die het leven aangenaam maken; hen hoef ik niet bij naam te noemen. Om twee kom ik echter niet heen; mijn ouders dank ik voor hun meeleven op de achtergrond. Aan hen draag ik dit boekje op.

TABLE OF CONTENTS

CHAPTER 1 INTRODUCTION	13
CHAPTER 2 RAMAN AND FAR-INFRARED SPECTROSCOPY ON MODULATED STRUCTURES	19
2.1 Introduction	20
2.2 Raman and infrared spectroscopy	22
2.2.1 Normal Crystals	22
2.2.2 Incommensurate crystals	25
2.3 Experimental set-up	26
2.3.1 Infrared spectroscopy	26
2.3.2 Raman spectroscopy	29
References	32
2.4 Raman and infrared spectra of the incommensurate crystal Na_2CO_3	33
Abstract	33
2.4.1 Introduction	34
2.4.2 The structure of sodium carbonate	35
2.4.3 Experimental	37
2.4.3.1 Crystal preparation	37
2.4.3.2 Raman measurements	38
2.4.3.3 FIR measurements	43
2.4.3.4 Temperature control	44
2.4.4 Interpretation	44
2.4.4.1 Optical activity of the modes	45
2.4.4.2 The internal modes	47
2.4.4.2.1 The ν_1 -internal mode	50
2.4.4.2.2 The ν_2 -internal mode	52
2.4.4.2.3 The ν_3 -internal mode	53
2.4.4.2.4 The ν_4 -internal mode	53
2.4.4.3 The soft modes	54
2.4.4.4 The external modes in the γ phase	58
2.4.4.4.1 The Raman spectra	58
2.4.4.4.2 The FIR spectrum	60
2.4.4.5 The lock-in transition	61

2.4.4.6	The external modes in the δ phase	66
2.4.5	Conclusion	67
	Acknowledgements	69
	References	70
2.5	Raman and infrared studies of $[\text{N}(\text{CH}_3)_4]_2\text{ZnCl}_4$	
	-A normal versus superspace description-	73
	Abstract	73
2.5.1	Introduction	74
2.5.2	Raman and infrared activity	77
2.5.3	Experimental	79
	2.5.3.1 Crystal preparation	79
	2.5.3.2 Raman measurements	79
	2.5.3.3 FIR measurements	82
	2.5.3.4 Indicatrix	83
	2.5.3.5 Temperature control	84
2.5.4	Interpretation	85
	2.5.4.1 The structure of $[\text{N}(\text{CH}_3)_4]_2\text{ZnCl}_4$	85
	2.5.4.2 Raman and infrared activity of the modes	87
	2.5.4.3 Analysis of the spectra	94
	2.5.4.3.1 External modes	94
	2.5.4.3.2 Internal modes	95
	2.5.4.4 The indicatrix in the monoclinic phases	98
2.5.5	Conclusion	102
	Acknowledgements	103
	References	104

CHAPTER 3 OPTICAL ACTIVITY IN INCOMMENSURATE STRUCTURES 107

3.1	Introduction	108
3.2	Optical activity	109
3.3	HAUP polarimeter	111
	References	118
3.4	Optical activity in the incommensurate structure Rb_2ZnBr_4	119
	Abstract	119
	3.4.1 Introduction	120
	3.4.2 Optical activity in Rb_2ZnBr_4	121

3.4.3	Optical symmetry properties in the incommensurate phase	125
3.4.3.1	General	125
3.4.3.2	The dielectric tensor	126
3.4.3.3	Optical activity	134
3.4.4	Experimental	136
3.4.4.1	HAUP polarimeter	136
3.4.4.2	Temperature control	137
3.4.4.3	Samples	137
3.4.4.4	Results and evaluation	138
3.4.5	Discussion	141
3.4.5.1	Rb_2ZnBr_4	141
3.4.5.2	Other A_2BX_4 -compounds	146
3.4.6	Conclusion	147
	Acknowledgements	148
	References	149

CHAPTER 4 POINT-CONTACT SPECTROSCOPY IN INCOMMENSURATE CHROMIUM

151

	Abstract	152
4.1	Introduction	153
4.2	The structure and density of states in chromium	154
4.2.1	The structure of chromium	154
4.2.2	The origin of the SDW	154
4.2.3	Density of states	155
4.3	Point-contact spectroscopy	155
4.4	Experimental	162
4.5	Results and discussion	162
4.6	Conclusion	169
	Acknowledgements	170
	References	171

SUMMARY	173
SAMENVATTING	177
CURRICULUM VITAE	181

CHAPTER 1

INTRODUCTION

In this thesis experimental and theoretical studies concerning some optical and dynamical aspects of modulated structures are presented. These structures involve both commensurate and incommensurate modulated crystals.

All the concepts mentioned above, such as (in)commensurate modulation, crystal, etc. share the property of referring to one or another form of regularity. The study of regularity of matter and especially the search for a description in terms of symmetries for crystals which at first sight are not regularly built, is the main aim of this work. This search is performed by selecting a number of physical properties of these crystals and investigating them in relation with the symmetry of the crystal.

Regularity and symmetry have always been a fascination for men. It is found in numerous ways in nature and probably as a reflection of its beauty, also in all kinds of art. In the beginning just as a pleasure for the eye but later when sciences and art became intimately connected, also as styles ruled by mathematical laws. A well known example of the latter influence is the strict use of the golden section in the architecture and paintings of the renaissance. In music one finds extreme forms of regularity in the fugue, crowned by *Die Kunst der Fuge* (J.S. Bach, BWV 1080).

As many aspects of art and science are strongly influenced by revolutionary changes, also the use of patterns and symmetries knows many different schools. Though each new style in the use of regularity is to a large extent determined by preceding or even very old ones, new ideas concerning the laws of regularity have been very important. In modern music this resulted in styles which for the "conservative" ear have no pattern at all. Often this use of seemingly chaotic styles is very stimulating for the development of mens views on art.

In science these new schools also have led to new insights and understanding of nature. A nice example is the recent interest in chaotic processes, in which scientists have discovered many forms of regularity, unknown until then. A less revolutionary but nevertheless for many scientists astonishing discovery was the one concerning incommensurate crystals.

Until the nineteen sixties crystals were believed to be an appearance of nature, which can be described by three independent fundamental periodicities as a result of a regular space filling with atoms. This in contrast to for example glasses, which have, though being a form of condensed matter, no such regularity. The success of the description of crystals was enormous. One was able to work out a classification of crystals by introducing translational symmetries corresponding to these three periodicities and adding a small number of other symmetries involving mirror and/or rotational operators. All these symmetries together form the space group symmetry

of a crystal. The mathematical frame work in which these space groups are specified, namely group theory, allowed for a classification into a finite number of possible and inequivalent symmetry groups. Practically all crystals found in nature fitted within this frame work of space groups and moreover, the use of this classification allowed for a specification of crystals in the early days by its morphology, later X-ray diffraction patterns and nowadays by numerous experimental techniques.

Incommensurate crystals, however, did not fit within this classification. For example the X-ray diffraction pattern of $\gamma\text{-Na}_2\text{CO}_3$ could not be labeled by the usual indices (h, k, l) , indicating the components of a vector of the reciprocal lattice of the crystal expressed in terms of three fundamental periodicities, without allowing for unrealistic large integers. This compound (and with it, later on, many others as well) was found to have an additional fundamental periodicity for which the atoms were somewhat displaced from the positions in which they would form a normal crystal. Accordingly, one can say that $\gamma\text{-Na}_2\text{CO}_3$ involves four fundamental periodicities. Besides these displacively modulated crystals, also composite incommensurate structures and atomic density modulations were found. Another class of incommensurate modulated structures is the one including charge or spin density wave systems. All these incommensurate crystals had, though a lack of space group symmetry, a very crystalline appearance. Their morphology revealed nice crystal faces and their X-ray diffraction pattern showed the typical sharp Bragg spots. Therefore these structures demanded, so to say, for a description of their symmetry. The answer was found in the so-called superspace groups, introduced by de Wolff and Janner and Janssen. These authors treated the additional periodicities of the modulation, analogously to what is done in the normal case, as new coordinates in a higher $(3 + d)$ dimensional Euclidean space. In this so-called superspace translational symmetry is again present and together with other Euclidean symmetry operators like mirrors and rotations. Analogous to what one has in three dimensions, these superspace groups are capable of describing the morphology and X-ray pattern of incommensurate crystals very elegantly. Instead of the three indices (h, k, l) , one then has e.g. (h, k, l, m) expressing the components of a reciprocal wave vector in terms of four fundamental periodicities in case of a single modulation. In three dimensions one then has $\mathbf{K} = h\mathbf{a}^* + k\mathbf{b}^* + l\mathbf{c}^* + m\mathbf{q}$, where \mathbf{a}^* , \mathbf{b}^* and \mathbf{c}^* refer to the reciprocal lattice vectors of the basic (no modulation) structure and \mathbf{q} is the wave vector of the modulation. Within a few years time, many structures with an incommensurate phase were found. Referring

to the schools in science mentioned above, it is interesting to see that a mineral, namely calaverite ($\text{Au}_{1-x}\text{Ag}_x\text{Te}_2$), very famous in the early days of morphological crystallography, because of the impossibility of indexing its crystal faces in terms of sets of three integers only, more than fifty years later was understood to be incommensurately modulated and therefore, to require four integral indices.

The success of the superspace description for structural investigations on incommensurate crystals led to the study of its consequences for other physical properties of such crystals. For normal crystals the space group symmetry has very profound consequences for many physical properties. These consequences in the case of incommensurate crystals are far from trivial. First of all because of the lack of space group symmetry but moreover, when one uses the superspace description, one has to bear in mind that physical properties are always found in three dimensions, while the symmetry description is in four (or more) dimensions. The use of superspace groups to describe the symmetry of incommensurate crystals, can be extended to include certain commensurate modulated structures. In many cases no differences in physical results between a normal and a superspace description is found. In these cases the usefulness lies in the elegance of the description reducing the number of relevant parameters needed. There are cases, however, where one substance shows many different phases as a function of temperature, which can all be described to a very good approximation by the same superspace group. For the A_2BX_4 -family of dielectrics this even holds for practically all its members. One speaks of a proto-type symmetry. In this case the normal and superspace description can lead to different results as to the restrictions implied by the symmetry on physical properties are concerned.

The use of a proper or adequate symmetry description of crystals is not only important from a fundamental point of view. In addition, the use of many properties of crystalline matter in devices is of great technological importance. For example, optical properties of crystals are often adapted by using coatings or other multi-layer techniques, which have to be controlled very well from an engineer's point of view but also have to be understood very well from a theoretical point of view. Both these demands become more and more important with the sizes of artificial structures becoming smaller. For example, the physical properties of superlattices often can not be simply guessed from extrapolations from more rough structures. Detailed calculations are necessary to reveal or predict the exotic behaviour of such compounds. Knowledge of the right symmetry description of such systems is not only a question of elegance but essential for the proper control of the properties of

the compounds

In this thesis, as was mentioned before, optical and dynamical properties of modulated structures are experimentally studied and analysed in terms of their symmetry. The three remaining chapters include four papers already published or submitted for publication.

In chapter 2 the Raman and infrared phonon spectra of modulated crystals are studied. Typical for a modulation with wave vector \mathbf{q} is the equivalency of wave vectors $\mathbf{k} = n\mathbf{q}$ (n integer) with $\mathbf{k} = 0$, also in the case of an incommensurate crystal. Because of this equivalency phonon modes at $\mathbf{k} = n\mathbf{q}$ become active in Raman or infrared spectra besides the (normal) modes at $\mathbf{k} = 0$. The selection rules for this activity can be found with the (super)space group. The resulting spectra are analysed in the case of Na_2CO_3 . As an example of a proto-type structure, the spectra in all commensurate phases of $[\text{N}(\text{CH}_3)_4]_2\text{ZnCl}_4$ are studied both in a normal and superspace description. The results are compared.

In chapter 3 optical activity in incommensurate structures is the subject. Optical activity (or gyration) is the effect for which the polarisation of light passing a crystal is rotated around the direction of propagation, the rotation angle being proportional to the thickness of the specimen. This effect is studied in the particular case of Rb_2ZnBr_4 . For the incommensurate phase the observed effect is explained in terms of long-wavelength structural contributions to the dielectric and gyration properties. The allowed relevant Fourier components and the symmetry of the corresponding tensors are found with the help of the superspace group of this compound.

In chapter 4 the incommensurate spin density wave in pure chromium is studied by means of point-contact spectroscopy. The resistance of a small Cr-Cr point-contact is found to increase considerably for low applied voltages. This increase is related to additional gaps in the electron density of states, due to the incommensurate spin density wave inducing a corresponding displacive modulation.

CHAPTER 2

RAMAN AND INFRARED SPECTROSCOPY ON MODULATED STRUCTURES

2.1. Introduction

Raman and far-infrared spectroscopy are two techniques which have been proven to be very powerful for studying all kinds of excitations in condensed matter, gasses and liquids. We will concentrate on rotational and vibrational excitations in crystals, in other words on phonons.

Both techniques analyse light which has interacted with excitations of the crystal. This can be done both in transmission and in reflection, while for far-infrared spectroscopy sometimes the absorption is measured as well. As will be explained in the next section, there are selection rules limiting the scattering processes which can take place. These selection rules make these techniques so powerful, because they allow the determination of symmetry properties of the material under study. Roughly speaking, one can say that both Raman and infrared spectroscopy allow to probe the phonons with zero wave vector. Which of these phonons is active depends on the symmetry of the excitation in question and the selection rules express precisely those conditions. These techniques have, in many cases, complementary selection rules. In other words, it is possible that a phonon at $\mathbf{k} = 0$ is Raman active but not active in the infrared and vice versa. These symmetry selective properties are very useful when studying phase transitions which involve symmetry changes: certain modes can be inactive in one phase and become visible in the other.

Often, these phase transitions are driven by so-called soft modes, phonons which on approaching the transition, have a decreasing frequency (grow soft) as a function of temperature and at the transition point provide a static deformation of the crystal. This deformation, then, gives rise to the symmetry changes of the new phase. If the deformation is periodic, one gets a modulated crystal structure. In case of a periodicity which does not fit with the underlying lattice, the crystal is said to be incommensurate.

As modulated and especially incommensurate crystals are concerned, again, the sensitivity to the symmetry of the excitations makes Raman and infrared spectroscopy suited for studying their structure.¹ First of all, because of the lack of a normal space group symmetry in incommensurate phases, it is interesting to find out what are the consequences of the modulation for the excitation spectra. The introduction of superspace groups by de Wolff² and Janner and Janssen,³ provides a description in more than three dimensions with a restored crystallographic symmetry, thus allowing for selection rules, which in incommensurate phases

represent a natural extension of those obtained with normal space groups. An important result of their work is that these superspace groups characterise the symmetry of phonons, in particular those with wave vector $\mathbf{k} = n\mathbf{q}$ (\mathbf{q} is the modulation wave vector and n integer). These latter phonons become, besides the phonons at $\mathbf{k} = 0$, also active in a modulated phase (Janssen⁴). Experimentally this has been verified by Rasing *et al.*,⁵ Echégut *et al.*⁶ and Maciel and Ryan.⁷

Incommensurate modulated phases are often induced by a soft phonon at a general point in the Brillouin zone. This phonon is inactive in both Raman and infrared spectra. In the incommensurate phase, however, two new excitations with wave vector $\mathbf{k} = \mathbf{q}$ arise, the so-called amplitudon and phason, a vibration of the amplitude and the phase of the modulation, respectively. These modes are possibly active due to the equivalency of their wave vectors $\mathbf{k} = n\mathbf{q}$ with $\mathbf{k} = 0$. The phason, however, remains in principle a zero-energy mode throughout the incommensurate phase, growing "hard" near the lock-in phase transition. This latter is a transition to a commensurate (superstructure) phase, which takes place in many of the incommensurate crystals known so far. Raman and infrared techniques are very well suited for studying these new excitations.

The use of superspace groups is not only restricted to incommensurate phases. The symmetry of commensurate modulated superstructures is often equally well and sometimes even better described by superspace groups.^{8,9} Here, we have to distinguish between two cases. The first category involves structures with a lock-in phase which has the same point group symmetry as that of the incommensurate phase. In this case, the superspace group and the normal 3D-space group essentially provide the same symmetry conditions. The usefulness of the superspace group then stems from the simplification of the description due to the smaller amount of parameters needed to describe the structure, in those cases where the modulation wave is not too complex. Obviously, this can be very helpful when one deals with large superstructures.¹⁰

The second case deals with superstructures which have a lower symmetry than that obtained from an (incommensurate) proto-type structure by simply changing the wave length of the modulation. Note that the superspace symmetry of the proto-type is independent of the commensurate or incommensurate character of the modulation. For this kind of phases, often, the actual deformations from this proto-type structure are very small. For many physical properties it is then, to a very good approximation, allowed to use the superspace description for all phases of one compound or even for all structures of one family of isostructural members.

The only parameters that change on going from one crystal phase to another, are the (in)commensurate wave vector \mathbf{q} and the phase of the modulation, the amplitude of the modulation being such that the the symmetry of the structure is not changed. A famous example of this kind of structures is the A_2BX_4 -family of dielectrics.^{11,8}

In sections 2.2 and 2.3 the selection rules in Raman and infrared spectroscopy and the experimental set-up, used in our experiments, are treated respectively. The actual work is thereafter divided in again two sections. The first one (2.4) presents the Raman and infrared spectra of Na_2CO_3 , a crystal for which the symmetry of the incommensurate phase is well known. In that section the complete spectra will be treated in all phases of this compound, including the additional modes at $\mathbf{k} = n\mathbf{q}$, the soft modes and a discussion of the lock-in phase in terms of the superspace group as an exact symmetry description. In section 2.5 the spectra of $[\text{N}(\text{CH}_3)_4]_2\text{ZnCl}_4$ are studied. This compound is an example of a structure with, besides an incommensurate phase, many commensurate phases which have the same (approximate) proto-type symmetry. The relevance of this proto-type symmetry for Raman and infrared spectroscopy is tested.

2.2. Raman and infrared spectroscopy

2.2.1. Normal crystals

In this section we explain how the selection rules for Raman and infrared spectroscopy can be derived using the symmetry of the crystal in question. In both types of spectroscopy the light (visible in the case of Raman and (far)-infrared for infrared spectroscopy) has a wave vector which is much smaller than any nonzero reciprocal lattice vector. Therefore, the light only interacts with excitations (phonons) with wave vectors at the center of the Brillouin zone ($\mathbf{k} \approx 0$). A further restriction on the interaction process stems from the symmetry of the excitation together with the experimental orientation of the crystal with respect to the propagation direction and polarisation of the light.¹²

In the case of infrared spectroscopy the activity of a certain phonon mode depends on the transition matrix element which involves the dipole moment of the mode in question and the electric field of the light. For normal temperatures only

transitions from the ground state to the first excited state, a fundamental transition, are relevant. In the harmonic approximation, this leads to absorption of radiation by phonons with energy $\epsilon = \hbar\omega$, where ω is the frequency of the mode. This absorption can only take place if the normal coordinates of the mode allow for an electric dipole moment. Therefore, this dipole moment \mathbf{m} is expanded about the equilibrium configuration in a Taylor's series in the normal coordinates $Q_{\mathbf{k}}$

$$\mathbf{m} = \mathbf{m}_0 + \sum_{\mathbf{k}} \left[\frac{\partial \mathbf{m}}{\partial Q_{\mathbf{k}}} \right]_0 Q_{\mathbf{k}} + \dots \quad (2-1)$$

A transition can take place if $\partial \mathbf{m} / \partial Q_{\mathbf{k}}$ is different from zero. This restriction is the same as demanding that the corresponding normal mode transforms under the symmetry group (i.e. the point group for modes at $\mathbf{k} = 0$) of the crystal, according to a component of the vector representation. In general there are three (or less when the symmetry is high enough for degeneracy to occur) relevant representations, corresponding to modes with dipole moments along three independent directions. A distinction between any of these different modes can be obtained by using polarised light.

In the case of Raman scattering, the radiation induces a dipole moment via the polarisability of the medium. This resulting dipole acts as a radiating source for the scattered light leaving the crystal. In this case, the polarisability tensor α is expanded in a Taylor series in the normal coordinates:

$$\alpha = \alpha_0 + \sum_{\mathbf{k}} \left[\frac{\partial \alpha}{\partial Q_{\mathbf{k}}} \right]_0 Q_{\mathbf{k}} + \dots, \quad (2-2)$$

and the dipole moment becomes

$$\mathbf{m} = \alpha \epsilon = \alpha_0 \epsilon + \sum_{\mathbf{k}} \left[\frac{\partial \alpha}{\partial Q_{\mathbf{k}}} \right]_0 A_{\mathbf{k}} \epsilon_0 e^{2\pi i (\mathbf{K} \pm \mathbf{k}) \cdot \mathbf{r}} e^{i(\omega_{\mathbf{K}} \mp \omega_{\mathbf{k}})t} + \dots, \quad (2-3)$$

for an exciting field of the form $\epsilon = \epsilon_0 e^{2\pi i \mathbf{K} \cdot \mathbf{r} - i\omega_{\mathbf{K}} t}$. $A_{\mathbf{k}}$ is the amplitude of the normal mode $Q_{\mathbf{k}}$. Thus, a radiating dipole with frequency $(\omega_{\mathbf{K}} \pm \omega_{\mathbf{k}})$ is induced. The corresponding quantum mechanical processes are the creation and annihilation of a phonon. They are designated as Stokes and anti-Stokes, respectively. The result is a light wave leaving the crystal with a slight shift in energy (as $\omega_{\mathbf{k}} \ll \omega_{\mathbf{K}}$). The wave vector of this dipole field is for a scattering geometry of 90° (the angle between the excited and scattered radiation) $k = \sqrt{2K}$, because the wave vectors of

exciting and scattered light differ only very little in magnitude. The scattering wave (phonon mode) in the crystal, therefore, makes an angle of 135° with the exciting beam. Higher order terms in equation (2-3) represent scattering processes involving more than one phonon. For the selection rules in the case of first order Raman scattering, the symmetry of the $(\partial \alpha / \partial Q_k)_0$ is the relevant one. A normal mode is Raman active when one (or more) of the polarisability tensor elements has the same symmetry as that mode. The different tensor elements and therefore the corresponding modes, can be selected by using polarised exciting radiation and analysing the polarisation of the scattered light. In general, the intensity of the scattered light, due to a certain mode is given by

$$I = A [\mathbf{e}_i^\dagger \boldsymbol{\alpha} \mathbf{e}_s]^2, \quad (2-4)$$

where A is a proportionality constant, \mathbf{e}_i and \mathbf{e}_s are the polarisation vectors of the incoming and scattered light respectively and $\boldsymbol{\alpha}$ is the (first order) polarisability tensor corresponding to the mode in question.

In conclusion, one can find the activity of a normal mode in a first order Raman or in an infrared absorption process, by determining the symmetry of the mode and finding the polarisability tensor elements and dipole moment elements, respectively, that transform according to the same irreducible representation of the point group of the crystal. Moreover, one can define a general vector field, describing all vibrations of the crystal by allowing for each atom a deviation from its equilibrium position. The vector space of all these fields carries the so-called mechanical representation of the lattice vibrations. By reducing this representation into the irreducible representations of the point group, one can find the number of modes transforming according to each representation and thus, also the number of modes active in each polarisation for both Raman and infrared spectra. By using projection operator techniques, one can find a basis for each of these representations, thus allowing for a further characterisation of the lattice vibrations in question. For a general theory on the symmetry of lattice vibrations see Maradudin and Vosko.¹³ As the intensity of the different active modes in the spectra is concerned, one has to go beyond group theory and use a microscopic model to account for the actual intensities and line widths.

2.2.2. Incommensurate crystals

In the case of incommensurate crystals, the use of space group theory is not possible because of the loss of translational symmetry in at least one direction. As was mentioned before, however, the use of superspace groups can overcome this problem. The essence of these higher (than three) dimensional space groups is to treat the independent additional periodicity of the modulation as a fourth (or higher when more periodicities are present) degree of freedom. Comparing this situation with a normal three-dimensional crystal, where one realises that in its reciprocal space all \mathbf{k} -vectors are relevant modulo any reciprocal lattice vector, one sees that in the incommensurate case as well as in the normal one, all reciprocal lattice vectors are equivalent to $\mathbf{k} = 0$, including the modulation wave vector \mathbf{q} . Another way to understand this is when one realises that instead of taking the basic 3D-structure with a modulation with wave vector (say) $\mathbf{q} = \gamma\mathbf{c}^*$ superimposed, one could also choose for a basic structure determined by \mathbf{a}^* , \mathbf{b}^* and \mathbf{q} , interpreting \mathbf{c}^* as a modulation wave vector. This choice would alter the Brillouin zone, as determined by the new basic structure. The vector $\mathbf{k} = n\mathbf{q}$ would be equivalent with zero, while the vector \mathbf{c}^* would be in a general position in the Brillouin zone, but nevertheless still equivalent to $\mathbf{k} = 0$.

Hence the vectors $\mathbf{k} = n\mathbf{q}$ in an incommensurate modulated phase are equivalent with $\mathbf{k} = 0$. The fact that in most cases the choice of the basic structure and the modulation is not difficult stems from the fact that the modulation amplitude normally is temperature dependent, i.e. becomes non-zero for certain temperatures, while the basic structure is relatively temperature independent. Moreover, the structural implications of the modulations are normally very small, therefore the size of the effects on physical properties due to the modulation are also modest. E.g. satellite spots in X-ray diffraction experiments are normally substantially weaker than the main (basic structure) reflections. Their intensity can be expressed in terms of the n -th order Bessel function and generally decreases very rapidly with increasing order n . The same behaviour can be expected (and is observed) for the intensity of Raman and infrared spectra. Modes active at $\mathbf{k} = 0$ are relatively strong, while the additional modes at $\mathbf{k} = n\mathbf{q}$, with $n \neq 0$, are much weaker, their intensity decreasing very fast with increasing n . Nevertheless, due to the equivalency of $\mathbf{k} = n\mathbf{q}$ with $\mathbf{k} = 0$, phonon-modes at $\mathbf{k} = n\mathbf{q}$ are in principle active. The actual activity depends on the symmetry of these modes which is determined by the point group of the superspace group. Thus for incommensurate phases also

group theoretical methods can be used, now referring to superspace groups instead of normal 3D-space groups. For the details we refer to Janssen.⁴

In the case of superstructures (e.g. lock-in phases), again, the modes at $\mathbf{k} = n\mathbf{q}$ are equivalent with $\mathbf{k} = 0$, but in this case that follows already from the fact that the new unit cell, the supercell, is larger and gives rise to a smaller Brillouin zone. The essential difference with an incommensurate structure is that for an superstructure the number of modes with a wave vector equivalent to $\mathbf{k} = 0$ is finite, while in the incommensurate case this number in principle is infinite.

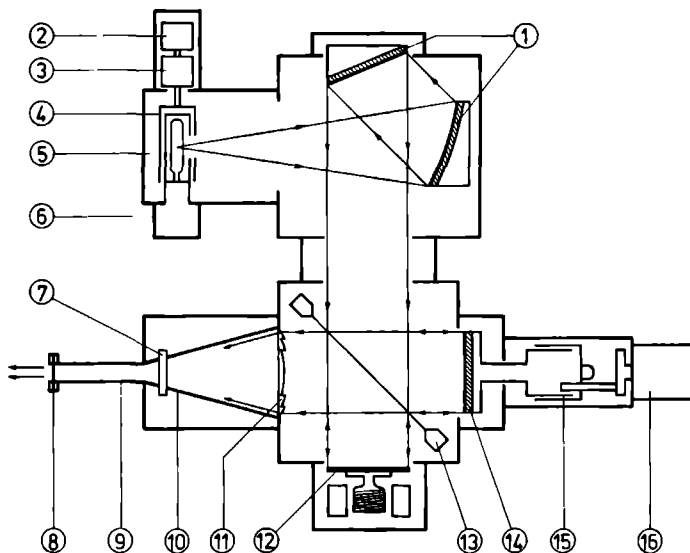
An interesting new class of structures for which even the basic structure is not commensurate is recently found,^{14,15} allowing for new point group symmetries, like the icosahedral ones. For these so-called quasi-crystals the X-ray diffraction pattern has no satellite spots that are weaker than main spots so this distinction and consequently, some of the considerations given above do not apply. Nevertheless, these structures are well described by superspace groups and again, the Fourier wave vectors of these structures are equivalent with $\mathbf{k} = 0$. It would be interesting to study the consequences of these new kind of symmetries for e.g. the vibrational spectra.

2.3. Experimental set-up

2.3.1. Infrared spectroscopy

The infrared spectroscopy presented in this thesis has been limited to the far-infrared regime. Typical wavenumber ranges are 10 cm^{-1} - 350 cm^{-1} or energies of 1.2 meV to 43 meV. The spectra recorded were taken with a Fourier transform spectrometer, based on a Michelson interferometer (Grubb Parsons). This interferometer is schematically drawn in Fig. 2.1. A medium pressure mercury lamp is used as a source for far-infrared radiation, which is collimated by mirrors. The resulting beam with a diameter of approximately 5 cm passes a beam splitter consisting of an exchangeable Mylar film ($6.25\text{ }\mu\text{m}$ – $100\text{ }\mu\text{m}$ thick). The reflected beam is led to a mirror, mounted on a micrometer screw (5 cm total length) driven by a stepping motor, while the transmitted beam is reflected by a second, vibrating mirror, which latter allows for phase sensitive detection. The two reflected beams

F.I.R. MICHELSON INTERFEROMETER



- | | |
|--------------------------------|------------------------------|
| ① Collimator mirrors | ⑨ Lightpipe (polished brass) |
| ② Reference signal generator | ⑩ Brass cone |
| ③ Chopper motor | ⑪ TPX Fresnel lens |
| ④ Chopper | ⑫ Vibrating mirror |
| ⑤ Medium pressure mercury lamp | ⑬ Beamsplitter (mylar film) |
| ⑥ Water-cooled lamp mount | ⑭ Moving mirror |
| ⑦ Transmission filter | ⑮ Micrometer |
| ⑧ Black polyethylene window | ⑯ Stepping motor |

Figure 2 1 The far-infrared Michelson interferometer

interfere with each other at the beam splitter and the resulting radiation leaves the interferometer through a Fresnel lens and a light cone bringing the beam diameter to that of a standard light pipe (13 mm). The thus obtained radiation is led to the

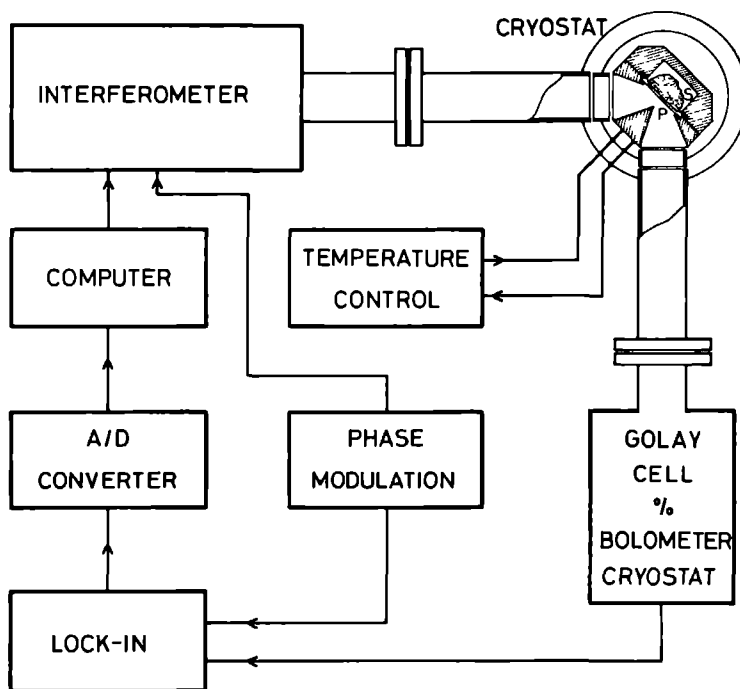


Figure 2.2. Schematic diagram of the complete far-infrared system in the reflection configuration.

sample. In our case (Fig. 2.2) a reflection unit containing two additional light cones in front of a polariser and the sample, allowed for reflection measurements at 90° . This reflection unit was mounted in a He-flow cryostat (Cryoson) which can reach temperatures between approximately 20 K and room temperature, while the same cryostat contained a heater in order to be able to achieve temperatures up to 700 K. The reflected radiation was measured either with a Golay cell or a bolometer-

cryostat. As the source and the transmission or reflection of many other parts in the interferometer system are far from frequency independent, one has to measure a back ground spectrum without the sample. This was done by mounting the crystal on a gold plated slide with a hole for the light to pass in front of the crystal. This slide could be shifted from outside the cryostat, thus keeping the sample at the same temperature, while recording a back ground spectrum of a gold mirror. Spectra with a specimen and corresponding background spectra thus obtained, were collected by a computer, Fourier transformed and mutually divided. The complete system, including light pipes, was evacuated in order to prevent absorption of radiation by water or other molecules.

Temperature was stabilised with a PID-regulator (Oxford). Below room temperature a Au(0.03% Fe)-Cr thermocouple was used, while above room temperature a Pt-100 resistor served as thermometer for the regulator. The temperature of the crystal is measured with a chromel-constantan thermocouple on the back-side of the crystal.

2.3.2. Raman spectroscopy

The Raman spectrometer (Fig. 2.3) consisted of an Ar⁺-ion laser (Coherent Radiation) as a radiation source with a wave length of either 514.5 nm or 488.0 nm, vertically polarised. This light passed a retardation plate in order to be able to rotate the polarisation with respect to the crystal directions. The scattered light is collected at an angle of 90° by a lens and focussed via an analyser on the entree slit of a double grating monochromator (Spex 14018), which contained gratings manufactured holographically and a spatial filter. The light leaving the monochromator was detected by a Peltier-cooled photo-multiplier tube (FW-130, I.T.T.). The output of this tube was fed to an amplifier-discriminator (PAR 1121) and a counter (PAR 1109). The final data were collected by a computer (Digital-Minc), which also drove the stepping motor of the monochromator.

The crystal was mounted in the same cryostat as described in the preceding section. Due to both the high and low temperatures used in the experiment, special precautions were necessary. For this reason, the sample was mounted in a pyrex cell filled with He as contact gas. This gas was cooled by a copper cold finger on which the sample was mounted. The pyrex cell was surrounded by a copper

RAMAN SPECTROMETER

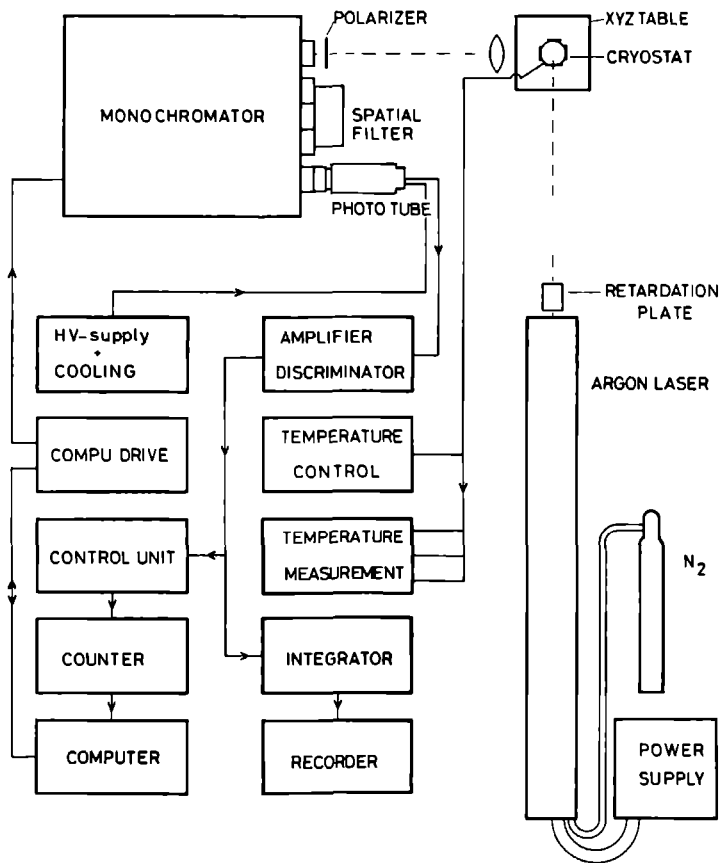


Figure 2.3. Schematic diagram of the Raman spectrometer.

radiation shield at a temperature some what higher than the temperature of the sample. Three holes oi this shield allowed for the light to pass. Again, the temperatures were measured (in the cold finger, just above the crystal) with a chromel-constantan thermocouple.

References

1. For a review see J. Petzelt, *Phase Transitions* **2**, 155 (1981).
2. P.M. de Wolff, *Acta Cryst.* **A33**, 493 (1977).
3. A. Janner and T. Janssen, *Phys. Rev.* **B15**, 643 (1977) and A. Janner and T. Janssen, *Acta Cryst.* **A36**, 399 (1980); **36**, 408 (1980).
4. T. Janssen, *J. Phys.* **C12**, 5381 (1979).
5. Th. Rasing, P. Wyder, A. Janner and T. Janssen, *Phys. rev.* **B25**, 7504 (1982).
6. P. Echégut, F. Gervais and N.E. Massa, *Phys. Rev.* **B30**, 6039 (1984).
7. A. Maciel and J.F. Ryan, *J. Phys.* **C14**, L509 (1981).
8. B. Dam and A. Janner, *Acta Cryst.* **B42**, 69 (1986).
9. Y. Valentine, O.B. Cavin and H.L. Yakel, *Acta Cryst.* **B33**, 1389 (1977).
10. A. Yamamoto and H. Nakazawa, *Acta Cryst.* **A38**, 79 (1982).
11. A.C.R. Hogervorst, thesis, Delft (1986).
12. G. Turrell, *Infrared and Raman Spectra of Crystals* (Academic Press, London, 1972); for Raman scattering see also R. Loudon, *Advances in Physics* **13**, 423 (1964).
13. A. Maradudin and S.H. Vosko, *Rev. Mod. Physics* **40**, 1 (1968).
14. D. Shechtman, I. Blech, D. Gratias and J.W. Cahn, *Phys. Rev. Letters* **53**, 1951 (1984).
15. T. Janssen, *Acta Cryst.* **A42**, 261 (1986).

2.4. The Raman and infrared spectra of the incommensurate crystal Na_2CO_3

H. Meekes, Th. Rasing* and P. Wyder**
Research Institute for Materials

A. Janner and T. Janssen
Institute of Theoretical Physics

University of Nijmegen, Toernooiveld,
6525 ED Nijmegen, The Netherlands

Abstract

The complete Raman spectra of Na_2CO_3 in its monoclinic (β), incommensurate (γ) and lock-in (δ) phase as well as the far infrared spectra in the γ - and δ -phase have been measured and interpreted using symmetry and phenomenological arguments. Additional modes have been observed in the incommensurate phase as predicted by the superspace group selection rules of γ - Na_2CO_3 . Two soft modes have been observed; one of them belongs to the monoclinic-to-incommensurate phase transition. Clear evidence has been found for the existence of a low temperature commensurate (δ) phase.

† Physical Review B34, 4240 (1986).

2.4.1. Introduction

During the last ten years a growing interest in incommensurate crystal phases has developed. Besides structural investigations, a lot of work has been devoted to the study of lattice vibrations, by means of light scattering. This paper is intended to give a contribution to this field by analysing the Raman and infrared spectra of sodium carbonate (Na_2CO_3), which is a well known example of a displacively incommensurate crystal structure. Some preliminary results herein have already been published elsewhere.¹

Incommensurate modulated crystals are characterised by a periodic distortion (modulation) which in wavelength does not fit with the periodicities of the underlying undistorted lattice. Frequently, this crystal phase is intermediate between a high temperature normal (N) phase and a low temperature commensurate (C) phase, where the modulation wave vector is locked-in to a rational value with respect to the reciprocal lattice of the undistorted crystal. The modulation can be of the displacive or of the density type, or of both.

One of the main consequences of the incommensurate nature of the modulation is the lack of lattice translational symmetry for this type of crystal. As many properties of normal crystals, such as the unit cell, Brillouin zone, phonons, etc., are closely related to the lattice translational symmetry, one could expect that all these properties will change drastically in the case of incommensurate structures. Experiment, however, shows that incommensurate crystals share most of the physical properties of the normal crystalline state. In particular their diffraction patterns show the familiar sharp Bragg spots. A first description of the appearance of these crystalline properties can be found in the work of de Wolff² and Janner and Janssen.^{3,4} In their approach, use is made of $(3+d)$ -dimensional space groups, so-called superspace groups. In the superspace the lattice symmetry of the incommensurate crystal is restored and one can again use notions like Brillouin zone, Bragg plane, etc., but in more than three dimensions. The real crystal appears as an intersection with the three-dimensional space of a structure appropriately embedded in the superspace.

The use of space group symmetry in deriving selection rules for light scattering is well established (see e.g. Hayes and Loudon⁵). In the case of incommensurate structures the superspace groups play the role of space groups for normal crystals and corresponding selection rules are easily found. Moreover the superspace groups can also be of help in the case of superstructures (e.g. commensurate crystal

phases), even when the supercell is not a very large one.

The specific choice of sodium carbonate as a model structure for our experiments was made for two reasons. First of all, the structure of the crystal is known in its several phases and secondly the modulation is quite significant, with amplitudes up to 0.4 Å. Both the modulation amplitudes and the wave vector are temperature dependent. Hence the effects of the modulation on the phonon spectrum are expected to become apparent while going through the different phases of the crystal.

This expectation is also supported from the theoretical point of view. One knows that the behaviour of excitations in the incommensurate phase depends on the superspace group symmetry of the crystal. The selection rules for Raman and infrared (IR) active modes have already been shown to be relevant for the understanding of spectra of Rb_2ZnBr_4 (Rasing *et al.*⁶). Those for Na_2CO_3 will be derived further on.

The work done so far on light scattering in the case of sodium carbonate has been limited to infrared transmission in the internal mode regime and Raman scattering for two temperatures⁷ and low frequency Raman scattering for several temperatures.⁸

This paper is organised as follows. Section 2.4.2 deals with the structure of sodium carbonate. Experimental details and results are given in section 2.4.3. Section 2.4.4 covers the interpretation of the results. Some conclusive remarks can be found in section 2.4.5.

2.4.2. The structure of sodium carbonate

Sodium carbonate belongs to the A_2BX_n (with $n = 3$ or 4) family of dielectrics, where several crystals are known to have an incommensurate modulated phase.

In Na_2CO_3 there are at least three clearly distinguishable phases. Above 763 K a hexagonal structure (α -phase) exists, stable up to the melting point at 1123 K. The structure in this phase has space group $P6_3/mmc$. Between 620 K and 763 K the crystal is monoclinic (β -phase) with space group $C2/m$. Below 620 K an incommensurate phase appears (γ -phase). In addition de Pater and Helmholtz⁹ found in a neutron diffraction experiment evidence for a fourth phase below 130 K (δ -phase) in which the crystal is commensurate and forms a superstructure of the β -

phase.

The incommensurate (γ -) phase has a one dimensional modulation with wave vector $\mathbf{q} = \alpha\mathbf{a}^* + \gamma\mathbf{c}^*$, where $\alpha = 0.182$ and $\gamma = 0.318$ at room temperature (\mathbf{b} is the unique axis and \mathbf{c} is the pseudo-hexagonal axis of the basis structure). In a harmonic approximation,¹⁰ it has been found that the modulation is polarised along \mathbf{b} for most of the atoms (with amplitudes up to 0.4 \AA at room temperature), only two oxygen atoms of every CO_3 -ion having a polarisation with components along \mathbf{a} and \mathbf{c} too. The result is an overall displacive modulation along \mathbf{b} , combined with a libration of the CO_3 -ions in their plane and around the C-O direction perpendicular to \mathbf{b} . The phases of the modulation wave are different for the various atoms in the unit cell of the basis structure. A projection of the C-centered cell and of the primitive cell in the β -phase is given in Fig. 2.4.

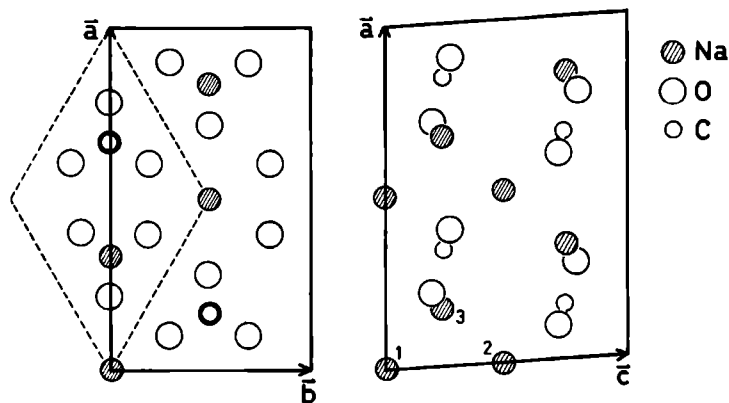


Figure 2.4. Two projections of the C-centered cell of Na_2CO_3 in the monoclinic β -phase. The primitive cell is drawn with broken lines in the projection along \mathbf{c} . The numbers at the Na sites are referred to in the text. Note the pseudo-hexagonal symmetry.

The atomic positions of the average structure at room temperature are:

$$\begin{array}{ll}
 \text{Na(1)} & : \mathbf{r}_1 = (0,0,0) \\
 \text{Na(2)} & : \mathbf{r}_2 = (0,0,\frac{1}{2}) \\
 \text{Na(3), C, O(2)} & : \mathbf{r}_j = (x_j, \frac{1}{2}, z_j) \quad (j = 3,4,5) \\
 \text{O(1), O(3)} & : \mathbf{r}_j = (x_j, y_j, z_j) \quad (j = 6,7)
 \end{array}$$

These positions are given with respect to the C-centered cell. The Na(1) and Na(2) atoms will be denoted as Na(*l*), when referred to in the α -phase, because of their equivalency in that phase. The generators of the point group $2/m$ are $m_y: (x, y, z) \rightarrow (x, \bar{y}, z)$ and $2_y: (x, y, z) \rightarrow (\bar{x}, y, \bar{z})$. The Na and C atoms, as well as the O(2), are invariant under the mirror operation; The two-fold axis leaves only Na(1) and Na(2) invariant.

The evidence for the presence of the δ -phase was not very clear and not apparent in a number of subsequent experiments. We will come back to this question. According to de Pater⁹ the commensurate value of the wave vector is $\mathbf{q} = \frac{1}{6}\mathbf{a}^* + \frac{1}{3}\mathbf{c}^*$, leading to a twelvefold superstructure with respect to the β -phase, with space group $P2/a$ (C_{2h}^4).

2.4.3. Experimental

2.4.3.1. Crystal preparation

The samples used in the unpolarised Raman and far infrared (FIR) measurements have been cut from larger crystals grown by the Bridgman method. On going through the α - β transition the single crystals get microtwinning around the \mathbf{c}^* -axis with six possible domain orientations. Therefore these crystals are not suitable for measurements using polarised light. The corresponding samples were opaque and roughly shaped. They were cut further and polished in order to improve the transparency of the faces. The final dimensions were approximately $4 \times 4 \times 4 \text{ mm}^3$.

All crystal manipulation was done in a dry nitrogen atmosphere to avoid hydration of the samples.

2.4.3.2. Raman measurements

The Raman measurements were made with an Ar⁺-ion laser working at 514.5 nm as a source and a Spex Industries double grating monochromator with spatial filter. Incoming and outgoing beams were mutually perpendicular.

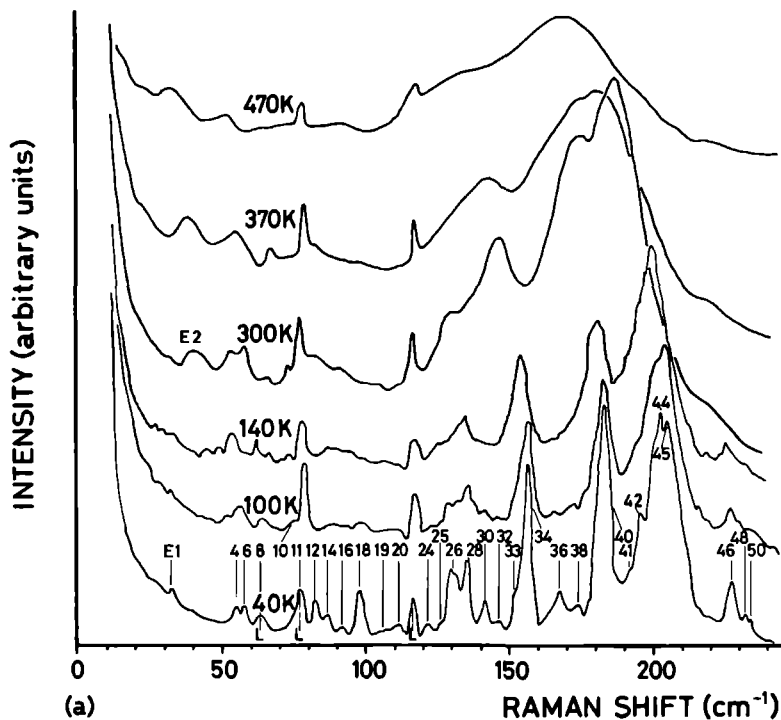


Figure 2.5-a. Unpolarised external modes Raman spectrum of Na₂CO₃ for a few temperatures. The identifiers E_n are referred to in the text; L indicates instrumental (laser plasma) lines.

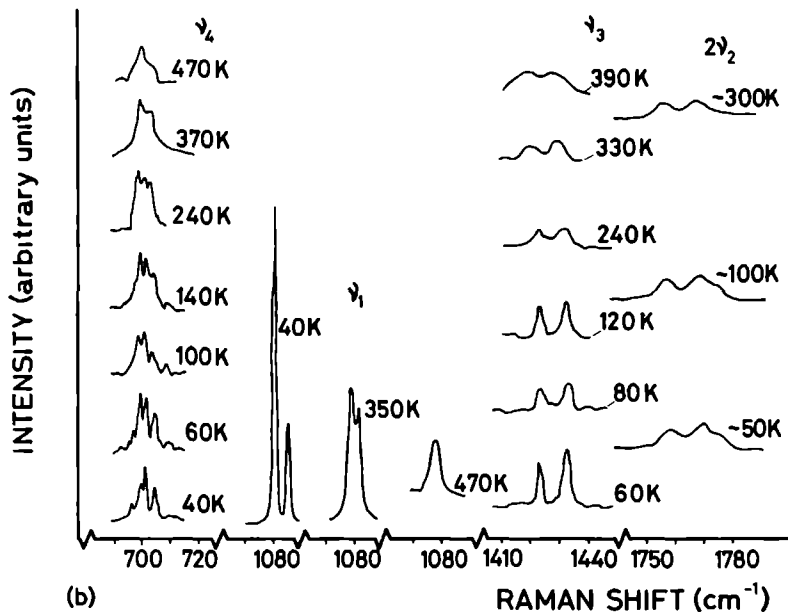


Figure 2 5-b Unpolarised internal modes Raman spectrum of Na_2CO_3 for a few temperatures The identifiers ν_n are referred to in the text

The photon counting has been done by standard equipment The exciting continuous power used varied from approximately 0.03 - 1 W

The complete unpolarised Raman spectra (internal and external modes) were measured from 40 K up to 685 K, with intervals of 20° The spectral resolution was about 2 cm^{-1} Frequency calibration was achieved by measuring the complete (attenuated) Rayleigh line for each spectrum The error in the frequencies however, is mainly due to the interpretation of the line form, and will depend strongly on temperature and specific mode (see below) Measurements above approximately 600 K were difficult or even impossible, because the samples tended to turn black at the spot where the laser light entered By lowering the power of the laser radiation down to 30 mW, the effect started at higher temperature It is probably due to

instability of the CO₃-ions under such conditions. The same phenomenon occurred, but then only above approximately 650 K, using a Nd-YAG laser working at 1064 nm in second harmonic generation experiments.¹¹ The surface of the sample was clearly destroyed by the radiation and the Raman signal disappeared. Hence most of the measurements have been done in the γ - and δ -phase. A few examples of Raman spectra taken at various temperatures are presented in Fig. 2.5-a and b.

With an exception for two soft modes, the instrumental line shape was not deconvoluted, nor fitted to a Lorentzian because we consider this inadequate for complex incommensurate structures like Na₂CO₃. The line form of a mode in the incommensurate phase is made up of many individual lines, whose mutual intensity ratios depend strongly on temperature as will become clear in section 2.4.4.5. Because of this and the large number of phonon branches in Na₂CO₃ one would need too many parameters in a fit to be valuable. More simple (well known) incommensurate structures could be appropriate for such an analysis. Therefore we have measured the frequency by taking the middle of the upper peak part of a line, assuming that the $\mathbf{k} = 0$ contribution is the largest and manifests itself as such a peak, for temperatures not too close to the lock-in transition. Furthermore, we are not interested in the exact phonon frequencies but rather in the global temperature dependence and splitting of lines. The frequency shifts as a function of temperature are plotted for all Raman lines in Fig. 2.6-a and b.

In the case of the soft modes, which will be treated in section 2.4.4.3, The peak frequencies (ω_p) were obtained by subtracting the Rayleigh wing. The mode frequencies (ω_0) were calculated with $\omega_0^2 = \omega_p^2 + \frac{1}{2} \Gamma^2$, where Γ is the full width at half maximum of the Raman line. This expression follows when the mode is interpreted as a damped harmonic oscillator, whose Raman intensity is given by

$$I(\omega, T) = K \frac{(n(\omega, T) + 1) \omega \Gamma \omega_0^2}{(\omega_0^2 - \omega^2)^2 + \omega^2 \Gamma^2} \quad (2-5)$$

(see e.g., Hayes and Loudon;⁵ K is a constant with respect to ω and T) and the Bose-Einstein factor (n) is approximated by $\frac{kT}{\hbar\omega}$ (for $T \approx 500$ K and $\omega \approx 30$ cm⁻¹).

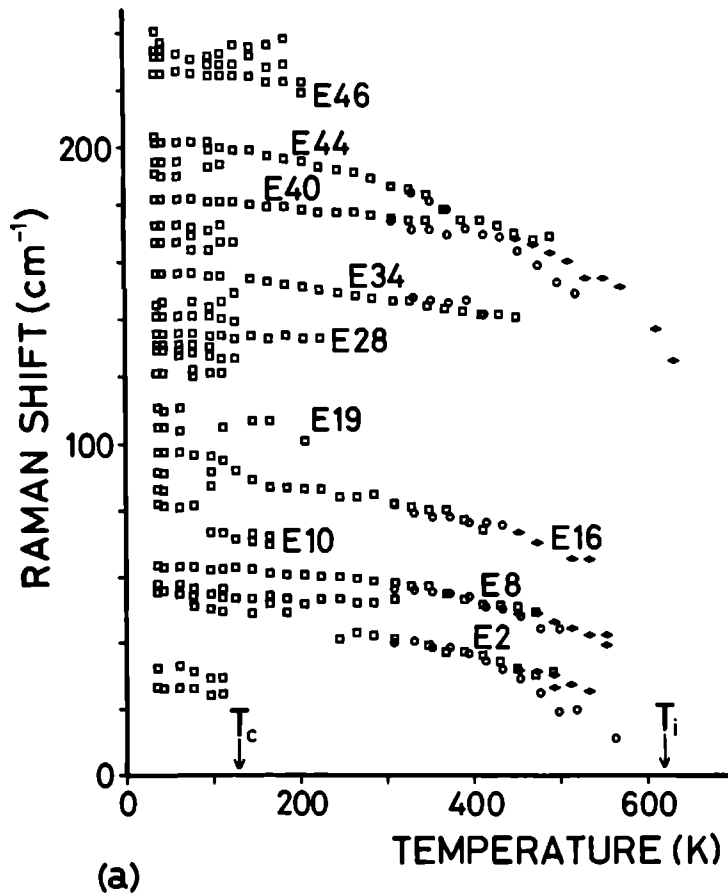


Figure 2 6-a. Raman shift versus temperature for the external modes of Na_2CO_3 . Indicated are the lock-in transition temperature (T_c) and the incommensurate phase transition temperature (T_i). The identifiers E_n are given for the most significant lines. The squares, circles and diamonds refer to different samples used and do not indicate the experimental error.

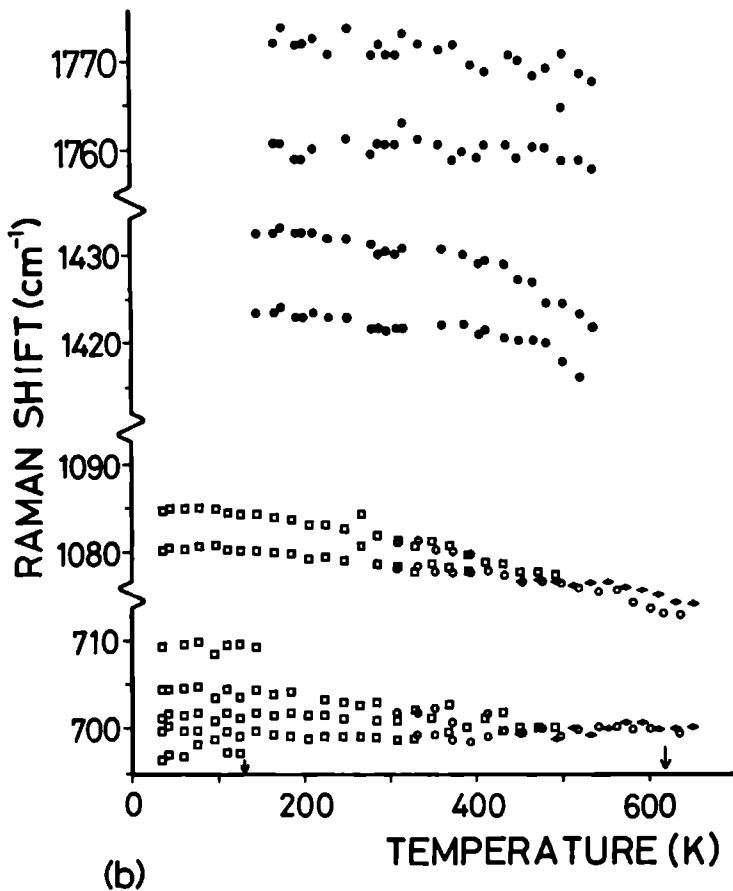


Figure 2 6-b. Raman shift versus temperature for the internal modes of Na_2CO_3 . Indicated are the lock-in transition temperature (T_c) and the incommensurate phase transition temperature (T_i). The squares, circles and diamonds refer to different samples used and do not indicate the experimental error. The two highest-internal-mode data (full circles) are from earlier measurements, using 1 W laser power.

2.4.3.3. FIR measurements

The FIR experiment consisted mainly of reflection measurements at 45° for the incoming and outgoing light. A Michelson interferometer has been used as a FIR source. The detector consisted of either a He-cooled bolometer or a Golay cell.

The FIR reflection spectra were measured from 40 K up to 375 K. For higher temperatures the lines grew too broad to give any new information. Two spectra are presented in Fig. 2.7. The internal modes were not measured. For the lowest wave numbers (up to 60 cm^{-1}) some transmission data were available¹². No measurements were done in the α - and β -phase.

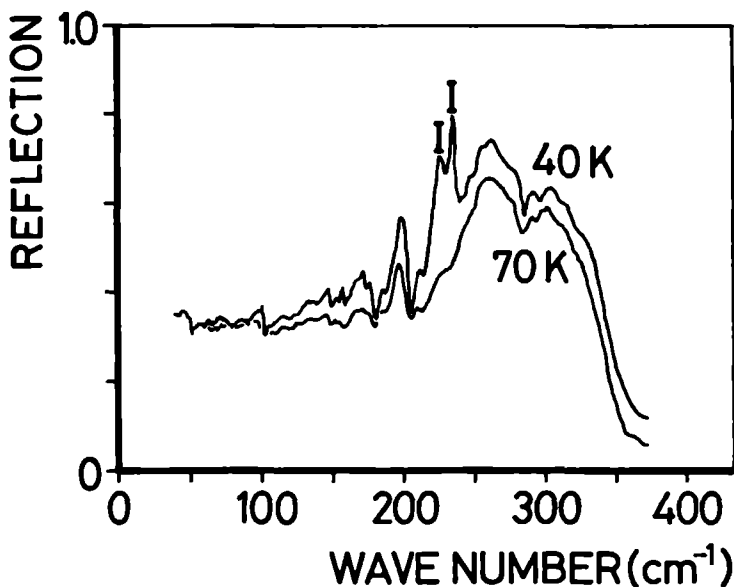


Figure 2.7 Far infrared reflection spectrum of the external modes of Na_2CO_3 for two temperatures. I denotes two instrumental peaks.

2.4.3.4. Temperature control

The samples were mounted in a He gas flow cryostat for temperatures from 4 K up to 300 K. For temperatures from 300 K up to 700 K the samples were heated in the same "cryostat". Special care was taken to be sure of the sample temperature, as will be explained below. Due to both the very low and very high temperatures used in the Raman measurements, the crystal (mounted on a cold/hot finger) showed a very large temperature gradient over the sample in the earlier measurements. On the other hand the crystal seemed to be quite absorbing for the laser light used. Therefore a pyrex cell was constructed, which was filled with He exchange gas. The cell was shielded (except for holes for the in- and outgoing light) by a copper radiation shield at about the same temperature as the sample. A second copper radiation shield was placed within the outer cryostat case. The laser output power was kept smaller than 0.2 W, for which no influence on the spectra was observed. All results given were measured with this arrangement, unless otherwise specified.

The temperature of the sample was measured within the copper cold/hot finger just above the crystal, by means of a chromel-constantan thermocouple. This finger served also as a source for the temperature of the contact gas. Especially at the lowest (40 K) and highest (650 K) temperatures, this resulted in reliable measurements. For the FIR measurements the sample was almost completely enclosed by a copper block. The temperature has been measured at the crystal's backside with a chromel-constantan thermocouple. We estimate the absolute error in the temperatures to be less than 5 degrees; the relative error probably less, both for the Raman and FIR measurements.

2.4.4. Interpretation

Due to the lack of single crystals and the large number of Raman and FIR active normal modes in Na_2CO_3 the assignment of the lines observed is rather difficult. A great deal, however, can be done on the basis of the selection rules one has for the different phases and of course the analysis of the influence of the modulation on the different modes. Combining these elements in a consistent way, we were able to reach a fairly complete understanding of all the spectra. Occasionally we compare the results with those already published on K_2CO_3 and

Rb₂CO₃ (Brooker and Bates¹³), because these structures (though commensurate) show a great resemblance to sodium carbonate.¹⁴

We will start with a derivation of the selection rules for light scattering in the different phases.

2.4.4.1. Optical activity of the modes

The optical activity of modes at $\mathbf{k} = 0$ in the α - and the β -phase has been obtained by standard methods based on space group symmetry whereas that of the modes in the γ -phase was obtained correspondingly by using superspace group methods. For a review on the use of space group symmetry in deriving selection rules for light scattering (Raman and IR) see e.g. Hayes and Loudon.⁵

TABLE 2-I.

D_{3h}	n (vibr)	activity	α -Na ₂ CO ₃	β -Na ₂ CO ₃
A_1'	1	Raman	$A_{1g} + B_{2u}$	$A_g + B_u$
A_2''	1	IR	$B_{1g} + A_{2u}$	$A_g + B_u$
E'	2	Raman	$2E_{2g}$	$2A_g + 2B_g$
		IR	$2E_{1u}$	$2A_u + 2B_u$

Table 2-I The number of Raman and IR active vibrational modes of the free CO₃-ion. The corresponding symmetries in the α - and β -phase of Na₂CO₃ are indicated.

One distinguishes between internal modes (relative vibrations of CO₃ constituents) and external modes (the remaining lattice vibrations). The latter have been considered in the rigid ion approximation, where the CO₃-ion is considered as a rigid molecule because of the much stronger bonds within the ion as compared to the "external" lattice bonds. Next to the internal modes, one then gets a number of librational (CO₃-ion), optical and acoustical translational modes that transform according to irreducible representations of the corresponding space group. We will use the Mulliken notation for these irreducible representations. The number of vibrational modes of the free CO₃-ion (symmetry group D_{3h}) and their symmetry are given in Table 2-I. The results for the α -phase of Na₂CO₃ are summarised in Table

2-II, those for the β -phase are given in Table 2-III.

TABLE 2-II

D_{6h}	$n(\text{acoust})$	$n(\text{opt tr})$	$n(\text{rot})$	$n(\text{vibr})$	activity
A_{1g}	0	0	0	1	Raman
E_{1g}	0	0	1	0	Raman
E_{2g}	0	2	0	2	Raman
A_{2u}	(1)	2	0	1	IR
E_{1u}	(1)	2	0	2	IR

Table 2-II The number of Raman and IR active modes in the α -phase of Na_2CO_3 . Parentheses indicate the acoustical modes which are not active

The optical activity of fundamentals is for normal crystals restricted to modes at $\mathbf{k} = 0$. In the case of incommensurate crystals, however, the modes at $\mathbf{k} = n\mathbf{q}$ (where \mathbf{q} is the incommensurate wave vector and n an integer) are equivalent to those at $\mathbf{k} = 0$ (Janssen¹⁵). Therefore modes at $\mathbf{k} = n\mathbf{q}$ may become optically active, depending on the symmetry with respect to the point group. The modes can be labeled by the irreducible representations of the three-dimensional point group isomorphic to that of the superspace group. In the case of Na_2CO_3 the superspace group is $P_{1'}^{C2/m}$ (Janner and Janssen³), and the point group is thus isomorphic to $2/m$.

TABLE 2-III

C_{2h}	$n(\text{acoust})$	$n(\text{opt tr})$	$n(\text{rot})$	$n(\text{vibr})$	activity
A_g	0	4	1	4	Raman
B_g	0	2	2	2	Raman
A_u	(1)	3	2	2	IR
B_u	(2)	6	1	4	IR

Table 2-III. The Raman and IR active modes in the β -phase of Na_2CO_3 . Parentheses indicate the acoustical modes which are not active

With the help of the superspace group the symmetry of modes at $\mathbf{k} = n\mathbf{q}$ can be derived. Because the intensity of modes in a light scattering experiment is expected

to decrease very fast with growing n in the case of a sinusoidal modulation,^{16,17} the selection rules are derived only for $n = 0, \pm 1$. The results are given in Table 2-IV.

TABLE 2-IV:

C_{2h}	$n(\text{acoust})$	$n(\text{opt tr})$	$n(\text{rot})$	$n(\text{vibr})$	activity
A_g	0 + 1	4 + 5	1 + 4	4 + 4	Raman
B_g	0 + 2	2 + 10	2 + 2	2 + 8	Raman
A_u	(1)+ 2	3 + 10	2 + 2	2 + 8	IR
B_u	(2)+ 1	6 + 5	1 + 4	4 + 4	IR

Table 2-IV. The Raman and IR active modes in the γ -phase of soda, indicated as $n_{k=0} + n_{k=\pm q}$. Parentheses indicate the acoustical modes which are not active.

The details of the change in selection rules due to the transition to the δ -phase will be given later.

The basis vectors of the irreducible representations containing one or more phonon modes, have been derived in all the phases. They were not strictly determined by the representations of the β -phase; the eigenvector is assumed to differ not much from that of the corresponding mode in the α -phase. The results for the external modes in the α - and β -phase are given in Table 2-V.

2.4.4.2. The internal modes

As already pointed out, a distinction has to be made between internal and external modes. The internal modes describe vibrations inside the CO_3 -ion, which has very strong bonds. Accordingly, its vibrational modes occur at rather high frequencies. For Na_2CO_3 , external modes typically have frequencies ω below 350 cm^{-1} , whereas the internal modes lie near 700, 880, 1080 and 1420 cm^{-1} , respectively. Due to these high frequencies, the coupling of the internal modes to the lattice is small. The dispersion of the internal modes is therefore very flat. Furthermore, comparing the values of the vibrational modes of the free CO_3 -ion¹⁸ with those in the crystal, one finds a difference in frequency of about 3, 0, 2 and 5 %, respectively. Hence the internal modes can be treated, within a good approximation, as local modes, the frequency being determined by the structure of

TABLE 2-V

α -phase	β -phase	mode		number	assignment
		Acoustical			
A_{2u}	B_u	along c		1	-
E_{1u}	A_u	along b		2	-
	B_u	along a		3	-
		Librational			
A_{2g}	B_g	CO ₃ around c	symm	4	E_{16} (C16)
E_{1g}	A_g	CO ₃ around b	symm	5	E_8 (C8)
	B_g	CO ₃ around a	symm	6	in Rayleigh line (E_2 at $\mathbf{k} = \pm\mathbf{q}$)
B_{2u}	A_u	CO ₃ around c	a-symm	7	
E_{2u}	A_u	CO ₃ around a	a-symm	8	
	B_u	CO ₃ around b	a-symm	9	
		Translational			
B_{2g}	A_g	CO ₃ along c	a-symm	10	
		Na(3) along c	a-symm	11	
E_{2g}	A_g	CO ₃ along a	a-symm	12	
		Na(3) along a	a-symm	13	
	B_g	CO ₃ along b	a-symm	14	
		Na(3) along b	a-symm	15	
A_{2u}	B_u	CO ₃ along c	symm	16	
		Na(3) along c	symm	17	
		Na(I) along c	symm	18	
B_{1u}	B_u	Na(I) along c	a-symm	19	
E_{1u}	A_u	CO ₃ along b	symm	20	
		Na(3) along b	symm	21	
		Na(I) along b	symm	22	
	B_u	CO ₃ along a	symm	23	
		Na(3) along a	symm	24	
		Na(I) along a	symm	25	
E_{2u}	A_u	Na(I) along b	a-symm	26	
	B_u	Na(I) along a	a-symm	27	

Table 2-V Basis vectors of the external modes transforming corresponding to the different irreducible representations in the α - and the β -phase. Note that the acoustical modes are also present among the translational modes. Symm and a-symm means symmetric and anti-symmetric, respectively, under a permutation of two equivalent ions, Na(I) stands for Na(1) or Na(2). The numbers are referred to in the text. A justification of the assignment to the Raman lines (at $\mathbf{k} = 0$) and the clusters (Cn) in the δ -phase can be found in sections 2, 4, 4, 3, 4 and 6, for the clusters see also Table 2-VII.

the CO_3 -ion itself and by the local surrounding of that ion. This local character is expected to be more pronounced, the higher the frequency. The external modes must be treated, of course, as ordinary phonon modes, which extend (in principle) through the whole crystal.

Due to the flat dispersion of the internal modes, the presence of a displacive modulation gives rise to a modulated shift in frequency for the individual ions with respect to that of an average structure. Therefore, the experimental line shape of the internal modes in the incommensurate phase shows a frequency distribution reflecting properties of the modulation. Which type of distribution one has to consider in the case of sodium carbonate was suggested by de Wolff and Tuinstra¹⁴ on the basis of a model developed by Blinc *et al.*¹⁹ for NMR measurements. We will call it the WTB-model and use it, taking into account the case of an incommensurate modulation involving more than one harmonic.

On going through the crystal, the local field felt by the CO_3 -ion takes all values between zero and the one due to a maximum displacement. We expand the frequency of an internal mode of the CO_3 -ion in a power series of the order parameter η , which describes the local effect of the modulation:

$$\nu = \nu_0 + a_1\eta + \frac{a_2}{2}\eta^2 + \dots \quad (2-6)$$

In equation (2-6) only even powers in η contribute, due to the (m)-symmetry element of sodium carbonate. The frequency distribution $f(\nu)$ depends on the density of ion sites $\rho_j(\mathbf{r})$ according to:

or (2-7)

$$f(\nu) = \frac{\rho}{|\nabla\nu|},$$

where $\xi \equiv \mathbf{q} \cdot \mathbf{r}$. In the case of sodium carbonate one knows that higher harmonics in the modulation wave have a non-negligible effect and become very important near the lock-in transition. Accordingly we write for the order parameter:

$$\eta = \sum_{n=1}^N f_n \sin(n\mathbf{q} \cdot \mathbf{r} + \phi) , \quad (2-8)$$

where we assume that all harmonics are in phase. From equation (2-6) follows that $f(\nu)$ and hence the intensity of the signal in the light scattering experiment diverge

when $|\nabla v| = 0$ hence, i.e. when $\eta = \eta_{\min} = 0$ or $\eta = \pm\eta_{\max}$. This means that the line shape of the internal modes shows two edge singularities, independent of the number of harmonics involved. The intensity ratio of both singularities however, depends on the number of those harmonics. For a single harmonic modulation ($N = 1$ in equation (2-7)), the intensity due to the two singularities will be equal. This is expected to be the case just below the incommensurate phase transition. For temperatures in the neighbourhood of the lock-in transition, the number of relevant harmonics in the modulation increases rapidly (discommensuration regime) and the modulation wave form is rather square-like than sinusoidal. In this regime the intensity of the line at the singularity point corresponding to $\eta = \pm\eta_{\max}$ will be stronger than that at the $\eta = 0$ singularity point. A more quantitative approach is only possible if one knows the form of the modulation wave.

In the commensurate phase the line form may change due to the commensurate value of the modulation wave vector.

In what follows, each internal mode is discussed in some detail. The experimental data used are taken from Brooker and Bates^{7,13} for material relevant to the IR internal modes of Na_2CO_3 and the IR and Raman data of K_2CO_3 and Rb_2CO_3 , whereas the Raman data on Na_2CO_3 are based on our own measurements. Symmetry considerations are given here for the β -phase; the reader is reminded that the γ -phase is a modulated β -phase structure and that all measurements have been collected in either the γ - or the δ -phase. For the experimental results see Figs. 2.5 and 2.6.

2.4.4.2.1. The ν_1 internal mode

This is the totally symmetric breathing mode, with free ion frequency 1063 cm^{-1} , symmetry A'_1 (Raman active only), giving rise to an A_g and a B_u symmetry mode in the crystal field of the β -phase. The IR active B_u component is not observed, while the A_g component is very strong in the Raman spectrum. The observed Raman signal consists of two sharp peaks at approximately 1080 cm^{-1} and 1085 cm^{-1} , respectively, at the lowest temperature. Hence the observations fit well with the WTB-model. The intensity ratio of the two peaks and the frequency difference of both plotted versus temperature are given in Fig. 2.8. If we extrapolate the intensity ratio linearly to the value 1, we find a temperature of approximately 560 K, interpreted as the temperature above which the modulation is mainly sinusoidal.

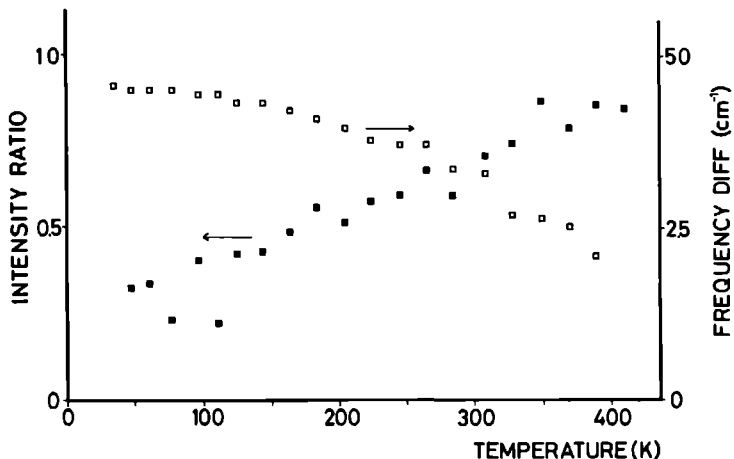


Figure 2.8 Frequency difference and peak-intensity ratio of the two components of the ν_1 internal mode of Na_2CO_3 versus temperature. The squares do not give the experimental error.

For lower temperatures the low frequency component becomes the strongest and this line can therefore be interpreted as corresponding to the $\eta = \pm\eta_{\text{max}}$ singularity. Below 140 K (which is just above the lock-in transition at 130 K) the ratio is 0.2 to 0.4.

In the model, the frequency difference between the two discontinuities is given by $\frac{1}{2}a_2\eta_{\text{max}}^2$ and therefore it depends on the amplitude and number of higher harmonics of the modulation. Experimentally, below approximately 140 K, this difference is almost constant indicating that the wave form is fairly stable below T_c . Above that temperature range the frequency difference decreases linearly until about 310 K, where it drops to a lower value. For temperatures above approximately 390 K the difference is too small to be detected. The step behaviour at 310 K could be related to the fact that the wave vector of the modulation locks-in to a value lying on the line $\alpha + \gamma = \frac{1}{2}$ below 300 K, with only quite small changes in its absolute value.⁹ An extrapolation to zero splitting would be tentative. In the case of K_2CO_3 and Rb_2CO_3 the IR component was very weak and this is consistent

with the idea of a small influence of the lattice.

2.4.4.2.2. The ν_2 internal mode

The free ion frequency of this mode is 879 cm^{-1} , its symmetry A_2'' and it is IR active. It consists of polar movements perpendicular to the plane of the ion. Under influence of the crystal field of the β -phase this mode splits into two components, $A_g + B_u$, hence Raman and IR active, respectively. The Raman active component however, was not observable, the IR component being quite strong, which is a further indication for the weak coupling between the ions. However, a two-phonon ν_2 Raman component was seen, although very weak. The selection rules for such a two phonon process imply

$$\Gamma(\text{two } -\nu_2) = 2A_g + 2B_u \quad (2-9)$$

where $A_g \times A_g = B_u \times B_u = A_g$ and $A_g \times B_u = B_u$; hence three different lines are expected.

In the IR, one line is expected in the β phase. In the γ phase the spectrum consists of two lines at 880 cm^{-1} and 886 cm^{-1} respectively, which again fits well in the WTB-model. When using high exciting powers up to 1 W, three Raman lines were resolved below approximately 140 K (N.B., these temperatures are not reliable due to heating of the sample by the high power of the laser used and the bad cooling during that measurement). The corresponding frequencies were observed at 1758, 1770 and 1775 cm^{-1} . At higher temperatures and in later measurements only two lines were seen at 1760 and 1772 cm^{-1} . The last two are exactly twice the value of the IR data and are therefore expected to be of the type $B_u \times B_u$. The $A_g \times A_g$ component is probably too weak, but could have given rise to the 1775 cm^{-1} line of the early measurements. The splitting of the two Raman lines seems to be constant up to approximately 450 K, although the intensity is too weak to draw definite conclusions. A striking feature, however, is the fact that the intensity of the 886 cm^{-1} IR line is smaller than that of the 880 cm^{-1} line at 300 K, while the two $-\nu_2$ intensities are comparable. This difference could be due to the less stringent demands on the phonon wave vectors for a two-phonon process ($\mathbf{q}_1 + \mathbf{q}_2 = 0$), which also explains the broader Raman lines as compared to the IR fundamentals. In the case of K_2CO_3 and Rb_2CO_3 also, the Raman ν_2 line was not observable, while the two $-\nu_2$ component was present, although a few cm^{-1} higher than twice the

fundamental frequency.

2.4.4.2.3. The ν_3 internal mode

The ν_3 mode is a doubly degenerate E' mode (Raman and IR active) with frequency 1415 cm^{-1} , consisting of non-symmetric motions in the plane of the ion. In the crystal field these modes split according to $A_g + B_g + A_u + B_u$, which are Raman and/or IR active. Because the unperturbed free ion modes are already active, one expects that the perturbed crystalline modes are also observable in both the Raman and IR spectra. This is indeed the case. The IR spectrum consists of two lines at 1413 cm^{-1} and 1425 cm^{-1} and the Raman spectrum also of two lines at 1422 cm^{-1} and 1431 cm^{-1} . The splitting is probably due to the crystalline field, which is also supported by the temperature dependence of the frequency difference of the two components. The movements of the O-atoms are much smaller than those of the C-atom. This mode, therefore, is less perturbed by the surrounding ions, than in the case of the ν_1 and ν_2 modes. Hence the value of a_2 in equation (2-6) is much smaller for the ν_3 mode than for the ν_1 and ν_2 ones and the two singularities are probably not resolved. A third small peak is observed at about 1450 cm^{-1} , when using high exciting power ($\approx 1\text{ W}$). In such a situation this peak shows the same frequency-dependence with temperature as the first two up to 300 K , where its frequency is 1448 cm^{-1} . In measurements done at less power, it is no longer observed. The Raman spectra of Brooker and Bates⁷ show the same peak at 1448 cm^{-1} (at room temperature), but the authors do not mention it. The frequency difference between this line and the first two, makes an assignment to a ν_3 mode rather difficult. In the case of K_2CO_3 and Rb_2CO_3 all Raman components were resolved, but the IR lines were broad and not all resolved.

2.4.4.2.4. The internal ν_4 mode

This mode is also a doubly degenerate E' mode with frequency 680 cm^{-1} . It consists of non-symmetric movements in the plane of the ion, the C-atom having the largest amplitude. In the IR three components were seen at 694 , 701 and a very weak line at 706 cm^{-1} . Brooker and Bates⁷ found only two Raman components, while we observe three lines resolved below 300 K . Below T_c five modes can be

seen. The A_g and B_u components consist of motions along **a**, while the B_g and A_u components have motions mainly along **b**. The modulation has displacements along **b** mainly; hence one expects the splitting of the two singularities to be the strongest for the B_g and A_u components, as compared with the other ones. This can explain the three observed modes in the IR and Raman spectrum. On the other hand it is possible that the edge singularities of the different ν_4 components are not resolved. This would be the case if the splitting of the low frequency component is the same as (or somewhat less than) that of the high frequency component. The fact that for this internal mode more lines are resolved on going from the γ - to the δ -phase, is probably due to a larger dispersion as compared to the other internal modes which have a higher frequency or higher symmetry. We will come back to this subject, when we treat the lock-in transition. In the case of K_2CO_3 and Rb_2CO_3 all Raman components and three of the four IR lines were observed.

2.4.4.3. The soft modes

Before turning our attention to the external mode spectra we would like to discuss the soft modes which play an important role in the $\alpha - \beta$ and the $\beta - \gamma$ phase transitions.

As in Na_2CO_3 several phase transitions are driven by soft phonons; the question arises whether they are visible in the spectra. The various soft modes responsible for the different phase transitions have been found theoretically by Maciel and Ryan^{8,20} and de Wolff and Tuinstra.¹⁴ Let us mention them in order to get an overall picture.

At the hexagonal-to-monoclinic phase transition temperature (T_α), the doubly degenerate symmetric librational mode of the CO_3 -ions becomes soft. Below T_α this mode becomes hard and splits up in the **a** and **b** polarised components. These components are both Raman active. The E symmetry acoustic mode at $(0,0,q_3) \approx 0$ couples to the E_{1g} mode but is of course not visible in the spectra.

At the monoclinic-to-incommensurate phase transition temperature T_i the symmetric librational mode around the **a**-axis becomes soft together with the **b** polarised acoustic mode, both at $\mathbf{k} = \pm\mathbf{q}$, being not Raman active, nor IR active above the transition temperature. Below T_i the librational mode hardens giving rise to Raman and IR active components at $\mathbf{k} = \pm n\mathbf{q}$. The acoustic mode splits into an

amplitudon which grows hard and a phason at zero frequency, the amplitudon being Raman active.

Below the lock-in transition at T_c , the original phason mode grows hard, resulting in an IR active mode at non-zero frequency.

Maciel and Ryan⁸ have looked at the low frequency Raman spectrum and have found two "hard" modes which they ascribed to the two librational modes belonging to the hexagonal phase transition. They compared their results with measurements on K_2CO_3 , where only one mode for the hexagonal phase transition was found.²⁰ Their explanation was that in K_2CO_3 the component of the soft mode that did not induce the transition to the monoclinic phase, stayed low in frequency, hidden under the Rayleigh line. The observation of this mode in Na_2CO_3 was explained to be due to a larger anisotropy in the hexagonal plane.

We found the same modes, however with different behaviour as a function of temperature. In fact, in our case, the highest mode ($E8$) extrapolates to zero at T_α , but the lowest one ($E2$) does not (Figs. 2.9 and 2.6).

If we extrapolate the mode frequency (ω_0 , see section 2.4.3.2) to zero, we find a temperature between T_α and T_i . We are very certain of the temperature values obtained in our measurements, because as mentioned in section 2.4.3, we paid much attention to this point. It is, however, difficult to find an exact extrapolation, due to the scattering of data points. Nevertheless, the data tend more towards T_i than to T_α .

Moreover, we think that also in Na_2CO_3 one of the two librational modes stays at low frequency (B_g). This conclusion has been obtained on the basis of the same model as used by Maciel and Ryan. In that model the Landau free energy is written as a power series of the order parameter ϕ (given by the tilt angle of the CO_3 -ions), up to sixth order:

$$\begin{aligned}
 F = & \frac{1}{2}\alpha(T)\phi^2 + \frac{1}{4}V\phi^4 + \frac{1}{6}W_1\phi^6(\eta_1^6 + 9\eta_1^2\eta_2^4 - 6\eta_1^4\eta_2^2) + \\
 & \frac{1}{6}W_2\phi^6(\eta_2^6 + 9\eta_2^2\eta_1^4 - 6\eta_2^4\eta_1^2) + \frac{1}{4}C_{44}(e_4^2 + e_5^2) + \\
 & g\phi(e_4\eta_1 + e_5\eta_2)
 \end{aligned} \tag{2-10}$$

The η_i are the coordinates of the librational mode with $\eta_1^2 + \eta_2^2 = 1$; $\alpha(T) = A(T - T_0)$. Terms representing elastic strains and a linear coupling of the order parameter to shear strains is included. Minimising the free energy with respect to the order parameter one finds:

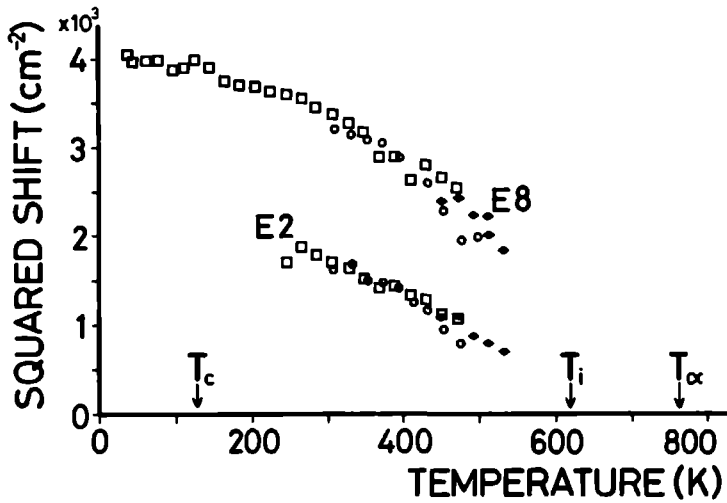


Figure 2.9 Squared frequency shift versus temperature for the two soft modes (E8 and E2) of Na_2CO_3 . Indicated are the hexagonal-to-monoclinic phase transition temperature (T_c) and the incommensurate phase transition one (T_i). Again three different samples have been used, the experimental error is not indicated.

$$\phi^2 = \frac{1}{2W_1} \{-V \pm (V^2 - 4W_1\alpha'(T))^{1/2}\} \quad (2-11)$$

where $\alpha'(T) = A(T - T_c)$ and $T_c = T_0 + 2g^2/(AC_{44})$. In the case of a first order phase transition, the order parameter will have a spontaneous non-zero value at the transition temperature. In the case of sodium carbonate, the tilt angle of the CO_3^- ions is linearly related to the angle β of the monoclinic cell. This appears very clearly in the mechanical model of de Wolff and Tuinstra.¹⁴ The angle β has been measured as a function of temperature by Crooijmans²¹ and shows a quadratic behaviour in the neighbourhood of the transition:

$$\left\{ \frac{\beta(T) - 90^\circ}{360^\circ} \right\}^2 = A'(T - T_\alpha) \quad (2-12)$$

above approximately 690 K, with $A' \approx 4.7 \cdot 10^{-6} \text{ K}^{-1}$. Such a behaviour is expected in the case of a second order transition. Therefore we conclude that indeed the transition is of second order (cf. de Pater and Helmholtz⁹). This implies that $T_\alpha \approx T_c$, $V > 0$ and $W \ll V$. The order parameter becomes simply

$$\phi^2 \approx -\frac{A}{V}(T - T_c) \quad (2-13)$$

The frequencies ω_i of both librational components can be expressed as

$$\omega_1^2 \approx -2A(T - T_0) + \frac{2g^2}{C_{44}}$$

and (2-14)

$$\omega_2^2 \approx \frac{2g^2}{C_{44}} .$$

If we use our data for $\omega_1^2(T)$ we find an upper limit of 14 cm^{-1} for ω_2 in the worst case of extrapolation. Even if we use the data of Maciel and Ryan this becomes $\omega_2 \approx 19 \text{ cm}^{-1}$ as upper limit. Both these values are smaller than the frequency of the lowest lying soft mode (E_2) and actually lie in the Rayleigh wing. Therefore we conclude that this mode does not indeed belong to the hexagonal, but to the incommensurate phase transition, and is probably the mode corresponding to the soft librational phonon at $\mathbf{k} = \pm \mathbf{q}$. This conclusion is supported by the fact that the acoustic E_1 symmetry branch, which couples to the soft mode for the hexagonal phase transition, also has one component which stays low in frequency throughout the β -phase. This follows from diffuse scattering observed in X-ray and neutron diffraction experiments.¹⁴ The amplitudon probably lies at lower frequency than the above mentioned mode, as it originates from an acoustic branch at $\mathbf{k} = \pm \mathbf{q}$. In K_2SeO_4 e.g., it lies at approximately 35 cm^{-1} (Wada *et al.*²²). Hence we expect this mode to be somewhere close to the Rayleigh line, as mentioned before. Maciel and Ryan found a mode at approximately 35 cm^{-1} , which they ascribed to the amplitudon.

A fourth Raman line was found at low temperatures, somewhere between the two soft modes and interpreted as the $\mathbf{k} = \pm \mathbf{q}$ mode, belonging to the lowest soft mode. The same mode was found by us: E_6 in Figs. 2.5 and 2.6. Looking at its

temperature dependence we would rather suggest that this mode is the $\mathbf{k} = \pm\mathbf{q}$ component of the upper soft mode. At the lowest frequencies (below about 30 cm^{-1}) some structure was observed in the tail of the Rayleigh line, especially when using high exciting power. This structure does not reproduce well for different temperatures. This can be explained by the presence of $\mathbf{k} = \pm n\mathbf{q}$ components of the acoustic modes, which overlap and which change in frequency and intensity as a function of a varying form of the modulation wave and its wave vector. We will now discuss the remainder of the external mode spectra.

2.4.4.4. The external modes in the γ -phase

In this section we devote our attention to the interpretation of the external mode spectra in the γ phase.

2.4.4.4.1. The Raman spectra

As one sees immediately (Figs. 2.5 and 2.6), the number of lines is too big to make the standard method for assignment useful. At the lowest temperature there are about thirty resolved lines, which have been numbered up to fifty (see Fig. 2.5). At higher temperatures these lines cluster together giving rise to about eleven lines just below 200 K. We will start with the interpretation of these eleven lines (E_{46} , E_{44} , E_{40} , E_{34} , E_{28} , E_{19} , E_{16} , E_{10} , E_8 , E_6 and E_2).

The selection rules for the β -phase give at most nine observable lines, three rotational and six translational modes. Hence, there is at least one additional mode, which is specific for the incommensurate γ -phase. Indeed only the average structure of the γ -phase has the same space group symmetry as the β -phase. We can furthermore consider the gross structure of the spectrum due to the average structure as a slightly deformed high temperature α -phase. We make thus use of the selection rules valid in the α -phase. In this phase all modes of symmetry A_{2g} , B_{2u} , E_{2u} , B_{2g} , B_{1u} and E_{2u} are not active in the Raman, nor in the IR spectra. At the phase transition from the hexagonal to the monoclinic phase all these modes become active (A_g , B_g , A_u or B_u) in principle. The modes which are not active in the α -phase are expected to have a low intensity in the β -phase spectra, as compared

to the modes which are active in both phases. These weak Raman active modes are number 4, 10 and 11 in Table 2-V. The modes which are expected to be strong in the β -phase are number 5, 6, 12, 13, 14 and 15 in Table 2-V. Two of these last six modes are the soft modes of the $\alpha - \beta$ or the $\beta - \gamma$ transition, grown "hard". These give rise to the lines $E8$ and $E2$, and have already been treated, together with $E6$, in the section concerning the soft modes. It remains to look for four strong modes in the Raman spectrum. In Fig. 2.5 we indeed see four strong modes, namely $E44$, $E40$, $E34$ and $E28$. In this figure we also observe (cf. Fig. 2.6) that $E44$ and $E40$ grow towards each other at higher temperatures. The same holds for $E34$ and $E28$. This decreasing splitting is related to the angle β approaching 90° when the temperature comes close to 763 K. Therefore we expect both the $E40-E44$ and the $E28-E34$ pairs to be degenerate in the α -phase. Because of the higher mass of the CO_3 -ion with respect to that of Na ($M(\text{CO}_3) \approx 2.6M(\text{Na})$) the low frequency modes ($E28-E34$) will correspond to normal modes for which mainly the CO_3 -ions move, either along **a** or **b**, while the pair $E40-E44$ corresponds to a similar mode, consisting primarily of Na(3) motions. Because the modulation is mainly polarised along **b**, one expects that the modes which at the lowest temperature consist of many resolved lines correspond to motions along **b** (see also the section devoted to the lock-in transition). Therefore we conclude (see also Table 2-V):

$E44$:	(mainly) Na(3) translation along b	anti-symmetric	(B_g)
$E40$:	(mainly) Na(3) translation along a	anti-symmetric	(A_g)
$E34$:	(mainly) CO_3 translation along a	anti-symmetric	(A_g)
$E28$:	(mainly) CO_3 translation along b	anti-symmetric	(B_g)

We are left with the modes $E46$, $E19$, $E16$ and $E10$. These modes are all rather weak. Because they are (except $E16$) not observable above 200 K, the assignment is even more difficult. Nevertheless we would like to present here a few considerations. If we compare the two translational modes Na(3) or CO_3 along **c**, which are anti-symmetric, we expect their frequencies to be smaller than those of the corresponding modes along **a** or **b**. This because of the smaller Na-O distances in the **a**, **b**-plane, compared to the Na-Na or Na-C distances along **c** (de Wolff and Tuinstra¹⁴). The libration around **c** has a moment of inertia, which is approximately twice as big as that of the librations around **a** or **b**, resulting in a lower frequency. On the other hand, due to the stronger bonds in the **a**, **b**-plane, the frequency is expected to be higher. Therefore we suggest that (see also Table 2-V):

<i>E</i> 16:	CO ₃ libration around <i>c</i>	symmetric	(<i>B_g</i>)
<i>E</i> 19:	(mainly) Na(3) translation along <i>c</i>	anti-symmetric	(<i>A_g</i>)
<i>E</i> 10:	(mainly) CO ₃ translation along <i>c</i>	anti-symmetric	(<i>A_g</i>)

The fact that the cluster (even above the lock-in transition) of three modes *E*46 to *E*50 is not assigned to a normal mode of the β -phase structure will be explained in the section concerning the lock-in transition.

2.4.4.4.2. The FIR spectrum

When we look at the FIR reflection spectrum (Fig. 2.7), the first striking feature is the resemblance to the Raman external mode spectrum. The FIR however has lines up to 350 cm⁻¹ and the line form is much broader.

The selection rules allow fifteen IR active external modes in the β -phase. Nine of these fifteen modes correspond to the nine Raman active modes, where symmetric is replaced by anti-symmetric, and conversely. The remaining six modes are number 18, 19, 22, 25, 26 and 27 in Table 2-V. Those IR active modes in the β -phase, which are inactive in the α -phase are again expected to be weak in the monoclinic phase. These are all modes which are anti-symmetric. The remaining nine strong modes are number 16, 17, 18 and 20 up to 25 in Table 2-V. The three acoustic modes, which are not IR active, are among these. Therefore we expect six strong and six weak lines. The modes in which only the Na(*I*) ions move will have relatively high frequencies with respect to the other ones and can thus be regarded as normal modes, because the Na(*I*)-ions are in the centre of an octahedron of oxygen atoms, with small Na-O distances compared to the Na(3)-CO₃ distances.¹⁴ Therefore we suggest that the three strong modes observed above 200 cm⁻¹ correspond to the three Na(*I*) modes which are symmetric. Due to the high frequencies of these modes, we can expect to see $\mathbf{k} = n\mathbf{q}$ (with $n \neq 0$) modes in the Raman spectrum, because they will not be obscured by $n = 0$ Raman lines. The three $n \neq 0$ Raman components at about 230 cm⁻¹ correspond to the lowest one of the three high frequency FIR modes (see the section on the lock-in transition). The two highest FIR modes have no component in the Raman spectrum. This can be explained by the fact that the 230 cm⁻¹ mode is **b**-polarised and therefore couples to the modulation, while due to screening of the O-atoms the $\partial\alpha/\partial Q$ stays small for the other two modes, resulting in a low Raman activity at $\mathbf{k} = n\mathbf{q} \neq 0$. The remaining

three modes are symmetric $\text{Na}(3)\text{-CO}_3$ translations parallel to \mathbf{a} , \mathbf{b} and \mathbf{c} . These modes can be assigned to the 100, 170 and 200 cm^{-1} lines. The \mathbf{c} -polarised mode is probably the lowest lying because of the greater inter ion distances. The remainder of the spectrum is difficult to interpret without more information. On the other hand it might be possible that the 230 cm^{-1} mode is the \mathbf{b} -polarised $\text{Na}(3)\text{-CO}_3$ mode, which is expected to appear resolved in the Raman spectrum, whereas the $\text{Na}(I)$ modes due to the screening mentioned above should give rise to less resolved weak Raman lines.

2.4.4.5. The lock-in transition

The question of whether or not Na_2CO_3 undergoes a lock-in transition has attracted the attention of several investigators. The first evidence for a lock-in transition has been obtained by de Pater and Helmholtz by neutron diffraction on a single crystal first, and in a powder experiment later.⁹ The commensurate value of the wave vector was found to be $\mathbf{q} = \frac{1}{6}\mathbf{a}^* + \frac{1}{3}\mathbf{c}^*$, the space group $P2/a$ and the transition temperature about 130 K.

Subsequent X-ray diffraction however, revealed no lock-in transition²³ and the same negative result was found in experiments on specific heat and on the dielectric constant.²⁴ Even the Raman experiments done by Maciel and Ryan⁸ showed no particular features in the neighbourhood of the lock-in transition.

The presence or absence of a lock-in phase transition in different crystals of the same compound is a well known phenomenon. Often these discrepancies between different samples are ascribed to the presence of defects or impurities for which incommensurate crystal phases are more sensitive than commensurate ones. In some cases, the impurities are claimed to be responsible for the absence of the transition²⁵; in other cases they would be the cause of the presence of a commensurate phase.²⁶ In any case, these phenomena are still badly understood. The distinction between incommensurate and commensurate phases has little meaning in the limit of very large unit cells. In our case, however, the distinction between the twelve fold superstructure and the incommensurate phase appears very clearly in the Raman spectra. Looking at Fig. 2.6 we see below $T_c \approx 130\text{ K}$ many modes which do not appear above this temperature. In fact, looking at the spectra, we see broad lines above 130 K, which resolve into rather sharp lines below this

temperature. This effect is somewhat obscured by the broadening of the lines with increasing temperature. The striking feature is that, on lowering the temperature, almost all lines start at 130 K, and that indicates a phase transition. Furthermore, above this temperature the structure superimposed on the broad lines is not the same at every temperature; this means that above the transition the structure changes rapidly with temperature, and this is consistent with the presence of a temperature-dependent incommensurate modulation. The explanation for the resolving of many lines in the commensurate phase is the following. The low-temperature commensurate phase is modulated, the modulation giving rise to a fairly large number of inequivalent atomic positions within the unit cell of the superstructure, lattice periodicity ensuring sharpness in the Raman lines.

In the incommensurate phase, above the transition temperature T_c , the crystal consists of commensurate regions (precursors of the lock-in structure), but the incommensurability of the modulation wave imposes the presence of so called discommensurations. From the point of view of the modulation wave, the whole is realised by a squared-like wave involving a fairly large number of higher harmonics. One can describe the same behaviour using instead of higher harmonics the low-temperature modulation wave together with a position dependent phase. In that case, the commensurate regions are characterised by a constant phase value, whereas the regions of discommensurations show a very rapid variation of the phase. This has two consequences for the Raman lines in the incommensurate regime. First of all, the presence of higher harmonics increases the intensity of the $\mathbf{k} = n\mathbf{q}$ modes for higher n values. Note however, that even at room temperature, and thus far away from the lock-in transition temperature T_c , the modulation wave is already non-sinusoidal.²⁷ Secondly, the discommensuration regions produce a broadening of the lines with respect to the corresponding ones in the commensurate phase. A consequence of the presence of higher harmonics is the increase of the intensity of the $\mathbf{k} = n\mathbf{q}$ modes (for higher n) in e.g. the Raman spectrum. In Fig. 2.10 a schematic plot is shown for the Raman line form in both the incommensurate and the commensurate phase. We see that due to the incommensurate value of the wave vector, the line form is very broad, with a structure superimposed, depending on the value of \mathbf{q} and the intensity of the various higher order satellites. In the neighbourhood of the lock-in transition the wave vector slowly drops to its commensurate value, when the temperature is lowered towards T_c , starting at approximately 200 K (de Pater and Helmholdt⁹). The change in the value of \mathbf{q} causes the structure in the Raman line to change considerably because the change in

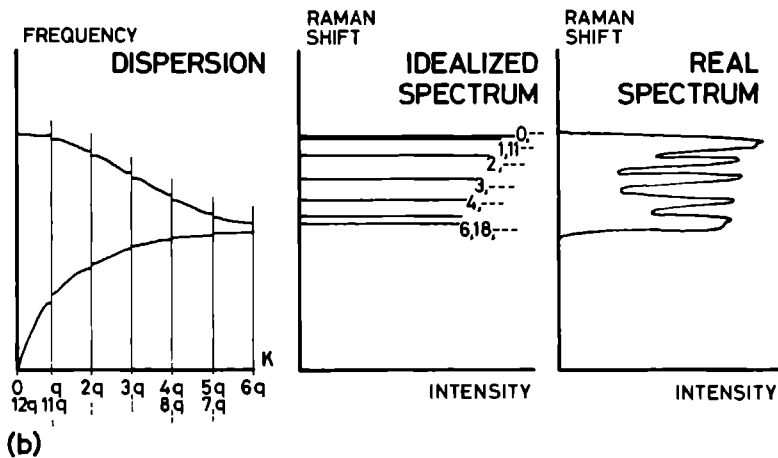
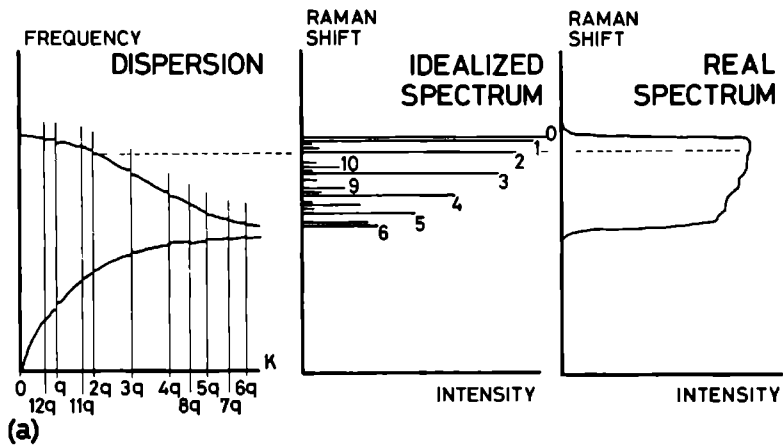


Figure 2.10 Expected Raman line form in the incommensurate phase near the lock-in transition (a) and in the commensurate phase (b). In the incommensurate phase not all lines are drawn for clarity. The relevant ones occur when the corresponding gap is significant (see broken lines). The intensities are arbitrarily chosen.

the frequency shift of a line at $\mathbf{k} = n\mathbf{q}$ is approximately n times the shift of the corresponding $\mathbf{k} = \mathbf{q}$ component. Moreover, instability of the value of \mathbf{q} near the lock-in transition causes the structure in the line form to be less well defined.

Another way of looking at the line form in the neighbourhood of the lock-in is to consider a superstructure approximation, describing the structure as a (twelvefold) superstructure with small deviations:

$$\mathbf{q} = \left(\frac{1}{6} - \delta_1\right)\mathbf{a}^* + \left(\frac{1}{3} - \delta_3\right)\mathbf{c}^* \quad (2-15)$$

where $\delta_1 \ll \frac{1}{6}$ and $\delta_3 \ll \frac{1}{3}$.

Now the line form will be that of the twelvefold superstructure perturbed, however, by additional modes due to the deviations. Again higher harmonics are needed to explain the strength of the additional modes, and the pronounced temperature dependence of the lines observed. In the commensurate case, apart from decrease of thermal broadening, the spectrum is much less sensitive to temperature changes. It is mainly the intensity of the resolved peaks which changes with temperature and this is an effect due to variation in the modulation wave form.

The activity of the modes at $\mathbf{k} = n\mathbf{q}$, both in the incommensurate and in the commensurate phase, can be obtained by means of the superspace group symmetry of the structure. In the present paper, this has already been done (for the incommensurate phase) up to the terms involving $n = \pm 1$. In the superstructure case, because of the large (twelvefold) supercell, the enormous matrices needed while using ordinary space groups, reduce (thanks to the superspace group) easily to twice the size of the matrices needed in the normal phase. The results of the analysis are given in Table 2-VI.

We see that every Raman active (*gerade*) mode for $n = 0$ splits into seven Raman and five IR active components in the δ -phase. The opposite (i.e. five Raman and seven IR components) holds for the IR (*ungerade*) $n = 0$ modes. The distinction between the *A* and *B* symmetries will not be of much use because of the lack of single crystals. The expected clusters of seven or five modes represent an upper limit. This can be seen in Fig. 2.10; the splitting of the components depends on the dispersion of the non-perturbed branch and on the splitting of the modes at $\mathbf{k} = n\mathbf{q}$, the latter being due to the coupling with the modulation.

At this point a distinction between external and internal modes is relevant again. The consistency between the approach described above and the one in the WTB-model is as follows. In the incommensurate phase, for a sinusoidal modulation, the splitting will be mainly present at $\mathbf{k} = \pm\mathbf{q}$, the higher order gaps decreasing very

TABLE 2-VI:

β -phase	γ -phase $n = 0, \pm 1, \pm 2, \pm 3, \dots$	δ -phase
A_g	$\rightarrow A_g + \frac{A_u}{B_g} + \frac{A_g}{B_u} + \frac{A_u}{B_g} + \dots$	$\rightarrow 4A_g + 3B_g + 3A_u + 2B_u$
B_g	$\rightarrow B_g + \frac{A_g}{B_u} + \frac{A_u}{B_g} + \frac{A_g}{B_u} + \dots$	$\rightarrow 3A_g + 4B_g + 2A_u + 3B_u$
A_u	$\rightarrow A_u + \frac{A_g}{B_u} + \frac{A_u}{B_g} + \frac{A_g}{B_u} + \dots$	$\rightarrow 3A_g + 2B_g + 4A_u + 3B_u$
B_u	$\rightarrow B_u + \frac{A_u}{B_g} + \frac{A_g}{B_u} + \frac{A_u}{B_g} + \dots$	$\rightarrow 2A_g + 3B_g + 3A_u + 4B_u$

Table 2-VI. Superspace group analysis of the modes (at $\mathbf{k} = n\mathbf{q}$) which are equivalent with $\mathbf{k} = 0$ in the β , γ and δ -phase. In the γ -phase one has a pair consisting of a gerade and an ungerade mode for each value of $|n| \neq 0$.

fast in magnitude.^{16,17} In the case of the v_1 mode for example, the zeroth order A_g mode has a B_g first order mode (at $\mathbf{k} = \pm\mathbf{q}$). The difference in intensity due to the difference in perturbation, is compensated by the relatively large number of ions perturbed by the modulation as compared to those which are not affected. This result is comparable with the two singularities with equal intensity as predicted by WTB model.

If on the other hand the modulation wave form is rather square-like, higher harmonics of $\mathbf{k} = \pm\mathbf{q}$ will be present and therefore the dispersion curve will show first order gaps at $\mathbf{k} = n\mathbf{q}$ ($n = \pm 1, 2, \dots$) too. For a flat dispersion this will result in two peaks, one corresponding to the zeroth order frequency, the other to the frequency which is perturbed in first order, again assuming that the higher order perturbations are negligible. As a result, the intensity of the line corresponding to the perturbed frequency will be stronger than the other one.

In the region where the modulation has a wave form between a sinusoidal and a square wave, the two singularities are expected to be broader and less well resolved. In the commensurate phase the modulation can be described by a wave form resembling to a great extent a square wave. Hence there are relatively many ions at positions where $\eta = \eta_{\max}$ and very few at $\eta = 0$. Again the different orders of perturbations between these lines will compensate the asymmetry in the lines.

In conclusion, the expected line form will depend largely on the modulation wave form as a function of temperature and on the form of the dispersion curves for the different branches. If we return our attention to the experimental results, we recognise, looking at the Raman spectrum, the different clusters resolved at the lowest temperature.

2.4.4.6. The external modes in the δ -phase

In this section we will explain how the different line forms of the clusters observed in the spectra of the δ -phase can be understood in terms of modes coupling to the modulation, using the results of the assignments in the γ -phase. The Raman lines belonging to the different clusters (C_n) are given in Table 2-VII

TABLE 2-VII

cluster	components	max number
C48	E50, E48, E46	5
C44	E45, E44, E42, E41	7
C40	E40, perhaps E38	7
C34	E34, perhaps E33	7
C28	E28, E26, E25, E24	7
C19	E20, E19	7
C16	E18, E16, E14, E12	7
C10	E10	7
C8	E8, E6, E4	7

Table 2-VII The Raman lines belonging to the different clusters in the δ -phase. The choice of the components is sometimes disputable. The identifiers E_n can be found in Fig 2.5 and partly in Fig 2.6. The maximum number of components (see also Table 2-VI) is given too.

Those modes for which the movements of the ions are (partly) along **b**, will couple strongly to the modulation, giving rise to a large splitting in several components. This is the case for the clusters C44, C28 and C16.

The opposite holds for the modes with no (or small) motions along \mathbf{b} ; they will show no or small splitting. This holds for the clusters $C40$, $C34$, $C19$ (although too weak) and $C10$.

Beside the splitting of the clusters, additional modes can be expected due to ($\mathbf{k} = 0$) IR active modes. Cluster $C48$ provides the clearest example of such lines; where due to the absence of a (strong) $n = 0$ line, the components are quite well resolved, even above the lock-in transition.

Cluster $C44$ can also contain $\mathbf{k} = n\mathbf{q}$ contributions due to a strong FIR line at the same frequency. Component $E18$ of cluster $C16$ clearly grows in intensity with decreasing temperature, starting at T_c . In the FIR a small though clear mode at 100 cm^{-1} , visible up to 130 K is seen. These modes are probably related. Finally, the Raman lines $E38$ and $E36$ are isolated and have corresponding lines in the FIR spectrum. Hence one expects the former to be $n \neq 0$ components of the FIR lines. The same holds for $E32$ and perhaps $E30$. It is however difficult to assign these lines to normal modes.

The FIR spectrum gives no further clear information on the lock-in transition, probably because of the broader peaks as compared to the Raman lines. Only a decreasing line width is observed by lowering the temperature.

2.4.5. Conclusion

We have measured the complete Raman spectra of Na_2CO_3 in the monoclinic (β), the incommensurate (γ) and the commensurate lock-in (δ) phase. The far infrared spectra have been obtained in the γ - and in the δ -phase. The different lines have been assigned and interpreted by using symmetry as well as phenomenological arguments. Most of the lines found have been assigned to the different phonon modes of the β -phase.

As the selection rules (obtained by using the superspace group of $\gamma\text{-Na}_2\text{CO}_3$) predict, additional modes are active in the incommensurate phase. A few of these modes have been seen and interpreted in both the Raman and IR spectra. The additional modes (lying at $\mathbf{k} = n\mathbf{q}$ for $n \neq 0$ in the β -phase) often differ not much in frequency from the corresponding modes at $\mathbf{k} = 0$. This and the fact that their optical activity is mostly rather small, causes the difficulty in observing these modes in the different spectra. We nevertheless have found additional modes which were

resolved because of three different reasons:

- The Raman lines E_{50} , E_{48} , E_{46} , E_{38} , E_{36} , E_{32} , E_{18} and perhaps E_{30} are interpreted as corresponding to $n \neq 0$ components of IR active modes at $\mathbf{k} = 0$. The absence of the relatively strong $\mathbf{k} = 0$ component and the fact that these additional modes are not obscured by other (strong) Raman active modes makes them observable.
- Those branches which are mainly \mathbf{b} -polarised, will be most sensitive to the modulation. Therefore the gaps at $\mathbf{k} = n\mathbf{q}$ will be the largest for these branches. This is observed in the Raman spectra of the commensurate phase, where the \mathbf{b} -polarised modes consist of clusters which have more components resolved than modes which are mainly \mathbf{a} or \mathbf{c} -polarised.
- The soft mode belonging to the phase transition to the incommensurate phase has wave vector $\mathbf{k} = \pm\mathbf{q}$ and is a resolved "additional mode" due to its temperature-dependent frequency and intensity near the phase transition.

For the internal modes (vibrations of the CO_3 -ion constituents), the line shape is better described by a frequency distribution, which is determined by the modulation amplitude in the vicinity of the different CO_3 -ions. This frequency distribution has two singularities at the frequencies corresponding to a maximal and a minimal modulation displacement. The intensities of the corresponding peaks in the spectra depend mainly on the number of higher harmonics involved in the modulation wave form. The higher the frequency of an internal mode, the flatter is its dispersion and therefore the better this description in terms of a frequency distribution holds.

Two soft modes have been found in the Raman spectra. One is identified as belonging to the hexagonal-to-monoclinic phase transition; the other one belongs to the monoclinic-to-incommensurate phase transition; this in contrast to results of earlier measurements of Maciel and Ryan.⁸ We conclude that of the two soft mode components, corresponding to the hexagonal-to-monoclinic phase transition, the symmetric libration around \mathbf{b} corresponds to the Raman line E_8 , while the libration around \mathbf{a} stays low in frequency ($\omega < 20 \text{ cm}^{-1}$) for temperatures below the phase transition temperature. The symmetric librational mode around \mathbf{a} at $\mathbf{k} = \pm\mathbf{q}$, which becomes soft together with the \mathbf{b} -polarised acoustic mode at $\mathbf{k} = \pm\mathbf{q}$ at the monoclinic-to-incommensurate phase transition, is observed as E_2 in the Raman spectra.

Finally, we have found clear evidence for a third phase transition to a lock-in (δ) phase at 130 K, which was seen only once before (de Pater and Helmholtz⁹). The effect on the line shape on going from an incommensurate to a commensurate

phase has been discussed and appears to fit well with the experimental results. In short (see Fig. 2.10), the line form in the incommensurate phase is broad and shows a structure superimposed, which is not well reproducible for different temperatures. Due to the increasing number of higher harmonics in the modulation wave form on approaching the lock-in transition, the intensities of the modes at $\mathbf{k} = n\mathbf{q}$ for higher values of n increase. This and the incommensurate value of the modulation wave vector gives rise to a dense cluster of lines in the spectra. The strong temperature dependence of \mathbf{q} in the neighbourhood of the lock-in transition makes the structure of these clusters also strongly temperature dependent. In the lock-in phase, on the other hand, the commensurate value of \mathbf{q} gives rise to a discrete number of lines for each phonon branch, resulting in clusters of fairly sharp lines. The number of lines observed is determined by the symmetry of the different cluster components and the effects of the modulation on the mode involved.

Acknowledgements

We express our gratitude to W. v.d. Linden for the melt-grown crystals, to Joep Engels for the eigenvector calculations in the α -phase, to Karl Hanssen for the FIR transmission data and to the members of the Department of Micro-Structures at the T.H. Delft for the data of Crooijmans and many stimulating suggestions. This work is part of the research program of the Stichting voor Fundamenteel Onderzoek der Materie (Foundation for Fundamental Research on Matter) and was made possible by financial support from the Nederlandse Organisatie voor Zuiver-Wetenschappelijk Onderzoek (Netherlands Organisation for the Advancement of Pure Research).

References

- * Current address: Department of physics, University of California, Berkeley, California 94720.
- ** Current address: Max-Planck-Institut für Festkörperforschung, Hochfeld-Magnetlabor, 166X, F-38042 Grenoble-Cedex, France.
- 1. H. Meekes, K. Hanssen, A. Janner, T. Janssen, P. Wyder and Th. Rasing, *Ferroelectrics* **53**, 285 (1984).
- 2. P.M. de Wolff, *Acta Cryst. A* **33**, 493 (1977).
- 3. A. Janner and T. Janssen, *Phys. Rev. B* **15**, 643 (1977).
- 4. A. Janner and T. Janssen, *Acta Cryst. A* **36**, 399 and 408 (1980).
- 5. W. Hayes and R. Loudon, *Scattering of Light by Crystals* (J. Wiley & Sons, New York, 1978).
- 6. Th. Rasing, P. Wyder, A. Janner and T. Janssen, *Phys. Rev. B* **25**, 7504 (1982).
- 7. M.H. Brooker and J.B. Bates, *J. Chem. Phys.* **54**, 4788 (1971).
- 8. A. Maciel and J.F. Ryan, *J. Phys. C.: Solid State Phys.* **14**, L509 (1981).
- 9. C.J. de Pater and R.B. Helmholtz, *Phys. Rev. B* **19**, 5735 (1979).
- 10. W. van Aalst, J. den Hollander, W.J.A.M. Peterse and P.M. de Wolff, *Acta Cryst. B* **32**, 47 (1976).
- 11. F. Tuinstra (Private communication).
- 12. K.E.H.M. Hanssen, *Doctoraalscriptie K.U. Nijmegen* (1983), p.65.
- 13. M.H. Brooker and J.B. Bates, *Spectrochimica Acta* **30A**, 2211 (1974).
- 14. P.M. de Wolff and F. Tuinstra, in *Incommensurate Phases in Dielectrics*, edited by R. Blinc and A.P. Levanyuk (North Holland, Amsterdam, 1986), Vol 2, p. 253.
- 15. T. Janssen, *J. Phys. C* **12**, 5381 (1979).
- 16. T. Janssen and de C. Lange, *Journal de Physique C* **6**, 737 (1981).
- 17. T. Janssen, in *Incommensurate phases in dielectrics*, edited by R. Blinc and A.P. Levanyuk (North-Holland, Amsterdam, 1986), Vol 1.
- 18. G. Herzberg, *Molecular Spectra and Molecular Structure* (van Nostrand Company Inc., New York, 1954), p.178.
- 19. R. Blinc, S. Juznic, V. Rutar, J. Seliger and S. Zumer, *Phys. Rev. Lett.* **44**, 609 (1980).

20. A. Maciel, J. F. Ryan and P.J. Walker, *J. Phys. C: Solid State Phys.* **14**, 1611 (1981).
21. P.C.B. Crooijmans, unpublished, Delft.
22. M. Wada, A. Sawada, Y. Ishibashi and Y. Takagi, *J. Phys. Soc. Jap.* **42**, 1229 (1977).
23. P.C.B. Crooijmans, G.H. Kolkman and F. Tuinstra, *Abstr. Eighth European Crystallographic Meeting, Liège*, p.243 .
24. M. Midorikawa, K. Tsunoda and Y. Ishibashi, *Journ. Phys. Soc. Japan* **49**, 242 (1980).
25. R.P.A.R. van Kleef, Th. Rasing, J.H.M. Stoelinga and P. Wyder, *Sol. State Comm.* **39**, 433 (1981).
26. K. Hamano, T. Hishinuma and K. Ema, *J. Phys. Soc. Japan* **50**, 2666 (1981).
27. A. Hogervorst, W.J.A.M. Peterse and P.M. de Wolff, in *Modulated Structures*, edited by J.M. Cowley, J.B. Cohen, M.B. Salamon and B.J. Wuensch (AIP Conf.Proc., No. 53, 1979), p.217.

2.5. Raman and infrared studies of $[\text{N}(\text{CH}_3)_4]_2\text{ZnCl}_4$ -A normal versus superspace description-

H. Meekes

Research Institute for Materials

A. Janner and T. Janssen.

Institute of Theoretical Physics

University of Nijmegen, Toernooiveld,

6525 ED Nijmegen, The Netherlands

Abstract

The relevance of a superspace description for Raman and infrared spectra in the commensurate phases of $[\text{N}(\text{CH}_3)_4]_2\text{ZnCl}_4$ has been studied. The selection rules for light scattering have been determined in all phases using as well the normal space groups as one superspace group for all phases. The results have been compared with experimental data. Special attention has been devoted to the domain structure in the two monoclinic phases.

2.5.1. Introduction

The study of crystals with an incommensurate phase has been focused to a large extent on the A_2BX_4 -family of dielectrics. Practically all members of this family studied so far, have a high temperature structure of the β - K_2SO_4 -type, some of them show a hexagonal phase below the melting point. At lower temperatures different modulated superstructures are found, most of which have an orthorhombic symmetry. In the case of an incommensurate phase both the average and the basic structure have orthorhombic symmetry. For a description of the members of this family and a mutual comparison of their symmetry and of their structure on the basis of a semi-microscopic model, see Hogervorst.¹ An analogous approach in terms of a model was used by Janssen.² A different description, based on the representations of the average space group considered in Landau's theory for second-order phase transitions, was given by Plesko *et al.*³ and Muralt *et al.*⁴

The introduction by de Wolff⁵ and Janner and Janssen⁶ of superspace groups to describe the symmetry of incommensurate modulated structures in terms of space groups in more than three dimensions, was found to be very useful, even in the case of commensurate modulations. In fact, both Hogervorst and Janssen found that for many members of the A_2BX_4 -family the superspace group symmetry (which is appropriate for their incommensurate phases) is conserved in the low temperature commensurate phases to a very good approximation, even when the actual 3-D symmetry is lowered due to the loss of one or more symmetry elements of the para phase. Experimentally this was verified by Dam,⁷ who considered the morphology. Moreover, it is found that a restriction that is laid upon the rational value of the q -vector of a commensurate modulation (in a superspace description), which depends on the symmetry elements lost, is obeyed in all 44 phases of the 24 compounds which were examined.¹ One therefore speaks of a proto-type symmetry group and the various structures can be described to a very good approximation as different intersections of a four-dimensional pattern, all having the same superspace group symmetry. In the commensurate case the actual structure is slightly deformed with respect to this ideal section involving more structural relations than those required by the 3-D space group symmetry. This can give rise to what Opechowski⁸ calls an "exceptional space group". As an illustration, one can think of a monoclinic space group with an orthorhombic lattice translational symmetry. The description of the symmetry group, and of different compounds and of different phases of a given compound by one single group is very appealing as it can make the mutual relations

between the structures more apparent and an understanding of the mechanisms involved in the phase transitions easier.

One can argue that for a commensurate phase, there is no doubt that the 3-D space group gives the right symmetry. On the other hand, it is possible that some hidden symmetries, as those provided by the proto-type symmetry, are overlooked in this way. An example of a crystal structure where the choice between a commensurate superstructure and an incommensurate modulation is difficult, is found in the room-temperature phase of Rb_2ZnBr_4 . The incommensurate phase in this compound has a modulation wave vector $\mathbf{q} = \gamma\mathbf{c}^*$, constant with $\gamma = 5/17$ within the experimental error over a wide temperature range. Nevertheless, the observed X-ray extinction conditions are best described by a superspace group.

In the light of this insight, it is interesting to investigate whether the two (normal versus superspace) descriptions give the same results for symmetry dependent physical properties.

One example is the structure itself, as determined experimentally by means of X-ray scattering. Here symmetry dependent selection rules are found in terms of extinctions of Bragg reflections. For a four dimensional superspace group (as is appropriate for the incommensurate phases of the A_2BX_4 -family) the extinctions are given through conditions on four indices (h, k, l and m) labeling a vector of the four dimensional reciprocal lattice Λ_4^* . When the superspace description is used for the commensurate phases, a comparison with extinction rules as predicted by the three dimensional space groups of these phases, is not simple to characterise in general (see e.g. de Wolff⁹). Pérez-Mato *et al.*¹⁰ argue that in the commensurate case the structural implications of the superspace group symmetry are fully equivalent with those of the 3-D space group. In the view of the present authors, the situation is more complex than that. In any case, from an experimental point of view, it appears very often more convenient to adopt a superspace group characterisation of a modulated structure than to use a superstructure description.¹¹

A second example is the morphology, clearly a symmetry dependent property of crystals, which was investigated by Rasing *et al.*¹² and Dam and Janner⁷ in the case of incommensurate phases. The latter examined three of the five modulated phases of $[\text{N}(\text{CH}_3)_4]_2\text{ZnCl}_4$ and found a clear evidence for the conserved superspace symmetry in these phases, again, not in contradiction with the three dimensional description of the commensurate phases, but moreover, relaxing the ambiguity in indices, which exists when using 3-D space groups, by using the concept of main faces, which are practically independent of the modulation and satellite faces, which

depend strongly on the modulation wave vector. These faces are again labeled by four integers h, k, l and m .

In the case of light scattering (Raman and infrared experiments), the superspace groups were proven to be useful for a prediction of selection rules in both incommensurate phases^{13,14,15} (where they form the only exact tool up to now) and superstructures with a large unit cell.¹⁵ Therefore we wanted to investigate further the selection rules in commensurate phases. For a derivation of selection rules in incommensurate phases see Janssen.¹⁶ One can expect differences between the selection rules predicted by a normal description and a superspace description, when the 3-D point group symmetry of the commensurate phase is lower than the symmetry given by the point group of the superspace group. The most striking differences are expected to occur when the 3-D symmetry is monoclinic or lower, the point group symmetry of the superspace group being orthorhombic, in which case one deals with an exceptional space group. Experimental verification is made through the difference in the number of modes active in a certain polarisation.

Among the twenty four compounds investigated, there are at least 14 structures for which a monoclinic phase has been found. Our choice fell upon $[\text{N}(\text{CH}_3)_4]_2\text{ZnCl}_4$ because of several reasons. First of all this compound can be grown rather easily, resulting in very beautiful colourless crystals, which are fairly easy to handle. Secondly, the compound has two different monoclinic phases between 160 K and 277 K, with relatively small supercells, so one can expect a limited number of rather sharp lines in the spectra. Thirdly the relevance of the superspace description for its morphology has already been shown.⁷

Considerable effort has already been made in Raman and infrared scattering on $[\text{N}(\text{CH}_3)_4]_2\text{ZnCl}_4$ (from now on abbreviated as TMAZC);¹⁷⁻²¹ we will compare our results with that work. This paper is organised as follows. In section 2.5.2 the derivation of the Raman and IR-activity in the normal and the superspace description will be explained. Section 2.5.3 deals with the experimental details and the results of the measurements. In section 2.5.4 the relevant selection rules will be given and the results will be interpreted. We end with a conclusion.

2.5.2. Raman and infrared activity

In this section we will briefly describe the procedure followed to obtain the selection rules for Raman and infrared activity. We will emphasise the differences which result when using ordinary 3-D space groups or superspace groups.

For ordinary crystals, only the phonon modes at $\mathbf{k} = 0$ can be active in a Raman or infrared experiment. Whether a certain phonon branch is active (at $\mathbf{k} = 0$) in either experiment, is determined by the symmetry of the corresponding mode. This symmetry depends on the point group of the crystal. The procedure to find the activity of these modes is described in many text books (see e.g. Hayes and Loudon²²). Often a distinction is made between internal and external modes. The former describe the vibrational motions of the constituents that can be considered as a group, held together by relatively strong bonds (e.g. molecular groups (CH_3) or ions (ZnCl_4^- and TMA^+)). The external modes, then, describe the motions remaining when the internal-mode-groups are considered to be rigid. This latter class can then be divided into rotational and translational modes.

In case of a superstructure, the 3-D point group is used to find the selection rules, although in this case more modes at $\mathbf{k} = 0$ are present due to the (generally) larger unit cell.

The different modes at $\mathbf{k} = 0$ are labeled by irreducible representations of the point group. The actual activity now follows from the transformation properties of the different components of the dipolar moment for infrared absorption and in the case of Raman scattering, of the polarisability tensor. These components are also labeled with the irreducible representations of the point group.

For the internal modes one can construct a correlation diagram,²³ which correlates the symmetry of the internal modes of the free ion (molecular group) and the corresponding ones in the crystal field, via the site symmetry of the ion. This diagram allows for a description of the internal modes in terms of the free-ion modes.

In case of an incommensurate phase, the symmetry is given by the superspace group. For a symmetry description of phonon modes in incommensurate phases see Janssen.¹⁶ If one restricts to the same wave vector labeling as in the corresponding non-modulated case, one finds that the modes at $\mathbf{k} = \pm l\mathbf{q}$, become equivalent with the modes at $\mathbf{k} = 0$ (\mathbf{q} is the modulation wave vector; l integer). In other words, these modes can also become active. They can be labeled by the same irreducible representations as in the non-modulated (basic) structure, when the corresponding

point groups are equivalent (this is not the general case, but it applies to the structure considered here). Due to the incommensurate wave vector, the number of active modes is in principle at least infinite. The intensity, however, decreases very fast with increasing l . The modes with $l = 0$ correspond to modes at $\mathbf{k} = 0$ in the basic structure. In the case of a superstructure which is described with a superspace group, one can distinguish two cases. The first case is the one where the point group of the superstructure is equivalent to the point group of the superspace group that describes the (often high temperature) incommensurate structure. In that case, the atoms are slightly rearranged on going from the incommensurate phase to the superstructure, while keeping the 3-D Euclidean elements of the superspace group; in this case one does not speak of an exceptional space group. The selection rules predicted by the superspace group are the same as the ones predicted by the 3-D point group, in the superstructure phase. An example of such a compound is Na_2CO_3 .¹⁵ The number of inequivalent wave vectors is restricted by the rational value of \mathbf{q} with respect to the basic reciprocal lattice. Hence, in this case, superspace groups are only useful, for a more structured description, making calculations often more elucidated.

The second class of superstructures is the one, where the point group of the superstructure is lower than that of the superspace group (exceptional space group). This case will be relevant in this paper. Hence, the superspace group can only be used as an approximate symmetry description and so also the 3-D exceptional space group. The differences in selection rules between a normal and a superspace description now result from the differences in point group symmetry. For every mode at $\mathbf{k} = 0$, the activity of the modes at $\mathbf{k} = \pm l\mathbf{q}$ of the corresponding phonon branch can be determined with the superspace group. Again, the number of inequivalent \mathbf{k} -vectors is limited due to the commensurate wave vector of the modulation.

A comparison between the two descriptions (normal and superspace) can be made by simply comparing the activity of the different modes in both approaches. In particular, this corresponds to counting the number of spectral lines as observed experimentally in different polarisations and comparing it with the predictions. The actual selection rules for TMAZC will be given in section 2.5.4.

2.5.3. Experimental

2.5.3.1. Crystal preparation

The TMAZC samples used in the Raman and far infrared (FIR) experiments were grown from an aqueous solution of $N(CH_3)_4Cl$ and $ZnCl_2$ in a molar ratio 2:1 by slow evaporation at $30^\circ C$. A small amount of concentrated HCl was added in order to improve growth. The resulting crystals were oriented by means of their morphology and X-rays. The samples used were all cleaved (to obtain faces perpendicular to **a**) or sawed and polished with a little water. They originated all from the same mother crystal. The specimens were platelets with a dimension of approximately $3 \times 4 \text{ mm}^2$ and 0.5–1 mm thick.

2.5.3.2. Raman measurements

For the Raman measurements an Ar^+ -ion laser working at 488 nm was used as an exciting source. The scattered light at 90° was focused on a Spex Industries double grating monochromator with spatial filter (Spex 14018). Photon counting was done with standard PAR equipment. Data were collected with a Digital computer.

The exciting power was 0.25 W. The monochromator was gauged for every spectrum by recording the complete Rayleigh line. The resolution of the monochromator was 1.5 cm^{-1} . Special attention was given to the polarisation directions in the monoclinic phases. $s_i(e_i, e_s)s_s$ is the notation of the polarisation (incoming light along s_i is polarised along e_i ; analogous for the scattered light). If not specified otherwise, the directions are given with respect to the crystallographic axes. Often the vectors s_i and s_s will be omitted. In first instance the complete Raman spectrum (including all internal modes) was measured in each phase for four different polarisations (**a,a**), (**a,b**), (**b,c**) and (**a,c**). Later on the attention was focused on the regions $0-450 \text{ cm}^{-1}$, $730-780 \text{ cm}^{-1}$ and $930-980 \text{ cm}^{-1}$ for reasons which will become clear in the following section. The polarisations (**b,b**), (**a,b**), (**b,c**) and (**a,c**) were chosen for all phases but phase IV, in which latter the polarisations (**a,a**), (**a,b**),

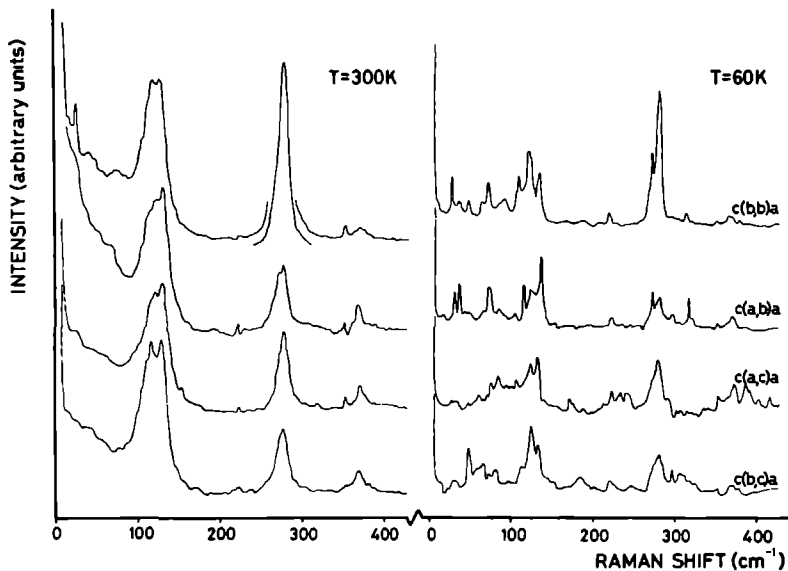


Figure 2.11. The low frequency spectra of TMAZC for the highest (phase I) and the lowest (phase VI) temperatures measured. The external modes can be found for $\omega < 120 \text{ cm}^{-1}$. The indicated polarisations hold for the spectra of both phases. In phase I, for the polarisation (b,b), the mode at 280 cm^{-1} is scaled down by a factor of two.

(a,c) and (b,c) were measured with respect to the principal axes of the indicatrix. The results of the different Raman measurements can be found in Figs. 2.11 and 2.12-a,b and the mode frequencies (which correspond to the peak frequencies) can be found in Table 2-VIII.

TABLE 2-VIII

phase I				phase V				phase VI(150 K)				phase VI(\approx 60 K)			
bb	ab	ac	bc	bb	ab	ac	bc	bb	ab	ac	bc	bb	ab	ac	bc
25		24						26		30		29	32		
												39	37		
												50	49		
												71	74	74	64
												82	93		82
119	121	119	116					118		117		110	115		114
125	131	129	127									123	125	124	124
								131		130		135	136	132	132
													222	223	
														227	
														233	
														242	
				268		272	273	270		270		273	272	273	
278	275	277	276	282	281	281	283	281		282		281	280		280
													317		
371	368	370	369					368		370		369	369	372	370
														387	
				753	753	753	753	752	753	753	752	752	751	752	751
757	756	756	757	756	756	756	757	756	756	756	757	757	756	757	755
												760			
946			947	946	947	947	948	947	947	947	948	946	946	946	946
951	950	948	949	949	949	949	950	949	950	949	950	949	948	949	947
		952	952		952			951			952	951	950	952	950
954		955		954	954	954		954		954	954	954		954	953
				955			956	957	958	956				956	
		958			959	959	960	960	961	959	959	958	957	959	960
												962	961	961	

Table 2-VIII. The peak frequencies (in cm^{-1}) of the external modes, the ZnCl_4^- -internal modes and the ν_1 , ν_2 and ν_3 modes of the TMA^+ -ion, in phases I, V and VI. Only the clearest peaks or shoulders are given.

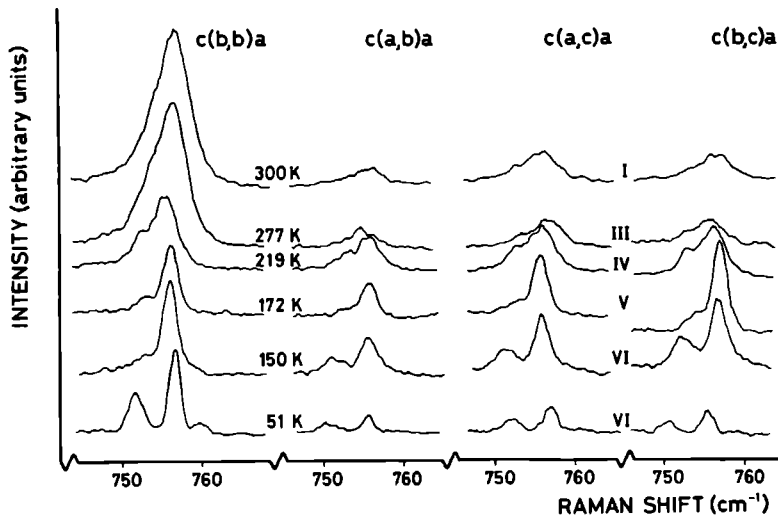


Figure 2.12-a. The ν_1 internal mode of the TMA^+ ion in all phases but the incommensurate one. The Roman literals indicate the different phases. In phase IV, instead of the polarisation (b, b) , (a, a) should be read.

2.5.3.3. FIR measurements

For the far-infrared (FIR) measurements a reflection configuration was chosen, in order to be able to perform polarised measurements (single crystals absorb too strongly to make transmission experiments easy). A Michelson interferometer (Grubb Parsons) was used as a source and a Golay cell as a detector. FIR measurements were limited to approximately 350 cm^{-1} . The polarisation is notated as a, b or c, as to indicate the direction of the electric field with respect to the crystallographic axes. Some FIR-results are given in Fig. 2.13.

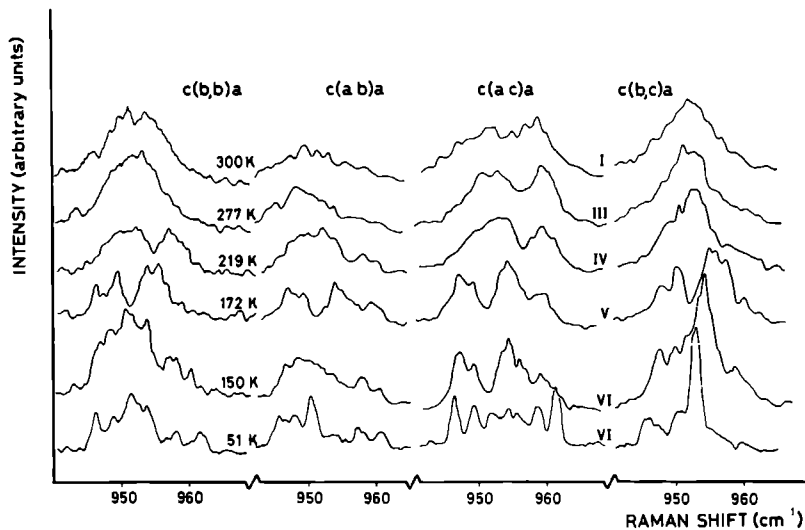


Figure 2 12-b The ν_3 internal mode of the TMA^+ -ion in all phases but the incommensurate one. The Roman literals indicate the different phases. In phase IV, instead of the polarisation (b,b), (a,a) should be read.

2.5.3.4. Indicatrix

Because the commensurate structures of phases IV and V are monoclinic, we can expect the indicatrix to rotate around the unique axis. In order to be able to still perform polarised measurements in these phases, we measured the direction of the principal axes with respect to the crystallographic axes at 488 nm as a function of temperature in the same cryostat as was used for the Raman measurements. This was done by placing the cryostat in between two crossed polaroids and adjusting the latter two for extinction.

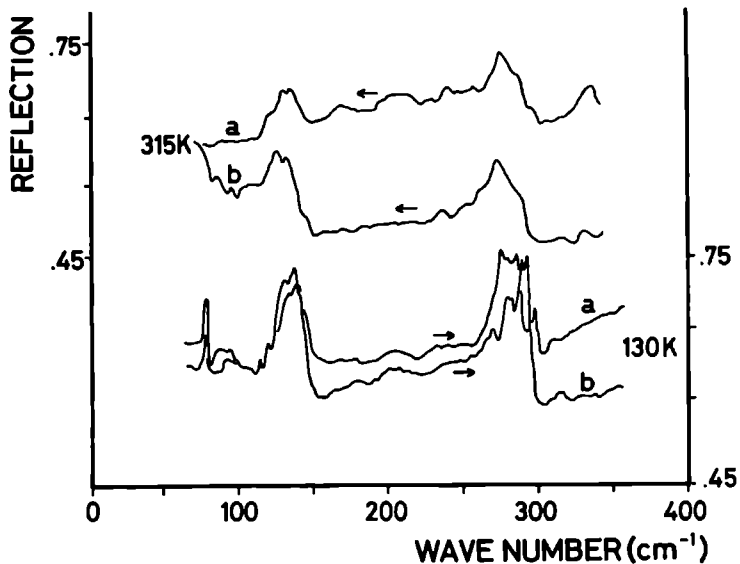


Figure 2.13. The far-infrared reflection spectrum of TMAZC for two temperatures (315 K in phase I and 130 K in phase VI), for two different polarisations (a and b).

2.5.3.5. Temperature control

The samples were mounted in a helium gas flow cryostat, in a copper holder which allowed to exert some mechanical pressure on the crystal in a direction perpendicular to the light beam, thus eliminating domains in phase IV. The sample was held by a stainless steel spring, thermal contact being improved with thermo paste. The temperature of the sample was measured with a chromel constantan thermocouple. We estimate the absolute error in the temperature to be less than $\pm 1^\circ$.

2.5.4. Interpretation

We will start with a short description of TMAZC and give the selection rules for light scattering in the different phases and will then concentrate on the actual spectra.

2.5.4.1. The structure of $[\text{N}(\text{CH}_3)_4]_2\text{ZnCl}_4$

TMAZC has several phases as a function of temperature. The different symmetries and transition temperatures are summarised in Table 2-IX. The

phase	VI	V	IV	III	II	I
T(K)	<161	<181	<276.5	<279	<293	>293
γ	$\frac{2}{3}$	0(?)	$\frac{2}{3}$	$\frac{1}{5}$	inc.	0($Z=4$)
symm.	$P2_12_12_1$	$P2_1/c11$	$P112_1/n$	$Pc2_1n$	$Pcmn(00\gamma)(ss\bar{1})$	$Pcmn$

Table 2-IX. A survey of the different phases occurring in TMAZC. The phase transition temperature, modulation vector ($q = \gamma c^*$) and the space group are given.

structure has been determined in the incommensurate (II) and the lock-in (III) phase.²⁴ For the basic structure one finds at room temperature ($Z = 4$; the hydrogen atoms are not considered; $a = 15.54 \text{ \AA}$, $b = 9.00 \text{ \AA}$ and $c = 12.28 \text{ \AA}$; space group $Pcmn$) that all atoms are at Wyckoff positions $(x, \frac{1}{4}, z)$, except for Cl(3), Cl(5) and Cl(6), which are in a general position. The structure is built up from tetrahedra (ZnCl_4^- and TMA^+), which are more or less rigid ions. Two projections of the orthorhombic cell can be found in Fig. 2.14. The modulation consists mainly of rotations and translations of the different tetrahedra; more details will be given in section 2.5.4.3.

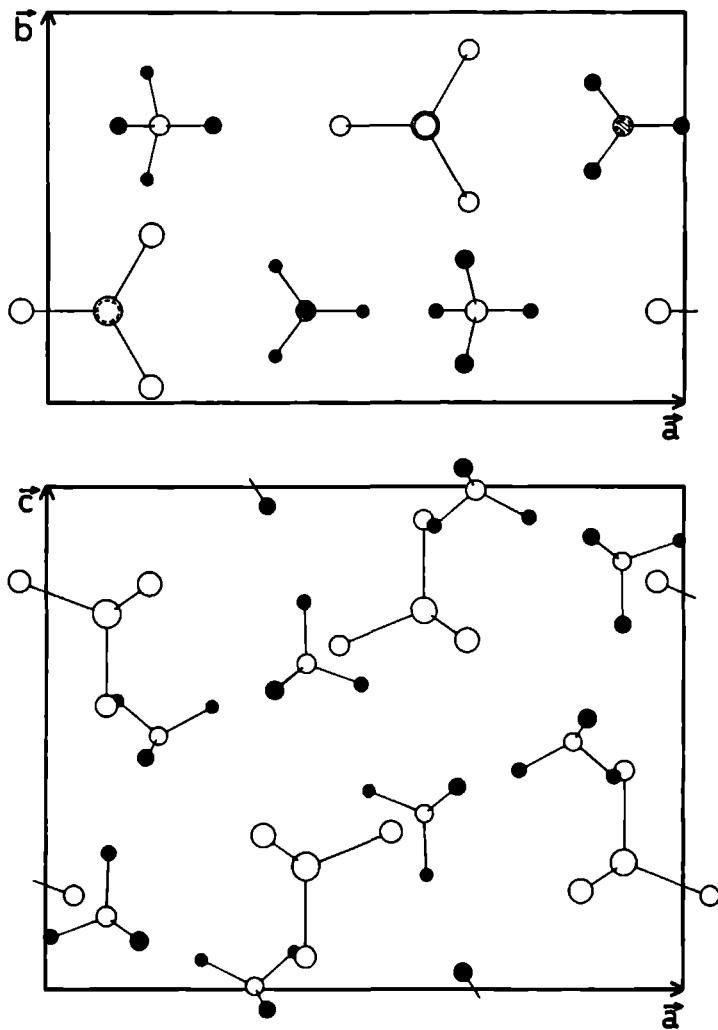


Figure 2.14. Two projections of the unit cell of TMAZC in the para phase. The full circles represent the CH_3 -groups.

TABLE 2-X

$mmm (D_{2h})$	$n(\text{acoust})$	$n(\text{opt tr})$	$n(\text{rot})$	$n(\text{vibr})$	Activity
A_g	0	6	3	18	(a ,a),(b ,b),(c ,c)
B_{1g}	0	3	6	9	(a ,b)
B_{2g}	0	6	3	18	(a ,c)
B_{3g}	0	3	6	9	(b ,c)
A_u	0	3	6	9	
B_{1u}	1	5	3	18	c
B_{2u}	1	2	6	9	b
B_{3u}	1	5	3	18	a

Table 2-X. The number of modes at $k = 0$ transforming according to the different representations of TMAZC in phase I. These results are the same as those for the basic structure of phase II.

2.5.4.2. Raman and infrared activity of the modes

The optical activity of the phonon modes in the different phases of TMAZC has been obtained with the use of normal space groups and superspace groups. A distinction is made between internal modes (vibrations of the constituents of the tetrahedral ions) and external modes (librational and translational modes of the tetrahedra, which are assumed to be rigid for these modes). For the TMA^+ -ions one can again divide the internal modes into two types, one containing all vibrations of the TMA^+ -ion, considering the CH_3 groups as point-like and a second type describing all CH_3 internal and rotational modes. The validity of this distinction will be discussed later on. In our derivation of the activity we have neglected the H-atoms, that is, we consider the CH_3 -groups as rigid spheres. For phases II and III we used the results of Madariaga *et al.*²⁴ We have assumed that the structure of the para phase is equivalent to the basic structure of the incommensurate phase. For phase IV to VI we have assumed that all atoms are in general positions, as in phase III, which is in the case of phase IV supported by the structure determinations of all other A_2BX_4 -members with a $P112_1/n$ -phase (see Ref. 1, Table 4.3.1 for references).

TABLE 2-XI

$m2m (C_{2v})$	$n(\text{acoust})$	$n(\text{opt tr})$	$n(\text{rot})$	$n(\text{vibr})$	Activity
A_1	1	44	45	135	b, (a,a),(b,b),(c,c)
A_2	0	45	45	135	(a,c)
B_1	1	44	45	135	a, (a,b)
B_2	1	44	45	135	c, (b,c)

Table 2-XI. The number of modes at $k = 0$ in phase III of TMAZC.

The results for the phases I to VI are given in Tables 2-X to 2-XV, where the number of modes at $k = 0$ or $k = \pm lq$ ($l = 1,2,3,\dots$), that transform according to the irreducible representations of the relevant space groups, is given. We will use the Mulliken notation for these irreducible representations. In these tables acoust. stands for acoustical, opt. tr. and rot. stand for the translational and librational modes of the (rigid) tetrahedra respectively, while vibr. indicates the internal (vibrational) modes. The activity is given for as well the Raman polarisation configurations as the infrared ones.

TABLE 2-XII

$2/m (C_{2h})$	$n(\text{acoust})$	$n(\text{opt tr})$	$n(\text{rot})$	$n(\text{vibr})$	Activity
A_g	0	27	27	81	(a,a),(b,b),(c,c),(a,b)
B_g	0	27	27	81	(a,c),(b,c)
A_u	1	26	27	81	c
B_u	2	25	27	81	a,b

Table 2-XII. The number of modes at $k = 0$ in phase IV of TMAZC

In the light of the superspace description considered as a good approximation for all phases, we can use the results of Table 2-XV not only in the incommensurate phase. For the commensurate phase with an l -fold superstructure, one can find the number of active modes for each representation by adding the results of the basic structure (Table 2-X) and the additional modes, for every l running over all inequivalent k -vectors; that is, for a five-fold superstructure (phase III) the contributions of $|l| = 1$ and $|l| = 2$ have to be included (Table 2-XV).

TABLE 2-XIII

$2/m (C_{2h})$	$n(\text{acoust})$	$n(\text{opt tr})$	$n(\text{rot})$	$n(\text{vibr})$	Activity
A_g	0	9	9	27	(a, a), (b, b), (c, c), (b, c)
B_g	0	9	9	27	(a, b), (a, c)
A_u	1	8	9	27	a
B_u	2	7	9	27	b, c

Table 2-XIII The number of modes at $k = 0$ in phase V of TMAZC

TABLE 2-XIV

$222 (D_2)$	$n(\text{acoust})$	$n(\text{opt tr})$	$n(\text{rot})$	$n(\text{vibr})$	Activity
A	0	27	27	81	(a, a), (b, b), (c, c)
B_1	1	26	27	81	c, (a, b)
B_2	1	26	27	81	b, (a, c)
B_3	1	26	27	81	a, (b, c)

Table 2-XIV The number of modes at $k = 0$ in phase VI of TMAZC

TABLE 2-XV

$mmm (D_{2h})$	$n(\text{acoust})$	$n(\text{opt tr})$	$n(\text{rot})$	$n(\text{vibr})$	Activity
A_g	0	$9+3(-)^l$	$9-3(-)^l$	$27+9(-)^l$	(a, a), (b, b), (c, c)
B_{1g}	0	$9-3(-)^l$	$9+3(-)^l$	$27-9(-)^l$	(a, b)
B_{2g}	0	$9+3(-)^l$	$9-3(-)^l$	$27+9(-)^l$	(a, c)
B_{3g}	0	$9-3(-)^l$	$9+3(-)^l$	$27-9(-)^l$	(b, c)
A_u	0	$9-3(-)^l$	$9+3(-)^l$	$27-9(-)^l$	
B_{1u}	0	$9+3(-)^l$	$9-3(-)^l$	$27+9(-)^l$	c
B_{2u}	0	$9-3(-)^l$	$9+3(-)^l$	$27-9(-)^l$	b
B_{3u}	0	$9+3(-)^l$	$9-3(-)^l$	$27+9(-)^l$	a

Table 2-XV The number of additional modes at $k = \pm lq$ ($l = 1, 2, \dots$), due to the modulation in phase II of TMAZC For $l = 0$ the numbers are the same as those given in table 2-X

It is, however, more informative to find a correlation between the symmetries of the modes at $k = 0$ and the ones at $k = \pm lq$. We determined this correlation between modes with $l = 0$ and $|l|$ even or odd. The results are given in Table 2-XVI.

For the internal modes one can construct a further correlation diagram, with the help of which one can predict the change in activity of the different free ion vibrations, once embedded in the crystal. The symmetry analysis of the free ion vibrational modes are given in Table 2-XVII. Such correlation diagrams can be found in Figs. 2.15 and 2.16.

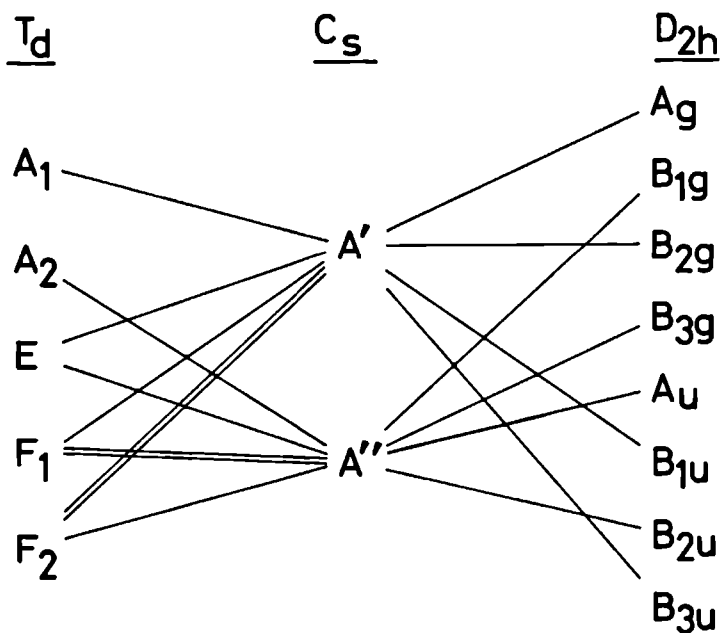


Figure 2.15. The correlation between the free ion tetrahedral symmetry T_d ($43m$) and the crystal symmetry in the para phase D_{2h} (mmm), through the site symmetry C_s (m). For the relevant polarisations see tables 2-X and 2-XVII.

TABLE 2-XVI

$l = 0$	$l = \text{odd}$	$l = \text{even}$
$A_g \rightarrow$	$B_{1g} + A_u \rightarrow$	$A_g + B_{1u}$
$B_{1g} \rightarrow$	$A_g + B_{1u} \rightarrow$	$B_{1g} + A_u$
$B_{2g} \rightarrow$	$B_{3g} + B_{2u} \rightarrow$	$B_{2g} + B_{3u}$
$B_{3g} \rightarrow$	$B_{2g} + B_{3u} \rightarrow$	$B_{3g} + B_{2u}$
$A_u \rightarrow$	$A_g + B_{1u} \rightarrow$	$B_{1g} + A_u$
$B_{1u} \rightarrow$	$B_{1g} + A_u \rightarrow$	$A_g + B_{1u}$
$B_{2u} \rightarrow$	$B_{2g} + B_{3u} \rightarrow$	$B_{3g} + B_{2u}$
$B_{3u} \rightarrow$	$B_{3g} + B_{2u} \rightarrow$	$B_{2g} + B_{3u}$

Table 2-XVI. The correlation between the modes at $k = 0$ and the corresponding ones at $k = \pm lq$ ($l = 1, 2, \dots$), in the superspace description.

As the main aim of this investigation is to analyse the (internal mode) spectra in the normal space group description and the superspace description, a comparison between Table 2-XVI and Figs. 2.15 and 2.16 is appealing. This has been done by calculating the number of modes transforming according to the different irreducible representations of the point group in the superspace description and the normal description (which latter follow from Fig. 2.16 and Table 2-XVII), for the four internal modes in phases III to VI. The results can be found in Table 2-XVIII. As an illustration, we will show how the results for the ν_1 -mode in this table in the case of phase III were obtained. First the superspace result. For phase III the modulation wave vector is $q = \frac{2}{5}c^*$. Therefore, the inequivalent wave vectors $k = lq$

TABLE 2-XVII

$43m (T_d)$	$n(\text{vibr})$	Activity
A_1	$1:\nu_1$	$(a, a) + (b, b) + (c, c)$
A_2	-	
E	$1:\nu_2$	$((a, a) + (b, b) - 2(c, c), (a, a) - (b, b))$
F_1	-	
F_2	$2:\nu_3, \nu_4$	$a, b, c, ((a, b), (b, c), (c, a))$

Table 2-XVII. The symmetry of the modes of the free tetrahedral ion.

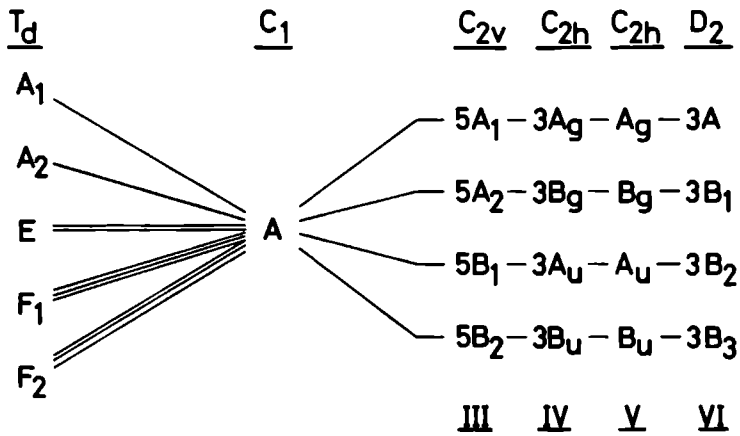


Figure 2.16. The correlation between the free ion tetrahedral symmetry T_d ($\bar{4}3m$) and the symmetry of the different commensurate phases, through the site symmetry C_1 (I). For the relevant polarisations see tables 2-XI to 2-XIV and 2-XVII.

are $\mathbf{k} = 0$, $\mathbf{k} = \pm\mathbf{q}$ and $\mathbf{k} = \pm 2\mathbf{q}$. The free-ion symmetry of the ν_1 -tetrahedral mode is A_1 (Table 2-XVII). In Fig. 2.15 we find that for the basic structure corresponding to $l = 0$, this mode splits into $A_g + B_{2g} + B_{1u} + B_{3u}$. In Table 2-XVI we find that the symmetry of the corresponding modes at $\mathbf{k} = \pm\mathbf{q}$ is $2B_{1g} + 2B_{3g} + 2A_u + 2B_{2u}$. For the modes at $\mathbf{k} = \pm 2\mathbf{q}$ the table gives $2A_g + 2B_{2g} + 2B_{1u} + 2B_{3u}$. If we take these results together and write them in terms of polarisations instead of irreducible representations, we find the results as given in the first column of Table 2-XVIII. For the normal description, Fig. 2.16 shows that the ν_1 -mode in phase III will split into four quintuplets. Each quintuplet, transforming according to one of the irreducible representations of the 3-D point group ($m2m$). In Table 2-XI we then find that in every polarisation, one can find exactly five modes, which is in agreement with the underlined result in Table 2-XVIII. For the doubly degenerate (E -symmetry) ν_2 -mode we find in Fig. 2.15 that it splits into eight lines equally distributed over all symmetries. This is the reason for the correspondingly equal

pol.	phase III			phase IV			phase V			phase VI			mmm
	v ₁	v ₂	v ₃ ,v ₄	v ₁	v ₂	v ₃ ,v ₄	v ₁	v ₂	v ₃ ,v ₄	v ₁	v ₂	v ₃ ,v ₄	
(a,a)	3	5	8	1	3	4	1	1	3	1	3	4	A _g
(a,b)	2	5	7	2	3	5	0	1	1	2	3	5	B _{1g}
(a,c)	3	5	8	1	3	4	1	1	3	1	3	4	B _{2g}
(b,c)	2	5	7	2	3	5	0	1	1	2	3	5	B _{3g}
—	2	5	7	2	3	5	0	1	1	2	3	5	A _u
c	3	5	8	1	3	4	1	1	3	1	3	4	B _{1u}
b	2	5	7	2	3	5	0	1	1	2	3	5	B _{2u}
a	3	5	8	1	3	4	1	1	3	1	3	4	B _{3u}
each	<u>5</u>	<u>10</u>	<u>15</u>	<u>3</u>	<u>6</u>	<u>9</u>	<u>1</u>	<u>2</u>	<u>4</u>	<u>3</u>	<u>6</u>	<u>9</u>	

Table 2-XVIII. The number of active internal modes in the different commensurate superstructures of TMAZC in the superspace description for each polarisation (pol.). The corresponding numbers in the normal description are underlined; in this case these numbers are the same for each polarisation. (a,a) stands for the polarisations (a,a), (b,b) and (c,c), respectively. The most right column gives the irreducible representations of the superspace point group.

distribution of this mode over all polarisations in Table 2-XVIII. As mentioned before, the validity of both descriptions can be tested by counting the number of modes (spectral lines) in the different polarisations.

At this point it is worth while to mention the problem of how to interpret the indicatrix of a monoclinic 3-D structure in an orthorhombic superspace description. Due to the relatively large rotations of the indicatrix (see section 2.5.4.4) as compared to the monoclinic angles ($\gamma = 90.3^\circ$ in phase IV and $\alpha = 90.02^\circ$ in phase V), a direct Raman or infrared measurement in a single polarisation is impossible. Let us remark that the deviations from 90° are a measure for the slight deformation in a superspace group description. For the monoclinic description with (say) c as the unique axis, there is no need to make any difference between a and b-polarised infrared spectra, as the modes for both will be equivalent. In the superspace description on the other hand, the difference between both polarisations is essential, but light polarised along the crystallographic a-axis, will be rotated while passing the crystal due to the birefringence. So one has to polarise the light along a principal direction of the indicatrix, as was done in phase IV in our measurements.

The consequence is that one measures spectra of two polarisations in such a case. The sample used in the measurements of phase IV, was oriented thus, that the crystallographic **a** and **b**-axes were rotated over 15° with respect to the polarisation directions **a** and **b**, which are used to indicate the different spectra. Due to this rotation, the (b,c) and (a,c)-spectra will contain a mixture of B_{2g} and B_{3g} -modes, while the (a,a) and (a,b)-spectra will be built up of both A_g and B_{1g} -modes. This admixture of unwanted modes amounts approximately 25 % for the polarisations (a,b), (a,c) and (b,c), while in the case of the polarisation (a,a), even approximately 45 % of the B_{1g} -character is present. These percentages are merely indicative.

2.5.4.3. Analysis of the spectra

Before turning our attention to the actual aim of this work (studying the difference in normal versus superspace description), we will give a general view of the spectra of the compound.

2.5.4.3.1. External modes

In the external mode regime ($\omega < 120 \text{ cm}^{-1}$ in Fig. 2.11), we see at high temperatures broad lines except for a sharp peak at $\omega = 25 \text{ cm}^{-1}$ in the polarisation c(b,b)b. The broad lines become sharper at lower temperatures. In fact this can be explained by an almost unhindered rotation of the TMA^+ -ions, which was also suggested by Blinc *et al.*²⁵ This can be understood if we compare the ion radii of the two tetrahedra ($r(\text{TMA}^+) \ll r(\text{ZnCl}_4^-)$) and their mass difference, resulting in relatively big holes for the TMA^+ -ions allowing a large freedom of motion between fairly hard potential walls. Due to this one can expect that higher harmonics in the dynamics play an important role. For lower temperatures, these motions freeze out. Unfortunately, Madariaga *et al.*²⁴ give no thermal parameters. Less recent work by Wiesner *et al.*²⁶ in which probably the average room structure is determined, gives clearly larger thermal parameters (on the average approximately two times larger) for the carbon atoms compared to the ZnCl_4^- constituents. Care must be taken however, because for the thermal parameters along the modulation polarisation, one can expect larger values when an average structure determination is performed, the

effects of a static displacive modulation simulating a contribution to the dynamical thermal motion. Blinc *et al.* find that the free rotations of the TMA⁺-ion freeze out at the phase transition to phase VI ($T = 161$ K), while the CH₃-groups still rotate around their C₃-axis. Nevertheless, also for the lowest temperatures, the external modes spectrum is too difficult to analyse. The sharp line at 25 cm⁻¹, however, is rather striking, being present for all phases in the polarisations (a,a) and (b,b), and not or much weaker in the other polarisations measured. This mode must be connected with motions of the ZnCl₄²⁻-lattice, because of the sharpness of its line form. In conclusion, the external modes are not very suited for our analysis.

2.5.4.3.2.1. Internal modes

The internal modes can be divided into several groups of lines at relatively high frequencies with respect to those of the external modes. The first group contains all six clusters of modes above 1000 cm⁻¹, which are identified as rotational and vibrational modes of the CH₃-groups. They will not be treated here being difficult to interpret in terms of selection rules. They contain however some information on the rotational degree of freedom of the CH₃ and TMA⁺-ions as was discussed in Refs. 11-13.

The internal modes of the ZnCl₄²⁻-ion can be found as two groups of modes at 132 and 277 cm⁻¹. Those of the TMA⁺-ion as four groups at approximately 370 (ν_2), 460 (ν_4), 757 (ν_1) and 954 cm⁻¹ (ν_3). The identification with the different normal modes of the TMA⁺-ion is after Edsall.²⁷ The assignment of the internal modes of the ZnCl₄²⁻-ion is more difficult and will be given in the next section. We will now treat the internal modes of the two ions in some more detail.

2.5.4.3.2.2. The ZnCl₄²⁻-ion

If we compare Fig. 2.15 with Tables 2-X and 2-XVII, we see that the ν_1 -mode should not be active in the polarisations (a,b) and (b,c) in phase I. Looking at the spectra, we nevertheless do find a nonzero intensity in these cases. This can be due to several reasons:

- The selection rules are not obeyed due to free rotations of the ZnCl_4^- , lowering the actual site symmetry.
- The ion is deformed to such an extent that the symmetry is lower.
- The ν_1 and another internal mode are accidentally degenerate.

The first reason is very unlikely due to the large ion radius of the ZnCl_4^- -ion, compared to the TMA^+ -ion, that is, the rigid lattice will be built up of ZnCl_4^- -ions. The second reason is falsified by the structural analysis of Madariaga *et al.*;²⁴ they find interatomic distances for the Zn-Cl bonds in the incommensurate phase, which differ always less than 2.5 % from the average tetrahedral configuration. The last reason is more likely to be true, because the ν_3 and the ν_1 modes have comparable frequencies in other compounds (e.g. Rb_2ZnCl_4 ²⁸). In order to check this possibility we measured the FIR polarised reflection spectra of TMAZC in the ν_1 -region. Table 2-X and Fig. 2.15 show that the ν_1 -mode is not active in the **b**-polarised spectra. The FIR spectra show a mode in as well the **a** as the **b**-polarised spectra at approximately 280 cm^{-1} ($T = 315 \text{ K}$), with comparable intensities (Fig. 2.13). Hence we expect the ν_3 mode to be strong in the FIR spectra and weak but manifest in the Raman (**a,b**) spectrum. The ν_1 -mode is probably weak in the FIR because of the high symmetry of this mode. Its free ion symmetry allows for only Raman activity, while the ν_3 -mode is both Raman and infrared active for the free ion. Due to the small coupling with the lattice of such an internal mode, this high symmetry is practically conserved in the crystal field (cf. Ref. 10). The consequence of the accidental degeneracy of the ν_1 and the ν_3 -mode is that the former can not be used for our purpose. Moreover, any search for the selection rules to be obeyed by the degenerate ν_1 and the ν_3 -modes is difficult. At the lowest temperature (60 K) the ν_1 -mode, though less broad, is still not resolved completely. In the (**b,b**)-spectrum two lines are resolved which are also present, but less clear, in the three other polarisations. These two lines are also present in phase V (172 K) but not in phase IV (219 K). Again, the ν_3 -mode will be present in this region, making an interpretation very difficult. In the off-diagonal spectra at $T = 60 \text{ K}$, one can see much structure in the neighbourhood of the ν_1 -mode, indicating that the ν_3 and the ν_1 -mode are less degenerate in this phase.

A comparable problem arises for the ν_2 and the ν_4 modes, which lie at approximately 132 cm^{-1} . For these modes also the frequencies almost coincide. On the other hand, their frequencies are so low that one can expect that they behave more as lattice (external) modes than as internal modes and moreover, that the external modes coincide with the ν_2 and ν_4 -modes. Therefore, also the ZnCl_4^- -

internal modes are not adequate for our purpose.

2.5.4.3.2.3. The TMA⁺-ion

For the TMA⁺-ion also the ν_1 -mode ($\omega \approx 755 \text{ cm}^{-1}$) is the one most suited for a study of the selection rules. Also in this case however, (see Fig. 2.12-a) we find a nonzero intensity in every Raman configuration. Referring to the reasoning given in the former section, we can not use the third reason, because for TMA⁺ all internal modes have frequencies which mutually differ considerably. The first reason however, is more likely in this case, as was already mentioned in section 2.5.4.3.1. The rotational motions of the TMA⁺-ion blur the picture, also for the other internal modes. At lower temperatures these rotations freeze out, which is clearly visible, when we compare the spectra for different temperatures. At 219 K (phase IV) we already see a low-frequency shoulder, which results in two peaks at 60 K, where the (b,b)-spectrum even has three lines.

The ν_3 -mode of the TMA⁺-ion ($\omega \approx 955 \text{ cm}^{-1}$, Fig. 2.12-b) is at room temperature already split in two broad lines with some structure, for the polarisation (a,c), probably corresponding to the two sites of the ion. The other polarisations show one very broad line with some structure. In phase III the same can be observed. In phase IV (219 K) all polarisations show this doublet, while in phase V (172 K), one sees already many resolved lines which in phase VI results in a cluster of many (up to seven) lines. One line in this cluster is very pronounced in the (b,c)-spectrum and, though less clear, in the (a,c)-spectrum. The two other internal modes (ν_2 and ν_4) are too weak or too broad to be useful for our purpose.

Because the free rotations are expected to be frozen out in phase VI, we will first concentrate on the low-temperature spectra. For the ν_1 -mode we can find in Table 2-XVIII that the number of lines expected in the superspace description is (note that the entries of this table have to be multiplied by two because of the two sites present for the TMA⁺-ion in the basic structure) two for the polarisation (b,b) and (a,c) and four for (a,b) and (b,c). The normal description predicts six lines in all polarisations. The spectra reveal no difference between the different off-diagonal polarisations as concerning the number of lines; always two lines are present. The polarisation (c,c), however, reveals three lines, which is in contradiction with the superspace description.

For the ν_3 -mode, Table 2-XVIII predicts for the superspace description eight lines in polarisation (b,b) and (a,c) and ten lines in (a,b) and (b,c), the normal description predicting 18 lines in every polarisation. For this mode, the spectra always show less than eight lines, so no hard conclusion can be drawn.

If we look at phase V, we find for the superspace description in Table 2-XVIII for the mode ν_1 , that no lines are expected in polarisation (a,b) and (b,c), while two lines are expected in (b,b) and (a,c). This prediction is in clear contradiction with the measurements, which show two lines (one strong line and a weak shoulder) in every polarisation. This number of lines is exactly what the normal description predicts and in fact would imply that these two lines represent the two sites of the ion. On the other hand, the latter conclusion is not very reliable, first of all because of the possible presence of a rotational degree of freedom for the TMA⁺-ion in this phase and secondly because of the presence of domains. We can expect to have admixture of unwanted modes, analogously to what was described for phase IV in section 2.5.4.2. In phase V we also measured spectra for polarisations $c(a, b_{\pm\chi})a$ (where the index χ indicates a vector parallel to the principal axis of the indicatrix of either domain (\pm)), but found no appreciable difference in intensities for the two peaks. Therefore we expect that contributions of both kinds of domains are equally present in the spectra of this phase. In phases IV and III the number of spectral lines is always significantly smaller than the number of active modes; so again, no conclusion can be drawn.

2.5.4.4. The indicatrix in the monoclinic phases

We will now devote some attention to the monoclinic phases IV and V. As was observed under a polarising microscope, in these phases the samples obtain domains that differ in the value ($90^\circ + \delta$ or $90^\circ - \delta$) for the monoclinic angle (γ in phase IV and α in phase V). The domain walls lie in the (b,c)-plane in phase IV and in the (a,b)-plane in phase V. Hence it seems that the b-axis stays fixed to the bulk sample, while in one phase, the unique axis of the other phase rotates. In the solid solution TMAZnCl_{4-x}Br_x Colla *et al.*²⁹ also found a monoclinic phase (VII) with the unique axis along **b** for x between 1 and 2.5. The domains formed on going from the incommensurate phase to this phase VII were different from the ones obtained on heating from phase VII to IV. In our case, in both phases (IV and V), the

domains formed a fairly regular one dimensional lattice of slabs extending throughout the samples with a thickness of 0.15-0.20 mm, when a fresh (unstressed) crystal was used. The rotation of the indicatrix in phase IV can be found in

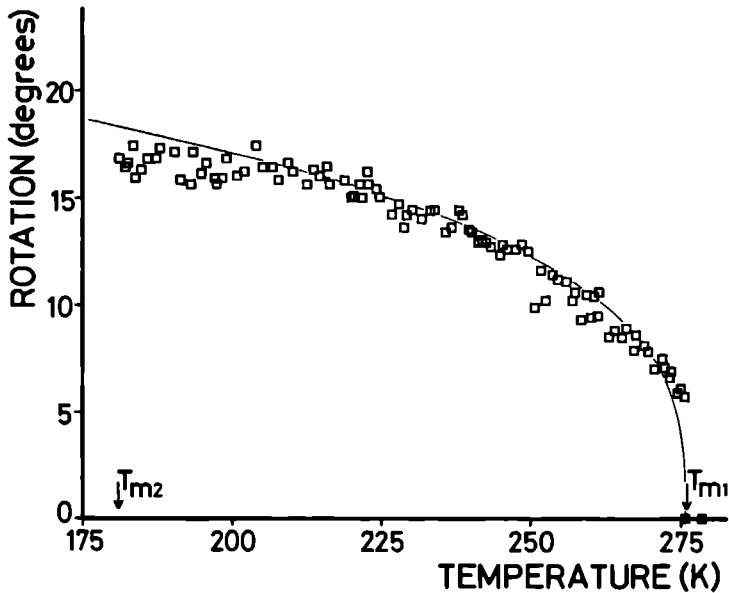


Figure 2.17 The deviation angle (γ) of the indicatrix for white light in phase IV. The solid line is a fit to $\gamma = A(T_{m1} - T)^\beta$, for temperatures above 220 K. At the phase transition to phase V, γ goes very fast to zero again.

Fig. 2.17 The results of the orientational measurements for the indicatrix show that the latter rotates over considerable angles compared to the deviation of the lattice from the orthorhombic symmetry ($<0.3^\circ$), in phase IV the maximum rotation is approximately 17° , in phase V about 29° ($\alpha \approx 0.02^\circ$). On going from phase III to IV, the angle γ increases approximately according to $\gamma = A(T_{m1} - T)^\beta$, where γ is the deviation from the orientation in the orthorhombic phase and T_{m1} is the phase transition temperature (phase III to IV). The values for A , β and T_{m1} were obtained from a fit to the data for temperatures above 220 K. The result was

$A = 4.48 \text{ }^\circ\text{K}$, $\beta = 0.30$ and $T_{m1} = 276 \text{ K}$. The value of the exponent is in fair agreement with the theoretical result of Le Guillou and Zinn-Justin,³⁰ which is 0.325 for a second order transition, although the actual transition is of first order. Below 220 K the rotation starts to deviate from the fit, probably a precursor for the phase transition to phase V. Just above T_{m2} (phase IV to V), γ diminishes very fast to zero again and at the same time the corresponding angle α of phase V increases very rapidly to its maximum value and stays constant down to the phase transition to phase VI, where its value is again zero, in agreement with the orthorhombic symmetry. The domains in phase IV can very easily be enlarged or made smaller by applying a slight pressure along a direction inclined to the crystallographic axes and perpendicular to the unique axis. In this way one can easily make a single domain crystal, which stays in that state when the temperature is not too close to T_{m1} or T_{m2} , even when the pressure is removed. After some mechanical pressure was experienced, the domains often tended to stay bigger, destroying the regular pattern even when the crystal was heated to phase III and afterwards stresslessly cooled again. These domains and the effect of some pressure can be seen in Fig. 2.18. In phase V however all samples which were used broke into pieces even before any movement of the domain walls was observed.

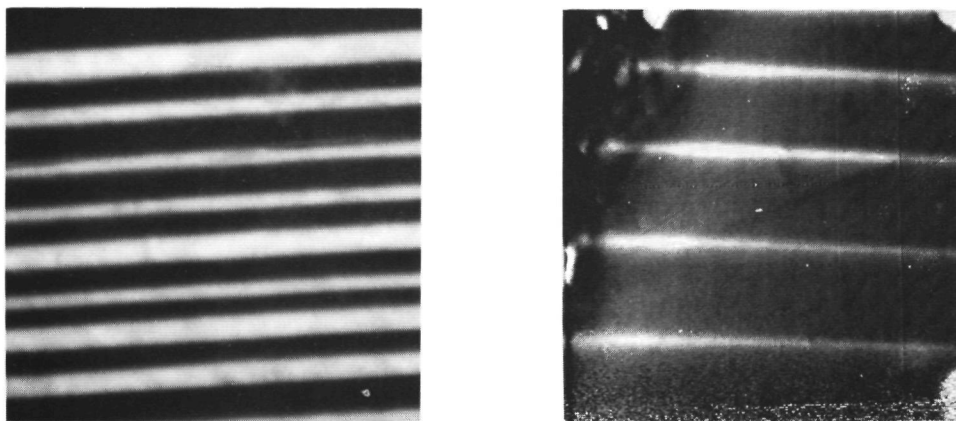


Figure. 2.18. Two photographs of the domains in phase IV of TMAZC. On the left, a strainless crystal is seen, while on the right, one of the two types of domains is favoured after some mechanical pressure has been exerted.

From these observations we can conclude that phase IV is ferro elastic. The same should hold for phase V, but here the effects are not observable. The enormous difference between phase IV and phase V as the sensitivity to external stress is concerned, indicates that the mechanisms for the corresponding phase transitions differ. The domain size seems not to depend so much on the defects or the relevant defects are already quite regularly distributed in a fresh sample.

Let us illustrate the role of the superspace symmetry in phase IV. In terms of the superspace group $Pcmn(00\gamma)(ss\bar{1})$, the only symmetry conditions which influence the rotations of the tetrahedra around c , which will be the cause of the rotation of the indicatrix are $(c_x|s)$ and $(m_y|s)$, which combine a mirror operation perpendicular to \mathbf{a} respectively \mathbf{b} with a phase shift of π in the internal space. The mirror perpendicular to c is conserved in this phase. In other words, the modulation of the mirror atoms has the opposite sign for odd harmonics in the modulation function and the same sign for even harmonics. For a three fold superstructure as is the case in phase IV of TMAZC, the rotations of the tetrahedra due to the modulation can always have a nonzero net value for every three (basic) cells. For a two fold superstructure this is only possible when even harmonics have an appreciable contribution to the modulation. An example of the latter structure is found in TMAMnCl₄, which has a monoclinic phase with a two fold super cell. The maximum rotation of the indicatrix in this compound has been observed to be 20°. ³¹ But the unique axis in this phase is \mathbf{b} , therefore the superspace elements $(c_x|s)$ and $(n_z|\bar{1})$ determine the rotation of the different tetrahedra. Thus, depending on the phase of the modulation, the inversion in the internal space can still account for a net rotation of the tetrahedra in the twofold supercell without even harmonics playing an important role in the modulation. Coming back to the superspace symmetry, one sees that in principle the tetrahedra can rotate without destroying the superspace symmetry, even leaving a net rotation for every supercell. These rotations can be rather large. In the solid solution $[\text{N}(\text{CH}_3)_4]_2\text{ZnCl}_{18}\text{Br}_{12}$ Colla *et al.* ³² found rotations of the TMA⁺-tetrahedra of 20° while the monoclinic angle was only 0.57°. The very small monoclinic deviation of the lattice can thus be considered as a secondary effect.

2.5.5. Conclusion

We have derived the light scattering selection rules for $[\text{N}(\text{CH}_3)_4]_2\text{ZnCl}_4$ (TMAZC) in all phases for both a normal space group and superspace description. In principle the superspace results can be applied to all members of the A_2BX_4 -family with the superpace group $Pcnn(00\gamma)(ss\bar{1})$, although the results are only approximately true, in case of a superstructure with a lower symmetry. For the lattice, a normal description is possible, but one has to take into account the actual space group symmetry ($Pcnn$, $Pc2_1n$, $P112_1n$, $P2_1c11$ and $P2_12_12_1$ respectively).

Furthermore, we have measured the complete Raman spectra of TMAZC in all phases, with special attention for the ν_1 -mode of the ZnCl_4^- -ion and the ν_1 and ν_3 -modes of the TMA^+ -ion.

An interpretation of the measurements in order to be able to decide whether the normal or the superspace description is better suited for light scattering experiments in the commensurate phases, turned out to be difficult, due to several reasons:

- The large number of particles in the unit cell combined with the free rotational motions of the TMA^+ -ions makes the external mode spectra too difficult to interpret.
- The internal modes of the ZnCl_4^- -tetrahedron are pair-wise almost degenerate, making it difficult to verify the selection rules.
- The free rotations of the TMA^+ -ion in all but the lowest temperature phase too, prohibit a clear verification.
- Finally, the spectra of the CH_3 -molecular vibrations and rotations are too complicated for our purpose.

In spite of these drawbacks, the results for the ν_1 -internal mode of the TMA^+ -ion in phase VI seem to indicate that the normal space group provides a better description.

This implies that the deviations from the ideal proto-type symmetry are relevant for the light scattering spectra. As the monoclinic phases are concerned, we have observed and explained that as a result of the approximate superspace symmetry, in spite of the nearly conserved orthorhombic lattice, the indicatrix rotates (as it is allowed to do freely around the unique axis in a 3-D monoclinic structure) over considerable angles. The monoclinic domains are observed to be very stress dependent in phase IV, while in phase V, they did not respond at all to any stress.

Because the investigation presented is not fully conclusive as the choice between a normal space group or a superspace description is concerned, we would like to suggest a further study of the subject. A more suitable candidate from the A_2BX_4 -family should preferably have a low temperature orthorhombic phase with a small supercell and no small ions as to have a rigid lattice. A study of a commensurate monoclinic phase in such a compound is also interesting, because of the selection rules and also because of the question of the interpretation of the indicatrix in Raman and infrared measurements.

Acknowledgements

This work is part of the research program of the Stichting voor Fundamenteel Onderzoek der Materie (Foundation for Fundamental Research on Matter) and was made possible by financial support from the Nederlandse Organisatie voor Zuiver-Wetenschappelijk Onderzoek (Netherlands Organisation for the Advancement of Pure Research).

References

1. A. Hogervorst, thesis, Delft (1986).
2. T. Janssen, *Ferroelectrics* **66**, 203 (1986).
3. S. Plesko, R. Kind and H. Arend, *Phys. status solidi A* **61**, 87 (1980).
4. P. Muralt, H. Arend, H. Altermatt and G. Chapuis, *Ferroelectrics* **56**, 7 (1984).
5. P.M. de Wolff, *Acta Cryst. A* **33**, 493 (1977).
6. A. Janner and T. Janssen, *Phys. Rev. B* **15**, 643 (1977) and A. Janner and T. Janssen, *Acta Cryst. A* **36**, 399 and 408 (1980).
7. B. Dam and A. Janner, *Acta Cryst. B* **42**, 69 (1986).
8. Opechowski, *Crystallographic and Metacrystallographic Groups* (North Holland, Amsterdam, 1986).
9. P.M. de Wolff, *Easy and Uneasy Superspace Groups*, lecture during the International Conference on Advanced Methods in X-ray and Neutron Analysis of Materials, 5-9 oktober 1987, Karlovy Vary (Czechoslovakia), to be published.
10. J.M. Pérez-Mato, G. Madariaga, F.J. Zuñiga and A. Garcia Arribas, *Acta Cryst. A* **43**, 216 (1987).
11. See e.g. Y. Valentine, O.B. Cavin and H.L. Yakel, *Acta Cryst. B* **33**, 1389 (1977).
12. A. Janner, Th. Rasing, P. Bennema and W.H. van der Linden, *Phys. Rev. Lett.* **45**, 1700 (1980) and Th. Rasing, thesis, Nijmegen (1982).
13. Th. Rasing, P. Wyder, A. Janner and T. Janssen, *Phys. Rev. B* **25**, 7504 (1982).
14. P. Echégut, F. Gervais and N.E. Massa, *Phys. Rev. B* **30**, 6039 (1984).
15. H. Meekes, Th. Rasing, P. Wyder, A. Janner and Th. Janssen, *Phys. Rev. B* **34**, 4240 (1986).
16. T. Janssen, *J. Phys. C* **12**, 5381 (1979).
17. V. Srinivasan, C.K. Subramanian and P.S. Narayanan, *Ind. J. Pure Appl. Phys* **21**, 271 (1983).
18. Somnath Ganguly, K.J. Rao, C.N.R. Rao, *Spectrochim. Acta* **41A**, 307 (1985).

19. Mahendra Pal, Anshu Agarwal, D.P. Khandelwal and H.D. Bist, *J. Raman Spectr.* 17, 345 (1986).
20. S.H. Tang, E.C. Looi and R. Radhakrishna, *Phys. Stat. Sol. (b)* 135, 519 (1986).
21. A.M. Bon, R. Almairac, P. Nassiri, C. Benoit and J.L. Ribet, *Phys. Stat. Sol (b)* 101, K87 (1980).
22. W. Hayes and R. Loudon, *Scattering of Light by Crystals* (J. Wiley & Sons, New York, 1978).
23. G. Turrell, *Infrared and Raman Spectra of Crystals* (Academic Press, London, 1972).
24. G. Madariaga, F.J. Zuñiga, J.M. Pérez-Mato and M.J. Tello, *Acta Cryst.* B43, 356 (1987).
25. R. Blinc, M. Burgar, J. Slak, V. Rutar and F. Milia, *Phys. Stat. Sol. (a)* 56, K65 (1979).
26. J.R. Wiesner, R.C. Srivastava, C.H.L. Kennard, M. DiVaira and E.C. Lingafelter, *Acta. Cryst.* 23, 565 (1967).
27. John T. Edsall, *J. Chem. Phys.* 5, 225 (1937).
28. Mitsuo Wada, Akikatsu Sawada and Yoshihiro Ishibashi, *J. Phys. Soc. Japan* 47, 1185 (1979).
29. E.L. Colla, thesis, E.T.H. Zürich, 1987.
30. J.C. Le Guillou and J. Zinn-Justin, *Phys. Rev.* B21, 3976 (1980).
31. Hiroyuki Mashiyama and Sigetosi Tanisaki, *J. Phys. Soc. Japan Letters*, 50, 1413 (1981).
32. E. Colla, V. Gramlich and W. Petter, *Acta Cryst.* C43, 1070 (1987).

CHAPTER 3

OPTICAL ACTIVITY IN MODULATED CRYSTALS

3.1. Introduction

Optical activity is a phenomenon which was discovered in the early days of crystal optics. In 1811, Arago found, that for light traveling along the optic axis of a quartz crystal which was placed between two crossed polarisers, the emerging light has an intensity differing from zero, despite the absence of birefringence for that direction. This phenomenon was found to be due to a rotation of the polarisation around the direction of the beam, the angle of rotation being proportional to the thickness of the specimen. The size of the effect is in general much smaller than that of the ordinary birefringence. Therefore, optical activity (or gyration) is notably more difficult to observe or determine quantitatively than the birefringence itself; an exception being the case where the birefringence is already very small or zero (i.e. in the neighbourhood of or along an optic axis).

The interest in optical activity in modulated structures has two reasons. First of all optical activity is a symmetry dependent property of crystals. For normal crystals, thus commensurately modulated structures included, the occurrence of gyration effects can very well be predicted using the (point) group symmetry of the crystal.¹ In incommensurate phases however, the phenomenon is known to exist, but an exact prediction of the effect merely on grounds of symmetry arguments has not been available yet. It is therefore of interest to check whether the superspace symmetry of such phases can replace the missing space group symmetry. This is already confirmed for X-ray structure determinations. The point is that for optical activity the relevant symmetry properties of the crystal are observed on a scale of the wavelength of the light used, this in contrast to for example X-ray diffraction measurements, which probe the symmetry on a scale of the coherence length of X-rays. A second reason for studying optical activity in incommensurate phases stems from the fact that for normal crystals the effect is believed to be due to structural properties which influence the propagation of light with an essentially non-zero wavelength. A consequence is that optical activity and the normal dielectric properties of crystals differ as their tensor forms are concerned. The tensor of the dielectric constant only depends on the crystal system, while the gyration tensor has different forms for different point group symmetries. In other words, the normal dielectric constant is, besides resonance effects due to phonons or electronic transitions, in principle wave length independent. Optical activity on the other hand vanishes when the wave length of the light (λ) becomes infinite; the size of the effect being proportional to (a/λ) , where a is the lattice constant.

In an incommensurate crystal, it is not a priori clear what takes over the role of this lattice constant, but anyway, structural periodicities are nevertheless present, even on a larger scale than in ordinary crystals. Therefore, the magnitude of the effect is expected to be much larger, albeit that the structural effects of the modulation are mostly very small. A class of materials with properties comparable to incommensurate structures is formed by liquid crystals, where one finds many examples of phases, where ordering takes place on scales, large compared to the ordinary lattice constants. In liquid crystals, optical activity has therefore been studied to a large extent, both theoretically and experimentally.² Very large values, compared to e.g. those in quartz, of the gyration coefficient have been observed in liquid crystals.

Returning to incommensurate crystals, we will study the effect using the superspace approach to predict the occurrence of optical activity from a theoretical point of view and relate the results to experimental data obtained for Rb_2ZnBr_4 .

We will first give a brief description of how the gyration effect can be explained on the basis of Maxwell's equations, without specifying a microscopic theory which accounts for the actual effect. After this introduction, a description will be given of a method which allows for the measurement of optical activity along any crystalline direction, even for relatively small values of the gyration. This method was introduced by Kobayashi *et al.*³⁻⁵ who developed an instrument designated as High Accuracy Universal Polarimeter (HAUP). Finally, we will introduce the superspace symmetry to the problem in a section dealing with the observed effect in Rb_2ZnBr_4 . As the theory of optical activity is concerned we would like to refer in particular to Sommerfeld⁶ and Born.⁷

3.2. Optical activity

The phenomenon optical activity is understood to be caused by a non-local dependence of the displacement field \mathbf{D} , on the electric field \mathbf{E} . In a Taylor expansion this reads

$$D_j(\mathbf{r}, t) = \epsilon_{jk}(\mathbf{r})E_k(\mathbf{r}, t) + \gamma_{jkl}(\mathbf{r})\partial_l E_k(\mathbf{r}, t), \quad (3-1)$$

where ϵ_{jk} is the normal dielectric tensor and γ_{jkl} is a tensor of rank three, which we will call the gyration tensor. We use the Einstein summation convention. The

tensor γ_{jkl} is antisymmetric both in the first two indices and in its argument. If we search for a plane wave solution of the form $E e^{i(\mathbf{k} \cdot \mathbf{r} - \omega t)}$, we find by substitution

$$D_j = (\epsilon_{jk} + i\gamma_{jk})E_k, \quad (3-2)$$

where we have introduced the second rank antisymmetric tensor

$$\gamma_{jk} = \gamma_{jkl}k_l = -\gamma_{kj} \quad (3-3)$$

and assumed that both ϵ_{ij} and γ_{ij} are macroscopic entities, not depending anymore on \mathbf{r} . Finally we introduce the gyration vector $\boldsymbol{\gamma}$ by

$$\gamma_i = \frac{1}{2}e_{ijk}\gamma_{jk}, \quad (3-4)$$

with $e_{ijk} = \frac{1}{2}(i-j)(j-k)(k-i)$, thus finding

$$\mathbf{D} = \boldsymbol{\epsilon}\mathbf{E} - i\boldsymbol{\gamma} \times \mathbf{E}. \quad (3-5)$$

Equation (3-5) gives combined with Maxwell's equation

$$\mathbf{D} = n^2(\mathbf{E} - \mathbf{s}(\mathbf{s} \cdot \mathbf{E})), \quad (3-6)$$

where $\mathbf{k} = ks$ and $|\mathbf{s}| = 1$, a set of equations for the electric field, called the Fresnel equations:

$$\{\boldsymbol{\epsilon} - n^2\{\mathbf{1} + \mathbf{s}\mathbf{s}\}\} \cdot \mathbf{E} - i\boldsymbol{\gamma} \times \mathbf{E} = 0. \quad (3-7)$$

The equation for the refractive index n follows by putting the determinant of (3-7) to zero. If we choose a coordinate system where ϵ_{ij} is diagonal, we can write

$$(n^2 - n'_{02})(n^2 - n'_0{}^2) = G^2, \quad (3-8)$$

where

$$G^2 = \frac{(\boldsymbol{\epsilon}\boldsymbol{\gamma}) \cdot \boldsymbol{\gamma} - n^2(\mathbf{s} \times \boldsymbol{\gamma})^2}{(\boldsymbol{\epsilon}\mathbf{s}) \cdot \mathbf{s}}. \quad (3-9)$$

In (3-8), n'_0 and n'_{02} correspond to the two solutions of the Fresnel equation in absence of the gyration effect, while in (3-9), n corresponds to either of these two solutions. At this stage, usually, the approximation $\boldsymbol{\epsilon} = n^2\mathbf{1}$ is made. In other words, the effect of the birefringence on G , which can be considered as a higher order effect, is neglected. This is possible if $|\boldsymbol{\gamma}| \ll |\boldsymbol{\epsilon}|$. The result is the simple

form

$$G^2 = (\mathbf{s} \cdot \boldsymbol{\gamma})^2. \quad (3-10)$$

If we assume that $n'_{02} > n''_{02}$, we find for the solutions of (3-8)

$$n^2 = \frac{1}{2} (n'_{02} + n''_{02} \pm \{(n'_{02} - n''_{02})^2 + 4G^2\}^{1/2}). \quad (3-11)$$

Hence, the elliptical form of the section of the indicatrix is perturbed by G , which in practice is one or two orders of magnitude smaller than the birefringence $\Delta n = (n'_{02} - n''_{02})$, when \mathbf{s} is not too close to the direction of an optic axis. The value of G^2 depends on the direction of the wave normal. In general G can be written as

$$G = g_{ij} s_i s_j, \quad (3-12)$$

where $\gamma_i = -g_{ij} s_j$. The g_{ij} form a second rank real pseudo tensor for which one can use symmetry arguments to predict its form. The transformation under an orthogonal element R goes according to

$$g'_{ij} = \det(R) R_{ik} R_{jl} g_{kl} \quad (3-13)$$

and for all $R \in K$, where K is the point group of the crystal in question, the symmetry condition demands that $g'_{ij} = g_{ij}$. In particular, it follows that \mathbf{g} and therefore $\boldsymbol{\gamma}$ vanish for a crystal with inversion symmetry.¹

Using equations (3-6) and (3-7), one can find the solutions of the waves. These can be written as a superposition of two elliptically polarised waves, corresponding to the two refractive indices given by (3-11). The ellipticities of both waves are the same, although the sense of rotation is mutually opposite.

3.3. HAUP polarimeter

We will give a description of the principles involved in the HAUP-measurement, which differs slightly from the one, Kobayashi *et al.*^{4,5} have presented. We will only consider the case for which measurements are performed at a fixed wavelength of the light used. This in contrast to an early description by Kobayashi,³ where measurements were done as function of wavelength. The drawback of the latter method is that the dispersion of the optical activity and the birefringence can be so

large, that it diminishes the valuability of the results.

Assume that a parallel beam of monochromatic light traverses a plane parallel specimen of a certain crystal (see Fig. 3.1).

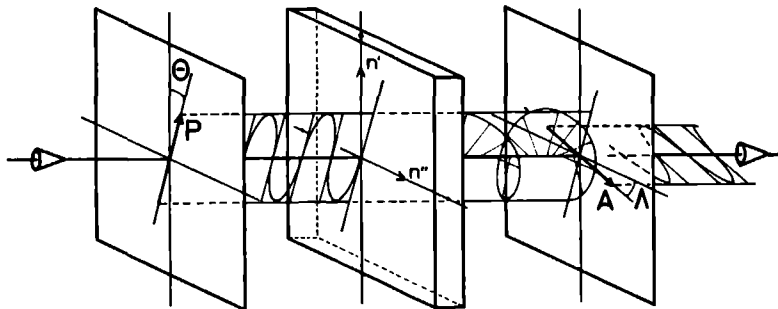


Figure 3.1. Schematic drawing of the principles of the measurement. The angles and vectors indicated are referred to in the text.

The wavelength of the light is λ and the thickness of the specimen is d . The relevant optical properties of the specimen are given by the birefringence (Δn) and the gyration coefficient (G) (both as observed for the specific direction involved). The effective refractive index (\bar{n}) is defined as $\bar{n} = (n'n'')^{1/2}$, where n' and n'' are the highest and lowest refractive indices respectively, for that direction.

On passing the specimen the polarisation of the light beam will be changed due to both the birefringence and the optical activity. The change in polarisation of the light leaving the crystal will therefore have two contributions. The difference due to the birefringence is determined by the phase difference for the two rays in the crystal, which is given by

$$\Delta_{\Delta n} = \frac{2\pi d}{\lambda} \Delta n. \quad (3-14)$$

The difference due to the optical activity is given by the phase difference

$$\Delta_G = \frac{2\pi d}{\lambda n} G. \quad (3-15)$$

Now suppose that the polarisation of the incoming light as determined by a polariser is given by the vector \mathbf{P} , while the detected light is analysed by a second polariser, specified by the vector \mathbf{A} . Furthermore we assume that the (experimentally variable) angle between \mathbf{P} and one of the principal axes of the relevant section of the indicatrix is given by Θ , while the angle between \mathbf{A} and the other principle axis is Λ . The vector \mathbf{P} will be rotated due to both Δn and G . This complicated combined rotation is easily represented in terms of a description of the state of polarisation on the so-called Poincaré-sphere.⁸ This representation allows also for a simple calculation of the intensity of the light emerging from the specimen, as analysed by \mathbf{A} . As the exact knowledge of both Λ and Θ is essential, an introduction of some corrections due to experimental errors is necessary. First of all, the value of Θ (and Λ) is very difficult to determine exactly. This problem, however, can be overcome by introducing an alternative angle defined by $\Theta' = \Theta_0 + \Theta$, where Θ_0 can be determined very accurately. Secondly, the non-perpendicularity of the light beam with respect to the sample will introduce an additional rotation of the polarisation, resulting in an error $\delta\Lambda$. Finally, the ellipticities of the polariser and analyser will be specified as p and a respectively. In first instance, we will only introduce p and a ; the errors in Θ and Λ will be added later. The Poincaré-sphere is drawn in Fig. 3.2.

In this figure, the principal directions of the elliptic section of the indicatrix are along x and $-x$, while the (x,y) -plane represents linearly polarised light. The effects of p and a are to add an ellipticity to the vectors $\mathbf{P}(\Theta)$ and $\mathbf{A}(\Lambda)$ (which represent linear polarisations) respectively. The birefringence (Δn) and the gyration (G) introduce a rotation of $\mathbf{P}(\Theta, p)$ around the axis BB' , which makes an angle 2β with the x -axis, where

$$\tan 2\beta = \frac{\Delta_G}{\Delta_{\Delta n}} = \frac{G}{\Delta n n} = 2k. \quad (3-16)$$

The rotation angle Δ is given by

$$\Delta^2 = \Delta_{\Delta n}^2 + \Delta_G^2 = \frac{2\pi d}{\lambda} \{(\Delta n)^2 + \left(\frac{G}{n}\right)^2\}. \quad (3-17)$$

The resulting vector $\mathbf{P}'(\Theta, p, \Delta, \beta)$ represents the state of polarisation of the light emerging from the specimen. The corresponding intensity as passed by the analyser,

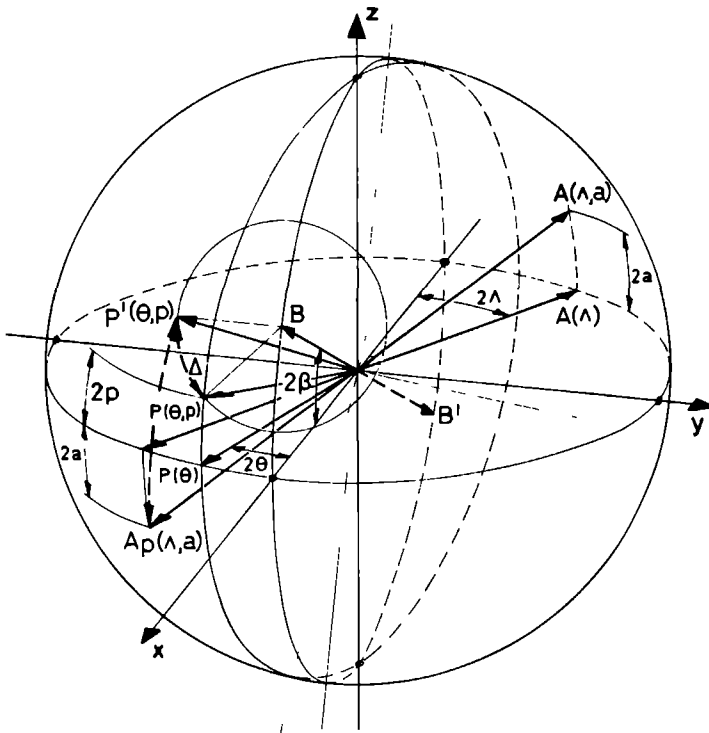


Figure 3.2. Poincaré-sphere representation of the different states of polarisation relevant for the experiment. The different symbols are referred to in the text.

is now given by $I = I_0 \cos^2(\frac{1}{2} \text{segm}(\mathbf{P}', \mathbf{A}))$, where I_0 is the intensity of the incoming light and $\text{segm}(\mathbf{P}', \mathbf{A})$ is the length of the short arc on the sphere (with unit radius), joining $\mathbf{P}'(\Theta, p, \Delta, \beta)$ and $\mathbf{A}(\Lambda, a)$, or equivalently by $(I = I_0 \sin^2(\frac{1}{2}(\text{segm}(\mathbf{P}', \mathbf{A}_p)))$, where $\mathbf{A}_p(\Lambda, a)$ indicates the vector $\mathbf{A}(\Lambda + \pi, -a)$. Since the actual values of Θ and Λ are very small (typical values are maximal 0.5°), one can approximate the segm-function by $\text{segm}(\mathbf{P}', \mathbf{A}_p) \approx |\mathbf{P}' - \mathbf{A}_p|$. For the same reason, this distance can be calculated using plane trigonometry, assuming the relevant area of the sphere to be flat. The intensity can thus be written as ($2k = \tan 2\beta \approx 2\beta$)

$$\begin{aligned}
I(\Theta, \Lambda, p, a) = I_0\{(\Theta + \Lambda)^2 - \Theta\Lambda(2 + 2\cos\Delta) + \\
\Theta\{2(k + a)\sin\Delta\} - \Lambda\{2(k - p)\sin\Delta\} + \\
\{(p + a)^2 + 4\{k^2 - k(p - a) - pa\}\sin(\Delta/2)\}\} \quad (3-18)
\end{aligned}$$

The experimental error in Θ and Λ can be eliminated by measuring I as a function of Θ' (the experimental value) with the analyser always crossed. This measurement can be performed very accurately. For this condition, the intensity becomes a parabola as a function of Θ' . We define the angle Θ_0 as the value of Θ , for which the intensity in this crossed configuration manifests a minimum, which is experimentally easily found. The value of Θ_0 thus becomes $\Theta_0 = -\frac{1}{2}(a + p)\cotg(\Delta/2)$. The experimental value for the polariser angle Θ' is given by $\Theta' = \Theta - \Theta_0$. When we also introduce the correction $\delta\Lambda$ in the analyser position by putting $\Lambda' = \Lambda - \Theta_0 - \delta\Lambda$ in the equation for the intensity, we find

$$\Theta_0 = -\frac{1}{2}(a + p)\cotg(\Delta/2) - \frac{1}{2}\delta\Lambda \quad (3-19)$$

and the intensity becomes

$$I = I_0\{A_0 + \{\chi - \cos(\Delta/2)(\Theta - \Lambda)\}^2 + \{\sin^2(\Delta/2)(\Theta + \Lambda)\}^2\}. \quad (3-20)$$

In this equation we have introduced a background term A_0 , which contains scattered light and the variable χ :

$$\chi = \{(\gamma - 2k)\sin(\Delta/2) + \delta\Lambda\cos(\Delta/2)\}, \quad (3-21)$$

where $\gamma = p - a$. Before describing the procedure to extract the values of Δn and G from the experimental data, we will give a brief description of the experimental set-up.

As can be seen in Fig. 3.3, a beam of light from a laser passes a polariser, a specimen, an analyser and is finally detected by a photomultiplier. At several places in the optical path, scattered or stray light is blocked by means of pinholes and diaphragms. A reference detector is used in order to compensate for fluctuations in the laser output power. The precision of the position of both polariser and analyser is very important; therefore, both are mounted inside the cryostats vacuum tank, thus eliminating windows between them. The polarisers are rotated by means of stepping motors resulting in a resolution of approximately 0.001° . These motors are driven by a computer, which also controls temperature settings and collects data

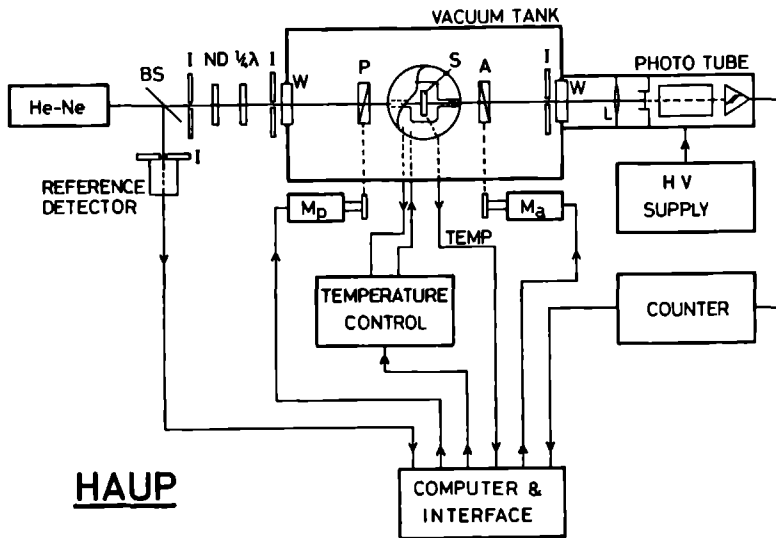


Figure 3.3. Experimental set-up for HAUP BS=beam splitter, I=iris diaphragm, ND=neutral density filter, P=polariser, A=analyser, M_a , M_p =stepping motor, W=window, L=lens, S=sample.

from both detectors. Temperatures below room temperature are achieved by cooling with a flow of liquid nitrogen or helium. Temperature stabilisation is obtained with a heater mounted in a copper block serving as a heat buffer. Above room temperature this block is only heated. The sample is placed within a radiation shield on top of the copper block, with two pin holes for the light beam to pass. A stressless mount of the crystal is very important in order to avoid strain induced gyration effects.

The measurement proceeds as follows. For each temperature, two measurements are performed. In the first one, the intensity is measured as a function of the polariser position (Θ), with the analyser crossed. The result is fitted to a parabola and the minimum of the resulting function corresponds to the angle Θ_0 . Then a second measurement is performed with Θ_0 as the zero position for both the polariser and the analyser. In this second (two-dimensional) scan, the intensity

is measured as a function of Λ for several values of Θ . The results of this 2D-scan are fitted to equation (3-20), giving values for I_0 , A_0 , χ and $\cos(\Delta/2)$. From the latter two, Δn and G must be extracted. Therefore some assumptions are necessary. First of all, $\delta\Lambda$ and γ are assumed to be temperature independent, which is certainly reasonable for γ . The latter value, however, can only be extracted when k is known for at least one temperature, e.g. in a phase where the gyration is known to be zero (cf. (3-21)). Furthermore, Δ and the sign of $\delta\Delta/\delta T$ have to be known for one temperature, because the fit only provides values of $|\Delta/2|$ modulo 2π . For this purpose the birefringence (Δn) can be used when $G \ll \Delta n$. Thus Δ is determined for all temperatures. The value of $\delta\Lambda$ is found by averaging all values of χ with $|\sin(\Delta/2)|$ small compared to $|\cos(\Delta/2)|$. So finally k and therefore G are found as a function of temperature. The birefringence $\Delta n(T)$ is found from $\Delta(T)$.

In practice, the values found for γ and $\delta\Lambda$ are (as k is) of the order of 10^{-3} and therefore not negligible. This means that the method is not suited for determining the optical activity of a sample for one single temperature (or other parameter), unless the value of k happens to be big compared to γ . This drawback makes HAUP less Universal. On the other hand, restrictions concerning sample orientation and polarisation quality, must hold for any other type of polarimeter.

References

1. Nye, *Physical Properties of Crystals* (Oxford University Press, 1985), chapter XIV.
2. H. Kelker and R. Hatz, *Handbook of Liquid Crystals* (Weinheim-Deerfield: Verlag Chemie, 1980), chapter 7.
3. J. Kobayashi, T. Takahashi, T. Hosokawa and Y. Uesu, *J. Appl. Phys.* **49**, 809 (1978).
4. J. Kobayashi, Y. Uesu, *J. Appl. Cryst.* **16**, 204 (1983).
5. J. Kobayashi, H. Kumomi and K. Saito, *J. Appl. Cryst.* **19**, 377 (1986).
6. See for example A. Sommerfeld, *Vorlesungen über Physik IV, Optik*.
7. M. Born, *Optik* (Springer, Berlin, 1985).
8. G.N. Ramachandran and S. Ramaseshan, *J. Opt. Soc. Am.* **42**, 49 (1952).

3.4. Optical activity in the incommensurate structure Rb_2ZnBr_4

H. Meekes

Research Institute for Materials

A. Janner

Institute of Theoretical Physics

University of Nijmegen, Toernooiveld,

6525 ED Nijmegen, The Netherlands

Abstract

The optical activity in Rb_2ZnCl_4 crystals has been measured along three directions in a temperature interval from above 400 K down to 50 K. In the incommensurate phase already a non-vanishing element of the gyration tensor has been observed, despite the fact that the average crystal structure has inversion symmetry. In order to explain this, phenomenological spatial dependent dielectric and gyration tensors, being invariant with respect to the superspace group of Rb_2ZnBr_4 , have been considered. The selection rules imposed by symmetry, when compared with the experimental results, give a first indication on which long-wavelength Fourier components of these tensors are eventually responsible for the optical activity observed. A generalisation of our considerations to other incommensurate structures is discussed.

3.4.1. Introduction

Rb_2ZnBr_4 is a member of the large family of A_2BX_4 -dielectrics, which show a variety of phase transitions between different modulated phases. Many of these dielectrics -including Rb_2ZnBr_4 - have an incommensurately modulated phase in a certain temperature range.¹ For an understanding of the mechanisms responsible for the phase transitions in these materials, a knowledge of the symmetry properties of the different phases is of great importance. Especially in the incommensurate phase, where a normal space group description is not possible, a study of the symmetry properties is interesting as one can test the validity of the so-called superspace group description.² These superspace groups have already been very useful for an understanding of a number of physical properties both in incommensurate and commensurate phases.³

The determination of optical activity -a third-rank-tensorial property of crystals- is a powerful tool to find certain symmetry properties of crystals. By this means one tests for example the presence of an inversion center or a mirror on the scale of the wave length of the light used. Although the precise measurement of optical activity has been very difficult for directions other than the optical axes of the crystal, the introduction by Kobayashi and Uesu of a new type of polarimeter (HAUP) made the measurement much more reliable and versatile.⁴ We have measured the optical activity of Rb_2ZnBr_4 in three independent directions, in order to be able to compare the superspace description with another more conventional approach, which makes use of the symmetry of an average structure in the incommensurate phase, perturbed by the modulation.

Our specific choice for Rb_2ZnBr_4 was made for several reasons. First of all the symmetry of the incommensurate phase has not been determined very conclusively in spite of great effort.⁵ Secondly, this crystal has several low-temperature phases of which the structure is even more unclear^{6,7,8} and thirdly no measurement of optical activity of this compound has been reported up to now.

This paper is organised as follows. In section 3.4.2 we will give a description of the sequence of phases in Rb_2ZnBr_4 and a prediction for the optical activity, with special attention for the incommensurate phase. Section 3.4.3 will treat the symmetry properties of both the dielectric and the gyration tensor in the superspace approach. The next section deals with the experimental details including the evaluation procedure used for the results. A discussion of these results is given in section 3.4.5 and finally we will give a conclusion.

3.4.2. Optical activity in Rb_2ZnBr_4

The setting we use will be the one chosen by Hogervorst in his comparative study of the modulated structures of the A_2BX_4 -family,¹ for which at room temperature, $a = 13.33 \text{ \AA}$, $b = 7.66 \text{ \AA}$ and $c = 9.71 \text{ \AA}$, with basic space group $Pcmn$. Rb_2ZnBr_4 has a paraelectric phase between the melting point (753 K) and the incommensurate phase transition (347 K). The incommensurate modulation consists mainly of rotations of the ZnBr_4^{2-} -tetrahedra, combined with small shifts of all ions along the \mathbf{b} -axis,⁵ the modulation wave vector being along \mathbf{c}^* : $\mathbf{q} = \gamma\mathbf{c}^*$ ($\gamma \approx 0.293$).⁹ At $T_c = 190 \text{ K}$, the wave vector jumps from its rather constant value in the incommensurate phase to the value $\gamma = \frac{1}{3}$, resulting in a commensurate three fold superstructure (lock-in phase) between T_c and $T_3 = 112 \text{ K}$ which is ferroelectric (F -phase). At T_3 a new phase transition (to phase IV) appears as was concluded from measurements of the dielectric constant.⁶ The symmetry in phase IV, however, does not differ from the lock-in (phase III) symmetry. The structure of the lowest temperature phases (Phase V between 77 K and 50 K and VI below 50 K) is not very clear. According to Ueda *et al.*⁸ the rational value of γ stays $\frac{1}{3}$, only some symmetry elements being lost.

For an overview of the expected symmetry groups and some measured properties see Table 3-I.

TABLE 3-I

phase	VI	V	IV	III	II	I
temp (K)	<50	<77	<112	<190	<347	<753
γ	$\frac{1}{3}$	$\frac{1}{3}$	$\frac{1}{3}$	$\frac{1}{3}$	inc.	0 ($Z=4$)
space group	$Pc11(?)$	$Pc11(?)$	$Pc2_1n$	$Pc2_1n$	$Pcmn(00\gamma)(ss\bar{1})$	$Pcmn$
ferroel.	b	b	b	b	-	-
antiferroel.	-	-	a	-	-	-

Table 3-I. The different phases of Rb_2ZnCl_4 . Given are the phase transition temperatures,⁵ the modulation wave vector ($\mathbf{q} = \gamma\mathbf{c}^*$), the space group symmetry and reported ferroelectric and antiferroelectric properties.

With the use of the point group symmetry of the structure in the different commensurate phases one can easily predict which elements of the gyration tensor (g_{ij}) are expected to be zero (see for example Nyc¹⁰ and further on in this section). The results are summarised in Table 3-II.

TABLE 3-II

phase	VI	V	IV	III	I
gyration tensor	$\begin{pmatrix} 0 & g_{12} & g_{13} \\ g_{12} & 0 & 0 \\ g_{13} & 0 & 0 \end{pmatrix}$	$\begin{pmatrix} 0 & g_{12} & g_{13} \\ g_{12} & 0 & 0 \\ g_{13} & 0 & 0 \end{pmatrix}$	$\begin{pmatrix} 0 & 0 & g_{13} \\ 0 & 0 & 0 \\ g_{13} & 0 & 0 \end{pmatrix}$	$\begin{pmatrix} 0 & 0 & g_{13} \\ 0 & 0 & 0 \\ g_{13} & 0 & 0 \end{pmatrix}$	$\begin{pmatrix} 0 & 0 & 0 \\ 0 & 0 & 0 \\ 0 & 0 & 0 \end{pmatrix}$

Table 3-II. The various forms of the gyration tensor in the commensurate phases of Rb_2ZnBr_4 allowed by symmetry.

Here we find that for temperatures below 77 K both g_{12} and g_{13} need not to be equal to zero, if we assume a m_x point symmetry, while between 77 K and 347 K this holds only for g_{13} . In the high temperature paraelectric phase the gyration tensor is zero because the point group is centro-symmetric.

In the incommensurate phase, the normal space group description is not adequate for the analysis of the gyration tensor. Instead of the normal three-dimensional space group one can, however, make use of higher dimensional space groups, with the aid of which the lattice translational symmetry of the crystal can be restored.² It is still not definitely settled which superspace group describes the symmetry of the incommensurate phase of Rb_2ZnBr_4 . Hogervorst⁵ has performed a structure determination on the basis of the (3 + 1)-dimensional space groups $Pcmn(00\gamma)(ss\bar{1})$, $Pc2_1n(00\gamma)(s\bar{1}\bar{1})$ and $P2_12_12_1(00\gamma)(\bar{1}\bar{1}1)$ and found the best -though doubt still exists- agreement with $Pcmn(00\gamma)(ss\bar{1})$; he claims that the actual structure is commensurate with $\gamma = 5/17$, down to ten degrees above T_c , although usage of the space group corresponding to that superstructure leads to less good results than when using the superspace group. A major difference between $Pcmn(00\gamma)(ss\bar{1})$ and the second best candidate $Pc2_1n(00\gamma)(s\bar{1}\bar{1})$ is that the former is centro-symmetric, while the latter is not. The commensurate superstructure with $\gamma = 5/17$ would have symmetry $Pc2_1n$, which is not centro-symmetric and in fact would give the same

predictions for the gyration tensor as given for phase III in Table 3-II.

A general theory on the symmetry of tensors describing physical properties of structures with a superspace symmetry is not yet available despite the fact that, mathematically speaking, the restrictions imposed by a superspace group on tensor fields are well defined. The problem lies more in the fact that in the physical 3-dimensional space, where the laws of physics are well known, the distinction between microscopic and macroscopic properties is less well defined than in the case of a normal crystal, because in three dimensions, the unit cell of an incommensurate crystal is infinite and the notion macroscopic can not be defined as involving length scales much larger than the elementary cell of the microscopic structure. In the $(3 + d)$ -dimensional space, however, such a distinction is possible as the volume of the higher dimensional unit cell is finite. The problem then arises of an appropriate extension of the physical laws to the higher dimensional space. Such an extension is in principle possible but not at all trivial. Here, the restrictions imposed by the superspace symmetry will be considered without extending the physical laws, but including more Fourier components than the constant one, as is done in the commensurate crystal case. An introductory approach to the problem can be found in Ref. 11. Some specific local tensorial properties, however, have already been examined within the context of superspace symmetry. For example the electric field gradient (EFG) tensor in incommensurate phases has been studied by van Beest and Janner.¹² In the light of this treatment, the experimental data for the Rb EFG-tensors and the Rb NMR-line-shape in both Rb_2ZnBr_4 and Rb_2ZnCl_4 are compatible with $Pcmn(00\gamma)(ss\bar{1})$ as the superspace group symmetry of the incommensurate phase in these compounds.¹³ Hence Rb_2ZnCl_4 would have a centro-symmetric incommensurate phase and consequently no optical activity. The latter conclusion, however, is in flagrant contradiction with the observations by Uesu and Kobayashi¹⁴ and Sanctuary,¹⁵ who found, though their results differ, a clear presence of optical activity in Rb_2ZnCl_4 . This discrepancy does not mean that a superspace description is not appropriate but it does show that care must be taken when considering the symmetry of different physical properties. In fact the essential difference between NMR (EFG) and optical activity is the microscopic respectively macroscopic nature of the phenomena. The NMR measurements mentioned above were performed on Rb-sites, and they do not (or much less sensitively) probe the symmetry of the Zn and Br or Cl-sites. In other words, the superspace group symmetry element $m_y(s)$ can be present for the Rb-atoms but absent (or nearly so) for the other atoms. Optical activity on the other hand gives information regarding the symmetry on a

much larger scale, of the order of the wave length of the light used. Therefore it probes to a good approximation the full symmetry of the crystal, though, at a semi-macroscopic scale. Care should be taken, however, in using the macroscopic limit because for optical activity the wave length of the light can essentially not be considered as infinite compared to the cell parameters as the phenomenon is understood to be observable only for finite wave length and, as already said, the cell parameters are themselves not all finite.¹⁶

Instead of the superspace description, some authors use the approach which was introduced by Golovko and Levanyuk¹⁷ in the case of $(\text{NH}_4)_2\text{BeF}_4$. They describe the dielectric function as a local property of the crystal, deviating from that determined by the average symmetry. Fousek and Kroupa¹⁸ studied the particular case of Rb_2ZnCl_4 in this approach. The average symmetry is in the case of Rb_2ZnBr_4 the point group $m_x 2_y m_z$.

At this point it is worthwhile to mention that the concept of local symmetry often provides not the most exhaustive description. For example, in the NMR measurements, by adopting the same principle of a local crystal field symmetry, a mirror operation m_y would not be involved, even not for Rb alone. So the local symmetry is not wrong but does not fully take into account symmetry elements which possibly imply additional selection rules and is furthermore not always a well-defined concept. This is particularly the case when in a rational approximation, leading to a superstructure, the point group depends on the approximation adopted in the size of the unit cell.¹⁹ Therefore, we think that it is advisable to take seriously into account the structural restrictions imposed on a microscopic scale by the superspace group in a way appropriate to the physical phenomenon considered. The present treatment of the dielectric and gyration tensor can serve as an illustration of how that can be done. Eventually, the correctness of this approach will have to be found in a comparison between experiment and theory.

3.4.3. Optical symmetry properties in the incommensurate phase

3.4.3.1. General

Our treatment of the symmetry properties of the dielectric tensor in an incommensurate phase is based on the superspace characterisation of such a phase. We will specialise to the superspace group symmetry of Rb_2ZnBr_4 and discuss the generalisation to other A_2BX_4 -members with the same superspace group ($Pcmn(00\gamma)(ssI)$).¹ We will describe the optical properties of the crystal in terms of Fourier components of the tensor in question, which are relevant for the wave propagation of light and include the restrictions imposed by the superspace symmetry.

The basic equation is given by

$$\mathbf{D}(\mathbf{r},t) = \boldsymbol{\epsilon}(\mathbf{r})\mathbf{E}(\mathbf{r},t), \quad (3-22)$$

where we have taken a local dependence of the displacement field \mathbf{D} on the electric field \mathbf{E} . We implicitly have assumed that we are far from resonances, i.e., the problem can be treated statically, with a time-independent dielectric tensor. This tensor $\boldsymbol{\epsilon}(\mathbf{r})$ must have the symmetry of the crystal and therefore (3-22) can be written as

$$\mathbf{D}(\mathbf{k}) = \sum_{\mathbf{h} \in M^*} \boldsymbol{\epsilon}(\mathbf{h})\mathbf{E}(\mathbf{k}-\mathbf{h}) \quad (3-23)$$

where M^* is the set of Fourier wave vectors occurring in the crystal structure. This implies in the present case that M^* is a Z -module of rank 4, which is freely generated by \mathbf{a}^* , \mathbf{b}^* , \mathbf{c}^* (spanning the reciprocal lattice Λ^* of the basic structure) and $\mathbf{q} = \gamma\mathbf{c}^*$ (the modulation wave vector). Note that all these vectors are defined in a 3-dimensional space so that up to now, no embedding in a 4-dimensional space is involved. In the description of light propagation in normal crystals, one realises that the wave vectors for visible light are very small compared to any non-zero reciprocal lattice vector, so (3-23) can very well be approximated by

$$\mathbf{D}(\mathbf{k}) = \epsilon(0)\mathbf{E}(\mathbf{k}), \quad (3-24)$$

where $\epsilon(0)$ can be viewed as a space averaged dielectric tensor. This equation leads together with Maxwell's equations ($\mathbf{n} = \mathbf{k}c/\omega$; ω is the frequency of the light)

$$\mathbf{D}(\mathbf{k}) = n^2\mathbf{E}(\mathbf{k}) - \mathbf{n}(\mathbf{n}\cdot\mathbf{E}(\mathbf{k})), \quad (3-25)$$

to the Fresnel equations, whose solutions specify the electric fields in the crystal and the refractive indices (n) in terms of the dielectric tensor elements $\epsilon_{ij}(0)$. In the case of an incommensurate crystal however, periodicities are present with a considerably longer wavelength than in ordinary crystals. In principle at least, M^* includes, because of the incommensurability between \mathbf{q} and Λ^* , arbitrarily small Fourier wave vectors. Hence, one can expect that in these crystals also non-zero reciprocal Z -module vectors contribute substantially to the propagation of visible light. The description of the dielectric tensor as a microscopic entity, influenced by the relatively long waves, in a Landau-like approach has been adopted by Golovko and Levanyuk¹⁷ for $(\text{NH}_4)_2\text{BeF}_4$ and later by Fousek and Kroupa¹⁸ for Rb_2ZnCl_4 . It is therefore important to compare our results with those of the latter two authors. We will first solve the Fresnel equations taking into account additional Fourier elements of the dielectric tensor and afterwards also discuss the relations imposed by symmetry on the gyration tensor.

3.4.3.2. The dielectric tensor

The wave vectors in the rank-four Z -module are specified by four integral indices (h, k, l, m) , according to $\mathbf{h} = h\mathbf{a}^* + k\mathbf{b}^* + l\mathbf{c}^* + m\mathbf{q}$. In our case we take $\mathbf{q} = \gamma\mathbf{c}^*$ with γ irrational. It is then easy to see that the vectors $(0, 0, l, m)$ for suitable choice of l and m are arbitrarily small. However, the larger the indices l or m , the smaller the structural information carried by the corresponding wave vector and hence, the smaller its corresponding tensor $\epsilon(\mathbf{h})$ is expected to be. Therefore, we search for the smallest l and m indices, leading to wave vectors which are small compared to the dimensions of (say) the first Brillouin zone of the basic structure. An elegant method to find l and m with these requirements is found in the continued fractions expansion of γ . This approximation provides a unique series of fractions which converges to the irrational value of γ . For each step in the

expansion, say $\frac{l}{m}$ (l and m integer), the next step increases the value of both l and m . The reciprocal lattice vector $(0,0,l,\bar{m})$ therefore decreases in length, but with each step, normally speaking, also decreases in structural importance as is typically observed in morphological and X-ray diffraction investigations. We assume that such a decreasing contribution of Fourier components with higher indices is also met in the optical properties of modulated crystals. For $\gamma = 0.293\dots$, the resulting vectors are in order of increasing length and descending importance $(0,0,1,\bar{3})$, $(0,0,2,\bar{7})$, $(0,0,5,\bar{17})$, $(0,0,12,\bar{41})$, \dots . If we make a list of these vectors (including their harmonics) and determine their length, we find for the first three with the lowest indices (we use $|c| = 9.71 \text{ \AA}$)

\mathbf{h}	$\frac{2\pi}{ \mathbf{h} } (\text{\AA})$	
$(0,0,1,\bar{3})$	80.2	(3-26)
$(0,0,2,\bar{6})$	40.1	
$(0,0,2,\bar{7})$	190.2	

As long as we are in the sinusoidal regime of the modulation, i.e. not too far below the incommensurate phase transition, the structural importance of the higher harmonics can be neglected.

The next step will be to determine the form of the tensor $\epsilon(\mathbf{h})$ allowed by the superspace symmetry group $G_s = (Pcmn(00\gamma)(ss\bar{1}))$ in our case). A general element g_s of G_s can be written as $\{R, R_I | \mathbf{t}_s\}$, with R the 3-dimensional orthogonal transformation, R_I the corresponding internal element and \mathbf{t}_s a superspace translation.² The elements \mathbf{h} of M^* can be embedded as reciprocal lattice vectors \mathbf{h}_s in the 4-dimensional lattice Λ_4^* , with correspondingly same integral components (h, k, l, m) . The tensorial Fourier components are also embedded according to $\epsilon(\mathbf{h}_s) = \epsilon(\mathbf{h})$ and the invariance with respect to g_s is given by

$$\epsilon_{ij}(\mathbf{h}) = R_{ik} R_{jl} \epsilon_{kl}(\mathbf{R}\mathbf{h}) e^{i(\mathbf{R}_s \mathbf{h}_s) \cdot \mathbf{t}_s}, \quad (3-27)$$

where the Einstein summation convention is used. If we make a list of the scalar

product $(\mathbf{R}_s \mathbf{h}_s) \cdot \mathbf{t}_s$ for the elements of G_s which are relevant, we find

g_s	$(\mathbf{R}_1 \mathbf{h}_s) \cdot \mathbf{t}_s$
$\{c_x, 1 \frac{1}{2} 0 \frac{1}{2} \frac{1}{2}\}$	$\pi(-h+l+m)$
$\{m_y, 1 0 \frac{1}{2} 0 \frac{1}{2}\}$	$\pi(-k+m)$
$\{n_z, \bar{1} \frac{1}{2} \frac{1}{2} \frac{1}{2} 0\}$	$\pi(h+k-l)$
$\{\bar{1}, \bar{1} 0000\}$	0
$\{2_x, \bar{1} \frac{1}{2} 0 \frac{1}{2} \frac{1}{2}\}$	$\pi(h-l-m)$
$\{2_y, \bar{1} 0 \frac{1}{2} 0 \frac{1}{2}\}$	$\pi(k-m)$
$\{2_z, 1 \frac{1}{2} \frac{1}{2} \frac{1}{2} 0\}$	$\pi(-h-k+l)$
$\{1, 1 0000\}$	0

For $\mathbf{h} = 0$, and hence $\mathbf{h}_s = 0$ equation (3-27) reduces to the symmetry condition for ordinary (3D-) macroscopic tensors, thus bringing $\epsilon(0)$ to a diagonal form ($\epsilon_{ij} = \epsilon_i \delta_{ij}$) in our (orthorhombic) coordinate system.

For $\mathbf{h} \neq 0$, we find different results. One can specify l and m by their parity condition, thus finding (ϵ is diagonal ($o = \text{odd}$ and $e = \text{even}$))

$l, m=0, 0$	o, o	e, e	o, e	e, o
$\begin{pmatrix} \epsilon_1 & 0 & 0 \\ 0 & \epsilon_2 & 0 \\ 0 & 0 & \epsilon_3 \end{pmatrix}$	$\begin{pmatrix} 0 & 0 & 0 \\ 0 & 0 & \epsilon_4 \\ 0 & \epsilon_4 & 0 \end{pmatrix}$	$\begin{pmatrix} \epsilon_6 & 0 & 0 \\ 0 & \epsilon_7 & 0 \\ 0 & 0 & \epsilon_8 \end{pmatrix}$	$\begin{pmatrix} 0 & 0 & \epsilon_9 \\ 0 & 0 & 0 \\ \epsilon_9 & 0 & 0 \end{pmatrix}$	$\begin{pmatrix} 0 & \epsilon_5 & 0 \\ \epsilon_5 & 0 & 0 \\ 0 & 0 & 0 \end{pmatrix}$

(3-28)

Here we have introduced a short notation for the different tensor components. Note that $\epsilon(\mathbf{h}) = \epsilon(-\mathbf{h})$ due to $\epsilon(\mathbf{r})$ being real in a lossless medium and because of the total inversion symmetry in G_s .

If we return to our basic equations (3-23), we could write these equations, restricting to (say) the first three wave vectors given in (3-26). In order to limit the calculations, we will make the following approximation. Equations (3-23) will be solved in a two and a three Fourier wave approximation, where one wave is given by $\mathbf{h} = 0$ and the other by one or two of the wave vectors in (3-26). In the two-wave approximation, equations (3-23) become (fields with wave vector $\mathbf{k} \pm 2\mathbf{h}$ are neglected)

$$\begin{cases} \mathbf{D}(\mathbf{k} - \mathbf{n}) = \boldsymbol{\epsilon}\mathbf{E}(\mathbf{k} - \mathbf{n}) + \boldsymbol{\epsilon}(-\mathbf{n})\mathbf{E}(\mathbf{k}) \\ \mathbf{D}(\mathbf{k}) = \boldsymbol{\epsilon}(\mathbf{h})\mathbf{E}(\mathbf{k} - \mathbf{h}) + \boldsymbol{\epsilon}\mathbf{E}(\mathbf{k}) + \boldsymbol{\epsilon}(-\mathbf{h})\mathbf{E}(\mathbf{k} + \mathbf{h}) \\ \mathbf{D}(\mathbf{k} + \mathbf{h}) = \boldsymbol{\epsilon}(\mathbf{h})\mathbf{E}(\mathbf{k}) + \boldsymbol{\epsilon}\mathbf{E}(\mathbf{k} + \mathbf{h}). \end{cases} \quad (3-29)$$

re we have written $\boldsymbol{\epsilon}(0) = \boldsymbol{\epsilon}$. Equations (3-29) give combined with Maxwell's tions (3-25) a set of equations for the Fourier components of the electric field, \mathbf{h} in block-matrix form on the basis $\{\mathbf{E}(\mathbf{k} - \mathbf{h}), \mathbf{E}(\mathbf{k}), \mathbf{E}(\mathbf{k} + \mathbf{h})\}$ can be written as

$$\begin{bmatrix} \boldsymbol{\epsilon} - \mathbf{F}(\mathbf{k}-\mathbf{h}) & \boldsymbol{\epsilon}(\mathbf{h}) & 0 \\ \boldsymbol{\epsilon}(\mathbf{h}) & \boldsymbol{\epsilon} - \mathbf{F}(\mathbf{k}) & \boldsymbol{\epsilon}(\mathbf{h}) \\ 0 & \boldsymbol{\epsilon}(\mathbf{h}) & \boldsymbol{\epsilon} - \mathbf{F}(\mathbf{k}+\mathbf{h}) \end{bmatrix} \begin{bmatrix} \mathbf{E}(\mathbf{k}-\mathbf{h}) \\ \mathbf{E}(\mathbf{k}) \\ \mathbf{E}(\mathbf{k}+\mathbf{h}) \end{bmatrix} = 0 \quad (3-30)$$

e

$$\mathbf{F}(\mathbf{k}) = \begin{bmatrix} n_2^2 + n_3^2 & -n_1n_2 & -n_1n_3 \\ -n_1n_2 & n_3^2 + n_1^2 & -n_2n_3 \\ -n_1n_3 & -n_2n_3 & n_1^2 + n_2^2 \end{bmatrix} \quad (3-31)$$

$\mathbf{F}(\mathbf{k}\pm\mathbf{h})$ is the matrix $\mathbf{F}(\mathbf{k})$, with \mathbf{n} replaced by $\mathbf{n}\pm\mathbf{m}$. In this matrix, the $n_1, 1,2,3$) are the refractive indices for fields with wave vector \mathbf{k} ($k = n\omega/c$). As other frequencies are present in the crystal, we interpret the fields with wave or $\mathbf{k} \pm \mathbf{h}$ as $\mathbf{k} \pm \mathbf{h} = (\mathbf{n} \pm \mathbf{m})\omega/c$. Note that the corresponding excitation can r be a solution of the normal Fresnel equations since $m^2 \gg \epsilon_{ij}$. For 630 nm-light, $n = 1.65$; the corresponding value of m is $m \approx 130$. The role of m erely that of an alternative refractive index, which specifies the coupling of a mode with wave vector \mathbf{k} to the long wavelength structural contributions to the :ctric constant. In other words, the normal modes for light propagation will : refractive indices which are predominantly determined by the Fresnel equations ie basic structure. There exists, however, a special case, for which $2\pi/|\mathbf{h}|$ is of order of the wavelength of the light. That regime has been treated in a oscopic approach by van Beest,²⁰ but will be disregarded here.

We first solved such a set of equations in a three Fourier-wave approximation, iding \mathbf{k} , $\mathbf{k} \pm \mathbf{h}$ and $\mathbf{k} \pm 2\mathbf{h}$, where $\mathbf{h} = (0,0,1,\beta)$; this in order to be able to pare the results of our approach with the ones obtained by Fousek and upa.¹⁸ In their approach, these authors found a diagonal contribution to $\boldsymbol{\epsilon}$, isting of a position independent part and a part which is modulated with wave

vector $6\mathbf{q}$, where \mathbf{q} is the modulation wave vector. Furthermore they found a $3\mathbf{q}$ -modulated contribution to ϵ_{23} . In fact, we find comparable results for $\epsilon(2\mathbf{h})$ and $\epsilon(\mathbf{h})$ respectively. The difference between their approach and ours is that they use the symmetry of the (approximate) commensurate phase ($\mathbf{q} = \frac{1}{3}\mathbf{c}^*$) and introduce a deviation via a space dependent amplitude and phase of the modulation, where as in our approach, we use the full symmetry of the incommensurate phase, albeit that we also neglect higher order Fourier components. The results for the electric fields in our approximation are comparable to those of Fousek and Kroupa. Due to their commensurate approximation being limited to the vector $(0,0,\frac{1}{3})$ and its first harmonic, Fousek and Kroupa have also a different interpretation of the wave vector of the modulation, which is superimposed on the fields. In their approach the corresponding wavelengths are $|\mathbf{c}| = 9.7\text{\AA}$ and $|\mathbf{c}|/2$. In our approach, the relevant wavelengths that one gets from the Z -module elements are much larger (cf. (3-26)). Obviously, the coupling between the light and the structural deformations will be larger when the wavelengths of both approach each other. Taking this into account and the results of the continued fractions expansion (3-26), we conclude that in the sinusoidal regime of the modulation, the first two Fourier components of structural importance are $\mathbf{h}_1 = (0,0,1,\bar{3})$ and $\mathbf{h}_2 = (0,0,2,\bar{7})$ and the contribution of $2\mathbf{h}$, can be neglected. Therefore we solved the Fresnel equations in the same way, now using \mathbf{h}_1 and \mathbf{h}_2 and found for the three principal directions of propagation ($m_3 = |\mathbf{h}_1|$ and $p_3 = |\mathbf{h}_2|$)

$$\mathbf{n} = (n_1, 0, 0)$$

$$\left\{ \begin{array}{l} E_1(\mathbf{r}) = \left[\frac{2i\epsilon_4 n_1 m_3 \sin(\mathbf{h}_1 \cdot \mathbf{r})}{(n_1^2 - \epsilon_3)(m_3^2 - \epsilon_1) - n_1^2 m_3^2} + \frac{2\epsilon_5 (n_1^2 - \epsilon_3) \cos(\mathbf{h}_2 \cdot \mathbf{r})}{(n_1^2 - \epsilon_3)(p_3^2 - \epsilon_1) - n_1^2 p_3^2} \right] E_2^0 e^{i\mathbf{k} \cdot \mathbf{r}} \\ E_2(\mathbf{r}) = E_2^0 e^{i\mathbf{k} \cdot \mathbf{r}} \\ E_3(\mathbf{r}) = \left[\frac{2\epsilon_4 (m_3^2 - \epsilon_1) \cos(\mathbf{h}_1 \cdot \mathbf{r})}{(n_1^2 - \epsilon_3)(m_3^2 - \epsilon_1) - n_1^2 m_3^2} + \frac{2i\epsilon_5 n_1 p_3 \sin(\mathbf{h}_2 \cdot \mathbf{r})}{(n_1^2 - \epsilon_3)(p_3^2 - \epsilon_1) - n_1^2 p_3^2} \right] E_2^0 e^{i\mathbf{k} \cdot \mathbf{r}} \end{array} \right. \quad (3-32)$$

$$\text{with } n_1^2 = \epsilon_2 + \frac{2\epsilon_4^2 (m_3^2 - \epsilon_1)}{(n_1^2 - \epsilon_3)(m_3^2 - \epsilon_1) - n_1^2 m_3^2} + \frac{2\epsilon_5^2 (n_1^2 - \epsilon_3)}{(n_1^2 - \epsilon_3)(p_3^2 - \epsilon_1) - n_1^2 p_3^2}$$

$$\approx \epsilon_2 - \frac{2\epsilon_4^2}{\epsilon_3} - \frac{2\epsilon_5^2(n_1^2 - \epsilon_3)}{p_3^2 \epsilon_3} \approx \epsilon_2 - \frac{2\epsilon_4^2}{\epsilon_3}.$$

$$\left\{ \begin{array}{l} E_1(\mathbf{r}) = 0 \\ E_2(\mathbf{r}) = \left[\frac{2\epsilon_4 \cos(\mathbf{h}_1 \cdot \mathbf{r})}{n_1^2 + m_3^2 - \epsilon_2} \right] E_3^0 e^{i\mathbf{k} \cdot \mathbf{r}} \\ E_3(\mathbf{r}) = E_3^0 e^{i\mathbf{k} \cdot \mathbf{r}} \end{array} \right. \quad (3-33)$$

$$\text{with } n_1^2 = \epsilon_3 + \frac{2\epsilon_4^2}{n_1^2 + m_3^2 - \epsilon_2} \approx \epsilon_3 + \frac{2\epsilon_4^2}{m_3^2} \approx \epsilon_3.$$

$$\mathbf{n} = (0, n_2, 0)$$

$$\left\{ \begin{array}{l} E_1(\mathbf{r}) = E_1^0 e^{i\mathbf{k} \cdot \mathbf{r}} \\ E_2(\mathbf{r}) = \left[\frac{2\epsilon_5(n_2^2 - \epsilon_3) \cos(\mathbf{h}_2 \cdot \mathbf{r})}{(n_2^2 - \epsilon_3)(p_3^2 - \epsilon_2) - n_2^2 p_3^2} \right] E_1^0 e^{i\mathbf{k} \cdot \mathbf{r}} \\ E_3(\mathbf{r}) = \left[\frac{2i \epsilon_5 n_2 p_3 \sin(\mathbf{h}_2 \cdot \mathbf{r})}{(n_2^2 - \epsilon_3)(p_3^2 - \epsilon_2) - n_2^2 p_3^2} \right] E_1^0 e^{i\mathbf{k} \cdot \mathbf{r}} \end{array} \right. \quad (3-34)$$

$$\text{with } n_2^2 = \epsilon_1 + \frac{2\epsilon_5^2(n_2^2 - \epsilon_3)}{(n_2^2 - \epsilon_3)(p_3^2 - \epsilon_2) - n_2^2 p_3^2} \approx \epsilon_1 - \frac{2\epsilon_5^2(n_2^2 - \epsilon_3)}{p_3^2 \epsilon_3}.$$

$$\left\{ \begin{array}{l} E_1(\mathbf{r}) = 0 \\ E_2(\mathbf{r}) = \left[\frac{2\epsilon_4(n_2^2 - \epsilon_3) \cos(\mathbf{h}_1 \cdot \mathbf{r})}{(n_2^2 - \epsilon_3)(m_3^2 - \epsilon_2) - n_2^2 m_3^2} \right] E_3^0 e^{i\mathbf{k} \cdot \mathbf{r}} \\ E_3(\mathbf{r}) = \left[1 + \frac{2i \epsilon_4 n_2 m_3 \sin(\mathbf{h}_1 \cdot \mathbf{r})}{(n_2^2 - \epsilon_3)(m_3^2 - \epsilon_2) - n_2^2 m_3^2} \right] E_3^0 e^{i\mathbf{k} \cdot \mathbf{r}} \end{array} \right. \quad (3-35)$$

$$\text{with } n_2^2 = \epsilon_3 + \frac{2\epsilon_4^2(n_2^2 - \epsilon_3)}{(n_2^2 - \epsilon_3)(m_3^2 - \epsilon_2) - n_2^2 m_3^2} \approx \epsilon_3 + \frac{2\epsilon_4^2(n_2^2 - \epsilon_3)}{\epsilon_3 m_3^2}.$$

$$\mathbf{n} = (0, 0, n_3)$$

$$\left\{ \begin{array}{l} E_1(\mathbf{r}) = E_1^0 e^{i\mathbf{k}\cdot\mathbf{r}} \\ E_2(\mathbf{r}) = \left[\frac{\epsilon_5}{(n_3 + p_3)^2 - \epsilon_2} e^{ih_2 \mathbf{r}} + \frac{\epsilon_5}{(n_3^2 - p_3)^2 - \epsilon_2} e^{-ih_2 \mathbf{r}} \right] E_1^0 e^{i\mathbf{k}\cdot\mathbf{r}} \\ E_3(\mathbf{r}) = \left[-2 \frac{\epsilon_4}{\epsilon_3} \cos(\mathbf{h}_1 \cdot \mathbf{r}) \right] E_1^0 e^{i\mathbf{k}\cdot\mathbf{r}} \end{array} \right. \quad (3-36)$$

$$\text{with } n_3^2 = \epsilon_1 + \frac{\epsilon_5^2}{(n_3 + p_3)^2 - \epsilon_2} + \frac{\epsilon_5^2}{(n_3 - p_3)^2 - \epsilon_2} \approx \epsilon_1 + 2 \frac{\epsilon_5^2}{p_3^2} \approx \epsilon_1.$$

$$\left\{ \begin{array}{l} E_1(\mathbf{r}) = \left[\frac{\epsilon_5}{(n_3 + p_3)^2 - \epsilon_1} e^{ih_2 \mathbf{r}} + \frac{\epsilon_5}{(n_3^2 - p_3)^2 - \epsilon_1} e^{-ih_2 \mathbf{r}} \right] E_2^0 e^{i\mathbf{k}\cdot\mathbf{r}} \\ E_2(\mathbf{r}) = E_2^0 e^{i\mathbf{k}\cdot\mathbf{r}} \\ E_3(\mathbf{r}) = \left[-2 \frac{\epsilon_4}{\epsilon_3} \cos(\mathbf{h}_1 \cdot \mathbf{r}) \right] E_2^0 e^{i\mathbf{k}\cdot\mathbf{r}} \end{array} \right. \quad (3-37)$$

$$\begin{aligned} \text{with } n_3^2 &= \epsilon_2 + \frac{\epsilon_5^2}{(n_3 + p_3)^2 - \epsilon_1} + \frac{\epsilon_5^2}{(n_3 - p_3)^2 - \epsilon_1} - 2 \frac{\epsilon_4}{\epsilon_3} \\ &\approx \epsilon_2 - 2 \frac{\epsilon_4}{\epsilon_3} + 2 \frac{\epsilon_5^2}{p_3^2} \approx \epsilon_2 - 2 \frac{\epsilon_4}{\epsilon_3}. \end{aligned}$$

In the different expressions for the refractive indices n_i , several approximations are given for which $m_3, p_3 \gg n_i$ and $\epsilon_1, \epsilon_2, \epsilon_3 \gg \epsilon_4, \epsilon_5$ is used. As a direct consequence, the refractive indices have values that differ only slightly from the ones in case of a macroscopic tensor. The solutions show a rocking and/or forward/backward movement of the electric electric field amplitude, depending on the position along \mathbf{c}

in the crystal. The magnitude of the additional field components is, however, very small. The electric fields and refractive indices, at T_1 approach continuously the solutions of the para phase, if we assume that the Fourier components $\epsilon(\mathbf{h})$ of the dielectric tensor can be written as a power series of the modulation amplitude. At the lock-in transition a symmetry change occurs, the mirror perpendicular to y being lost. Moreover, the wave vectors $(0,0,l,\bar{m})$ lose their long wavelength character, jumping to multiple values of \mathbf{c}^* . For intermediate temperatures, between the sinusoidal regime and the actual lock-in transition (the so-called discommensuration regime), the modulation involves more and more higher harmonics of the modulation wave with decreasing temperature. In this regime the temperature dependence of the wave vector also becomes stronger, but still can be written as $\mathbf{q} = (\frac{1}{3} - \delta(T))\mathbf{c}^*$. The first vector resulting from the continued fractions expansion remains $(0,0,1,\bar{3})$, while the following series of vectors rapidly changes with temperature. Thus, we expect the optical properties due to the modulation in the discommensuration regime to be mainly effected by this Fourier wave vector $(0,0,1,\bar{3})$, with a gradual increase of the importance of its higher harmonics and relatively rapidly changing contributions as a function of temperature of the remaining vectors in the continued fractions expansion. These latter vectors can in principle have contributions to all dielectric tensor components. For the odd harmonics of $(0,0,1,\bar{3})$ both l and m are odd, while for the even harmonics both are even. In (3-28) we then find that the even harmonics only contribute to the diagonal tensor, which is the tensor form of the basic dielectric tensor, while all odd harmonics contribute to the element ϵ_4 . Therefore, the optical properties are mainly determined by the tensor elements $\epsilon_1, \dots, \epsilon_4$, resulting in a continuous behaviour in the discommensuration regime, despite the strong temperature dependence of the modulation. At the lock-in transition one can expect a small discontinuity in the optical properties due to the jump of the wave vector to a commensurate value. In the lock-in phase the long-wavelength periodicities are no longer present, the vector $\mathbf{q} = \frac{1}{3}\mathbf{c}^*$ being the longest one. Because this length is small compared to the relevant vectors in the incommensurate phase, we expect the optical properties in the commensurate phase to be mainly determined by the macroscopic dielectric tensor $\epsilon(0)$, a normal constant (orthorhombic) diagonal tensor.

As was already stated by Fousek and Kroupa, the experimental observation of the small variations in the refractive indices is very difficult; they have to be isolated from the normal changes in refractive indices due to the thermal expansion of the cell.

3.4.3.3. Optical activity

In this section we will introduce the gyration tensor to the problem. For the description of optical activity we refer the reader to Sommerfeld¹⁶ and Born.²¹ The effect of gyration is understood to be due to a non-local dependence of the displacement field $\mathbf{D}(\mathbf{r})$ on the electric field $\mathbf{E}(\mathbf{r})$. Again, the problem is assumed to be static. Because of this dependence, one can expect the long wavelength structural properties of incommensurate phases to influence the gyration even more than the ordinary dielectric properties as described in the preceding section. The basic material equation (3-22) is statically rewritten in a Taylor approximation as

$$\mathbf{D}(\mathbf{r}) = \{\boldsymbol{\epsilon}(\mathbf{r}) + (\boldsymbol{\gamma}(\mathbf{r})\partial)\}\mathbf{E}(\mathbf{r}), \quad (3-38)$$

where the gyration tensor γ_{ijk} is a third rank tensor, antisymmetric in its first two indices. Again, γ_{ijk} is a material tensor and therefore it has the symmetry of the crystal, so that we can write the Fourier transform of (3-38) as

$$\mathbf{D}(\mathbf{k}) = \sum_{\mathbf{h} \in M'} \{\boldsymbol{\epsilon}(\mathbf{h}) + (i \boldsymbol{\gamma}(\mathbf{h})(\mathbf{k} - \mathbf{h}))\}\mathbf{E}(\mathbf{k} - \mathbf{h}), \quad (3-39)$$

where the differentiation has been performed. As $\gamma_{ijk}(\mathbf{r}) = -\gamma_{ikj}(-\mathbf{r})$ and $\gamma_{ijk}(\mathbf{r})$ is a real tensor, one has $\gamma_{ijk}(\mathbf{h}) = -\gamma_{ikj}(-\mathbf{h})$. Before determining its form, we briefly describe the contraction of $\boldsymbol{\gamma}$ to a vector $\boldsymbol{\gamma}^{(k)}$, the so-called gyration vector, and a second rank pseudo tensor g_{ij} , which are normally used to describe the gyration properties of crystals. First a second rank antisymmetrical tensor is introduced by

$$\gamma_{ij}^{(k)}(\mathbf{h}) = \gamma_{ijl}(\mathbf{h})k_l \quad (3-40)$$

The gyration vector is then written as

$$\boldsymbol{\gamma}^{(k)}(\mathbf{h}) = \frac{1}{2}e_{ijl}\gamma_{ijl}^{(k)}(\mathbf{h}), \quad (3-41)$$

where $e_{ijl} = \frac{1}{2}(i-j)(j-l)(l-i)$, resulting in

$$\mathbf{D}(\mathbf{k}) = \sum_{\mathbf{h} \in \Lambda_i} \{\boldsymbol{\epsilon}(\mathbf{h})\mathbf{E}(\mathbf{k} - \mathbf{h}) - i \boldsymbol{\gamma}^{(k-b)}(\mathbf{h}) \times \mathbf{E}(\mathbf{k} - \mathbf{h})\}. \quad (3-42)$$

The effect of optical activity is now observed as a rotation of the polarisation around the wave normal \mathbf{k} of the light, whenever $\mathbf{k} \cdot \boldsymbol{\gamma}^{(k)}(\mathbf{r}) \neq 0$, the effect of the birefringence on the optical activity being neglected. A more common notation for

l, m \mathbf{k}	0,0	o,o	e,e	o,e	e,o
(1,0,0)	$\begin{bmatrix} 0 \\ 0 \\ 0 \end{bmatrix}$	$\begin{bmatrix} 0 \\ 0 \\ \gamma_{121} \end{bmatrix}$	$\begin{bmatrix} 0 \\ -\gamma_{131} \\ 0 \end{bmatrix}$	$\begin{bmatrix} 0 \\ 0 \\ 0 \end{bmatrix}$	$\begin{bmatrix} \gamma_{231} \\ 0 \\ 0 \end{bmatrix}$
(0,1,0)	$\begin{bmatrix} 0 \\ 0 \\ 0 \end{bmatrix}$	$\begin{bmatrix} 0 \\ 0 \\ 0 \end{bmatrix}$	$\begin{bmatrix} \gamma_{232} \\ 0 \\ 0 \end{bmatrix}$	$\begin{bmatrix} 0 \\ 0 \\ \gamma_{122} \end{bmatrix}$	$\begin{bmatrix} 0 \\ -\gamma_{132} \\ 0 \end{bmatrix}$
(0,0,1)	$\begin{bmatrix} 0 \\ 0 \\ 0 \end{bmatrix}$	$\begin{bmatrix} \gamma_{233} \\ 0 \\ 0 \end{bmatrix}$	$\begin{bmatrix} 0 \\ 0 \\ 0 \end{bmatrix}$	$\begin{bmatrix} 0 \\ -\gamma_{133} \\ 0 \end{bmatrix}$	$\begin{bmatrix} 0 \\ 0 \\ \gamma_{123} \end{bmatrix}$
(1,1,0)	$\begin{bmatrix} 0 \\ 0 \\ 0 \end{bmatrix}$	$\begin{bmatrix} 0 \\ 0 \\ \gamma_{121} \end{bmatrix}$	$\begin{bmatrix} \gamma_{232} \\ -\gamma_{131} \\ 0 \end{bmatrix}$	$\begin{bmatrix} 0 \\ 0 \\ \gamma_{122} \end{bmatrix}$	$\begin{bmatrix} \gamma_{231} \\ -\gamma_{132} \\ 0 \end{bmatrix}$
(0,1,1)	$\begin{bmatrix} 0 \\ 0 \\ 0 \end{bmatrix}$	$\begin{bmatrix} \gamma_{233} \\ 0 \\ 0 \end{bmatrix}$	$\begin{bmatrix} \gamma_{232} \\ 0 \\ 0 \end{bmatrix}$	$\begin{bmatrix} 0 \\ -\gamma_{133} \\ \gamma_{122} \end{bmatrix}$	$\begin{bmatrix} 0 \\ -\gamma_{132} \\ \gamma_{123} \end{bmatrix}$
(1,0,1)	$\begin{bmatrix} 0 \\ 0 \\ 0 \end{bmatrix}$	$\begin{bmatrix} \gamma_{233} \\ 0 \\ \gamma_{121} \end{bmatrix}$	$\begin{bmatrix} 0 \\ -\gamma_{131} \\ 0 \end{bmatrix}$	$\begin{bmatrix} 0 \\ -\gamma_{133} \\ 0 \end{bmatrix}$	$\begin{bmatrix} \gamma_{231} \\ 0 \\ \gamma_{123} \end{bmatrix}$

Table 3-III. The form of the gyration vectors $\gamma^{(k)}(\mathbf{h})$ for different wave vectors of the light (\mathbf{k}) and all parity conditions of l and m in $\mathbf{h} = (0,0,l,m)$. e denotes even, o denotes odd. The entries are given in terms of the gyration tensor element γ_{ijk} (see (3-38)).

the optical activity is in terms of a second rank real pseudo tensor g_{ij} , which can be defined from

$$\gamma_i = -g_{ij}k_j \quad (3-43)$$

The symmetry properties for the g_{ij} can be found e.g. in Nye.¹⁰

Returning to equation (3-38), we will determine the form of γ_{ijk} , using the superspace symmetry of the crystal. The symmetry condition for $\gamma_{ijk}(\mathbf{h})$ now reads

$$\gamma_{ijk}(\mathbf{h}) = R_{lm}R_{jn}R_{kp}\gamma_{mnp}(\mathbf{R}\mathbf{h})e^{i(\mathbf{R}\mathbf{h},\mathbf{h}_i)} \quad (3-44)$$

For $\mathbf{h} = 0$ this again leads to $\gamma_{ijk}(0) = 0$, predicting no optical activity within this approximation. The observed effect is thus due to the modulation dependent ($m \neq 0$) wave vectors and again we restrict our considerations to those given in (3-26). In order to obtain results which can directly be related to the experimental directions of the wave normals, we give the gyration vectors for different directions of \mathbf{k} , for all parity conditions of l, m in $\mathbf{h} = (0, 0, l, m)$, in Table 3-III. If we restrict to the first Fourier wave vector of importance ($\mathbf{h} = (0, 0, 1, \bar{3})$) we find in this table, without specifying the exact form of the fields (which still need further investigation), that optical activity can only be present for the direction $\mathbf{k} = (k_1, 0, k_3)$, or more general for \mathbf{k} with $\mathbf{k} \times \mathbf{b} \neq 0$. All other directions for \mathbf{k} are perpendicular to the corresponding gyration vector. Physically this is understood as follows. Only the fields for $\mathbf{k} = (k_1, 0, k_3)$ can show gyrational effects due to the coupling with fields with wave vector $\mathbf{k} \pm (0, 0, 1, \bar{3})$. If we include the next Fourier component $\mathbf{h}_2 = (0, 0, 2, \bar{7})$, we find that rotation is in principle possible for all directions of \mathbf{k} . The appearance of a net observable rotation depends on other conditions as well, which are not yet fully explored. Some of the expected ones are presented in section 3.4.5.

3.4.4. Experimental

3.4.4.1. HAUP polarimeter

The measurements were performed by means of a HAUP polarimeter as described by Kobayashi *et al.*⁴ The light source was a He-Ne laser (632.8 nm); the extinction ratio of the polariser and analyser were specified to be 10^{-6} ; the resolution of the stepping motor driven Nicols was approximately $.001^\circ$. For all measurements the polarisers were rotated both from -0.5° to $+0.5^\circ$ with respect to their zero positions, with intervals of 0.05° . For each position the intensity was

measured with a photon counting system for a period of 1 s and corrected with a reference signal to take care of drift in the laser output power.

3.4.4.2. Temperature control

The sample was mounted on a cold/hot finger with as few stress as possible to avoid induced optical activity. Thermal contact was improved with thermal paste. The sample was completely surrounded by a copper radiation shield at the samples temperature (except for two small holes for the transmitted light). Temperature was controlled with a heater in the cold/hot finger and a Pt-100 resistor as a thermometer. For temperatures below room temperature the sample was cooled with an additional N₂ or He flow through the cold finger. A second Pt-100 resistor, mounted in the sample holder was used to measure the temperature of the sample. The temperature stability was always better than ± 0.01 K and the absolute error was estimated to be less than ± 1 K.

3.4.4.3. Samples

The samples used were grown with a modified Bridgman technique. Starting material was obtained from crystals grown from an aqueous solution containing RbBr and ZnBr₂ in the molar ratio 2:1, slightly acidified with concentrated HCl to improve growth. The growing rate from the melt was 0.6 mm/h. The thus obtained transparent crystal was cleaved perpendicular to **a**, oriented further with a polarising microscope and sawed with a string saw. The faces to be used for the experiment were polished to a local flatness of about 1 μ . All samples were measured no longer than one day after they were polished in order to avoid contamination of the surfaces due to the hygroscopic nature of the material.

The off-diagonal gyration tensor elements were measured along the bisectors of the corresponding axes with the exception of g_{13} , which was measured along a direction tilted over 15° from the bisector towards the **a**-axis, because the optical axis turned out to be approximately along this bisector (at room temperature). All three samples used were obtained from the same melt growth. The samples are denoted

as RZB_{ij} , where the indices indicate the orientation of the cut as adapted to the measurement of the tensor element g_{ij} . Their dimensions were

- RZB₁₁: $\approx 5 \times 8 \text{ mm}^2$ and 1.65 mm thick
 RZB₁₂: $\approx 8 \times 12 \text{ mm}^2$ and 1.95 mm thick
 RZB₁₃: $\approx 8 \times 12 \text{ mm}^2$ and 1.01 mm thick.

3.4.4.4. Results and evaluation

For the evaluation of the results we used the following procedure. All data were fitted to the following formula describing the measured intensity (I_0) in terms of the polariser position (Θ) and the analyser position (Λ):

$$I = I_0 \{ A_0 + \{ \chi - \cos(\Delta/2)(\Theta - \Lambda) \}^2 + \{ \sin^2(\Delta/2)(\Theta + \Lambda) \}^2 \} \quad (3-45)$$

where I_0 is the incoming intensity, A_0 a background intensity due to scattering, $\chi = \{ (\gamma - 2k)\sin(\Delta/2) + \delta\Lambda\cos(\Delta/2) \}$ with $\gamma = p - a$ the difference in ellipticity of the polariser and the analyser, Δ is the phase difference for the light due to the sample, $\delta\Lambda$ is a measure for the misalignment of the sample and $k \approx g/(2\Delta\bar{n})$, where g is the optical activity and \bar{n} is the effective refractive index. This formula is in essence the same as the one given by Kobayashi⁴ and is derived elsewhere.²² The procedure suggested by Kobayashi,⁴ which fits the results to Y ($Y = \Theta - \Lambda$) and uses in a second fit to Θ the first fit results, was not adequate in our case because the data points scattered quite much, mainly due to problems with the mechanical interface between the stepping motors and the Nicols. Therefore we adopted this procedure only to obtain starting values for the parameters used in another fit procedure, which fits the data with respect to both Θ and Λ simultaneously. Thus we obtained values for $|\cos(\Delta/2)|$, χ , A_0 and I_0 as a function of temperature. One drawback of the HAUP technique is the fact that one always needs to know a value of Δ and the sign of $\partial\Delta/\partial T$ at a certain temperature because the measurement gives only values for $|\cos(\Delta/2)|$. Therefore the birefringence was measured for all three samples at room temperature. This was done by measuring very accurately the three refractive indices with an Abbe refractometer, using an interference filter to obtain light with a wave length of 634 nm. The results were ($T = 297 \pm 1 \text{ K}$):

$$n_a = 1.6448 \pm 0.0002$$

$$n_b = 1.6518 \pm 0.0004$$

$$n_c = 1.6573 \pm 0.0002$$

The refractive indices were also measured for other wave lengths; at 514.5 nm we found

$$n_a = 1.659$$

$$n_b = 1.666$$

$$n_c = 1.672.$$

These values are systematically smaller (0.3-0.5 %) than those obtained by Horix²³ but consistent with the data of Kusto *et al.*²⁴ ($\lambda = 589$ nm). The value for the birefringence was calculated for all three samples used ($\lambda = 634$ nm; Δn_{ij} is the birefringence as observed for light traveling along a direction perpendicular to the sample denoted by RZB_{ij}):

$$\Delta n_{11} = (5.5 \pm 0.5) 10^{-3}$$

$$\Delta n_{12} = (9.0 \pm 0.5) 10^{-3}$$

$$\Delta n_{13} = (2.3 \pm 0.5) 10^{-3}.$$

These values were used to extract the correct values for the birefringence as a function of temperature from the fit results for $|\cos(\Delta/2)|$. The sign of the slope for this function was assumed to be the same as for Rb_2ZnCl_4 and taken from Ref. 15. Both γ and $\delta\Delta$ are assumed to be independent of temperature. The value for $\delta\Delta$ was obtained by averaging all values of $\chi/\cos(\Delta/2)$ with $\sin^2(\Delta/2) < 0.5$; the value γ by averaging all values of $(\chi - \delta\Delta\cos(\Delta/2))/\sin(\Delta/2)$ in the paraelectric phase, where $k = 0$. In this way, $g = 2k\Delta\tilde{n}$ was obtained as a function of temperature. The results for the birefringence are given in Fig. 3.4-a, b and c; those for the optical activity in Fig. 3.5-a, b and c.

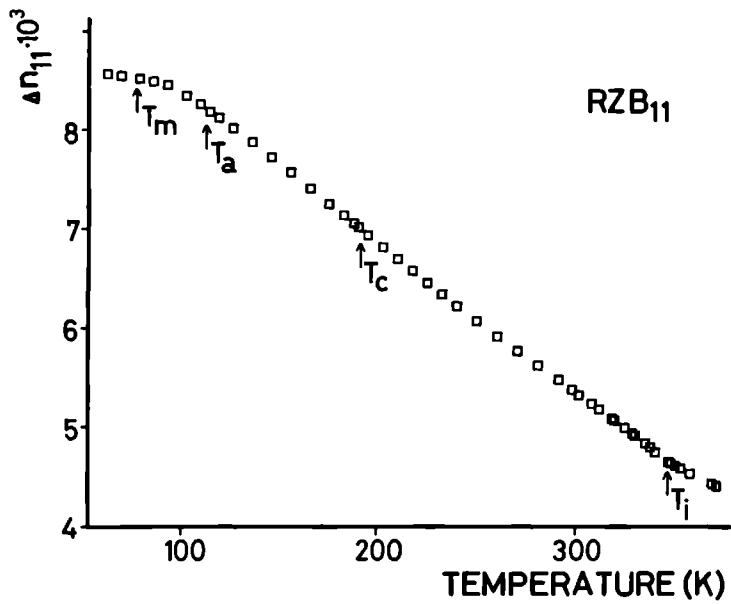


Figure 3 4-a The birefringence as a function of temperature for RZB₁₁ (Δn_{yz})
Indicated are the different phase transitions

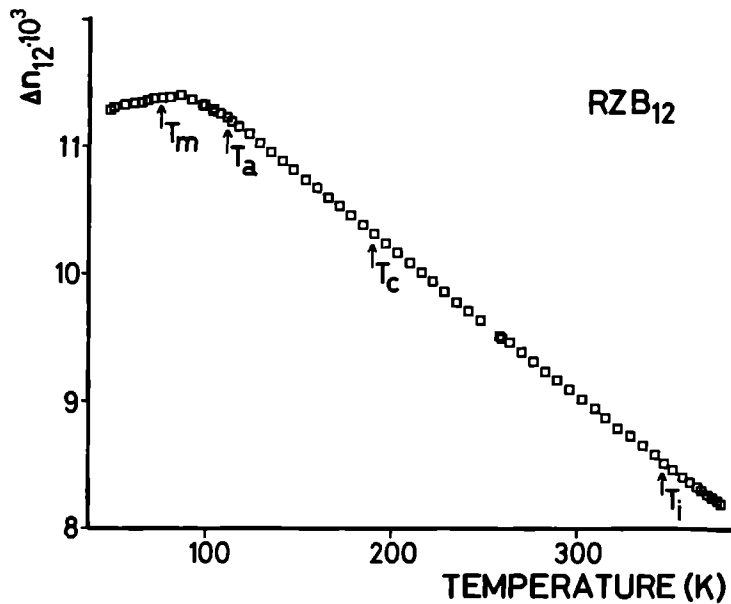


Figure 3 4-b The birefringence as a function of temperature for RZB₁₂
($\Delta n_{zx} - \frac{1}{2} \Delta n_{yx}$) Indicated are the different phase transitions

3.4.5. Discussion

3.4.5.1. Rb_2ZnBr_4

We will first concentrate on the results for the birefringence as a function of temperature. At this point we have to emphasise that the small jumps in the

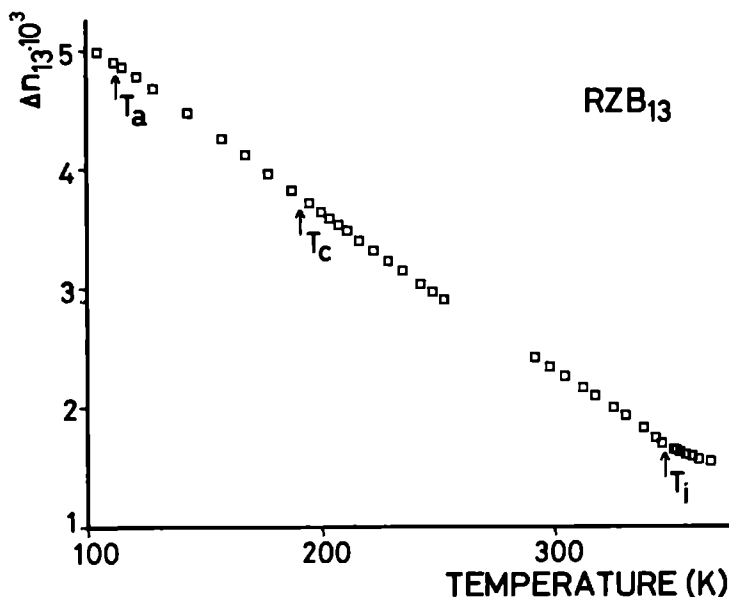


Figure 3 4-c The birefringence as a function of temperature for RZB_{13} ($\Delta n_{xy} - \frac{3}{4} \Delta n_{xz}$) Indicated are the different phase transitions

birefringence as predicted in section 3 4 3 can not be observed by means of HAUP. Very precise differential measurements of the birefringence however, can reveal those jumps.²⁵ Our comparisons with Rb_2ZnCl_4 refer to Sanctuary¹⁵

For RZB₁₁ we see in Fig. 3.4-a that the value of Δn_{23} increases almost linearly with increasing temperature within the incommensurate phase and the lock-in phase (III). There is no clear change at the lock-in transition temperature (T_c). Above T_1 , the slope diminishes; the same behaviour can be seen for temperatures in phase IV and V. The behaviour in the neighbourhood of T_1 is confirmed by the measurements of Kusto *et al.*,²⁴ although they found a value of $\Delta n_{11} = 4.5 \cdot 10^{-3}$ at 300 K for $\lambda = 632.8$ nm, where we find $\Delta n_{11} = 5.3 \cdot 10^{-3}$.

For RZB₁₂, the birefringence ($\Delta n_{zx} - \frac{1}{2} \Delta n_{yx}$) shows the same behaviour as for RZB₁₁, only the slope in the para phase is in this case almost the same as in the incommensurate phase. At T_c a very small change in the slope is present. In the neighbourhood of the phase transition to phase V, the sign of the slope changes. In phase V the slope seems to be constant again, while in the intermediate phase IV the behaviour is far from linear.

For RZB₁₃, again an analogous behaviour is observed, although no measurements were done in phase V. The change in slope at T_1 is more pronounced than for RZB₁₂ and in the neighbourhood of T_c , again, a very small change in slope can be seen. In all three cases, the slope is in the incommensurate and lock-in phase approximately $0.5-1 \cdot 10^{-5} \text{ K}^{-1}$, which is comparable with the result found for Rb₂ZnCl₄. The changes in the neighbourhood of the transition temperatures to phases IV and V do not coincide with the reported temperatures (112 K and 77 K). In fact, at 112 K only small gradual changes are observed, which is in agreement with the reported⁵ small differences between phases III and IV. The change in the sign of the slope in the case of RZB₁₂ is probably related to the phase transition to phase V, indicating a higher transition temperature in our sample (≈ 85 K). The highest temperature reported for this transition is 80 K.⁸

Next we will devote our attention to the optical activity. As was mentioned before, one can see in Fig. 3.5 that the data points scatter quite much. Nevertheless we can draw the following conclusions.

The gyration coefficient g_{11} stays small ($< 1 \cdot 10^{-5}$) for all temperatures measured. The small gradual increase with decreasing temperature is probably due to a small change of $\delta\Lambda$ with temperature. Except for phase V, the same holds for g_{12} ($< 1 \cdot 10^{-5}$). Below approximately 77 K, g_{12} systematically increases.

A different behaviour is observed for g_{13} . This coefficient increases considerably at T_1 and continues to do so down to the lowest temperature measured (≈ 100 K). At T_c , the value for g_{13} is approximately $2.3 \cdot 10^{-5}$; cf. Rb₂ZnCl₄, where $g_{13}(T_c) \approx 4.0 \cdot 10^{-5}$. The slope is approximately $-1.0 \cdot 10^{-7} \text{ K}^{-1}$. (In Rb₂ZnCl₄: $-4.5 \cdot 10^{-7} \text{ K}^{-1}$).

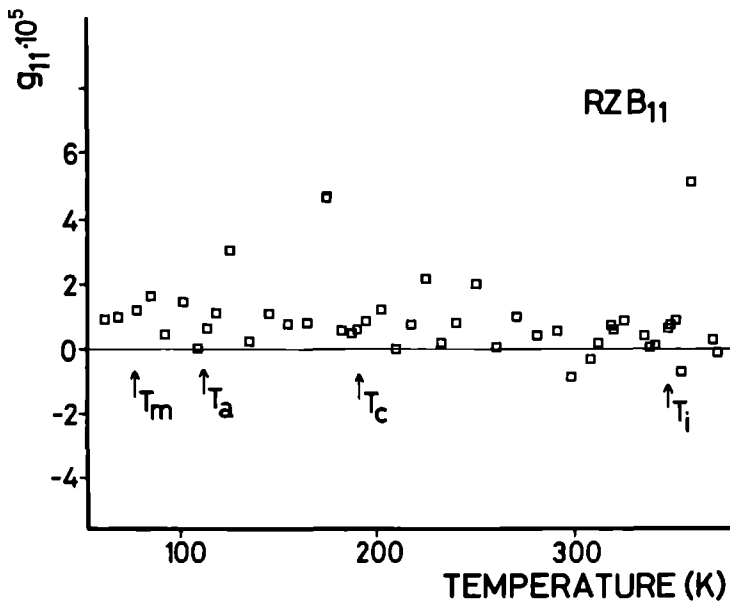


Figure 3.5-a. The gyration tensor element (g_{11}) as a function of temperature for RZB_{11} . Indicated are the different phase transitions.

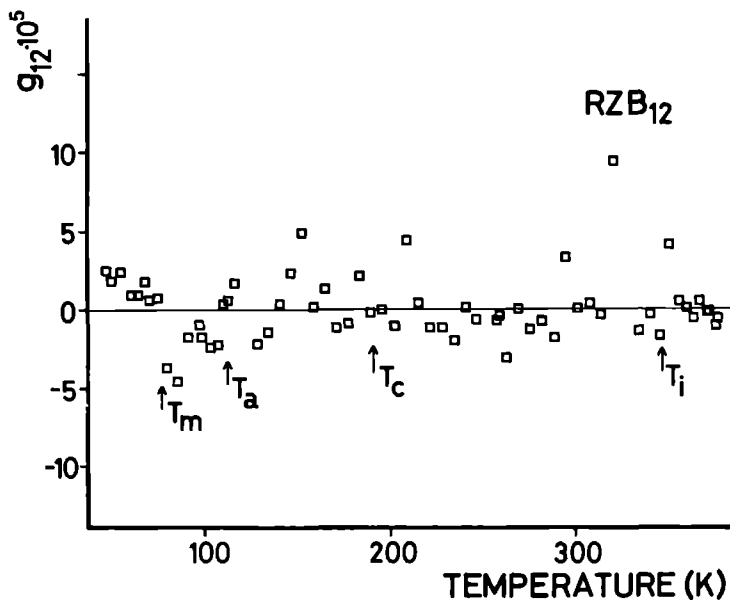


Figure 3.5-b. The gyration tensor element (g_{12}) as a function of temperature for RZB_{12} . Indicated are the different phase transitions.

If we compare these results with the predictions for the commensurate phases given in section 3.4.2, we see that both values are consistent. The value of g_{13} increases down to 100 K, indicating that the order parameter responsible for the optical activity does the same. The nonzero value for g_{12} in phase V indicates that the symmetry element n_z of phase III and IV is lost indeed, resulting in the point group symmetry m_x consistent with the predicted space group $Pc11$. If we compare this result with Rb_2ZnCl_4 , where also a low temperature phase transition to a monoclinic phase (probably $Pc11$) is found,²⁶ we observe that the phase transition temperatures in the two compounds do not differ much. ($T_1 = 303$ K (437 K), $T_c = 192$ K (190 K) and $T_m = 75$ K (77 K) for Rb_2ZnCl_4 (Rb_2ZnBr_4)). Unfortunately, the optical activity in Rb_2ZnCl_4 has only been determined for g_{13} and only down to 150 K.

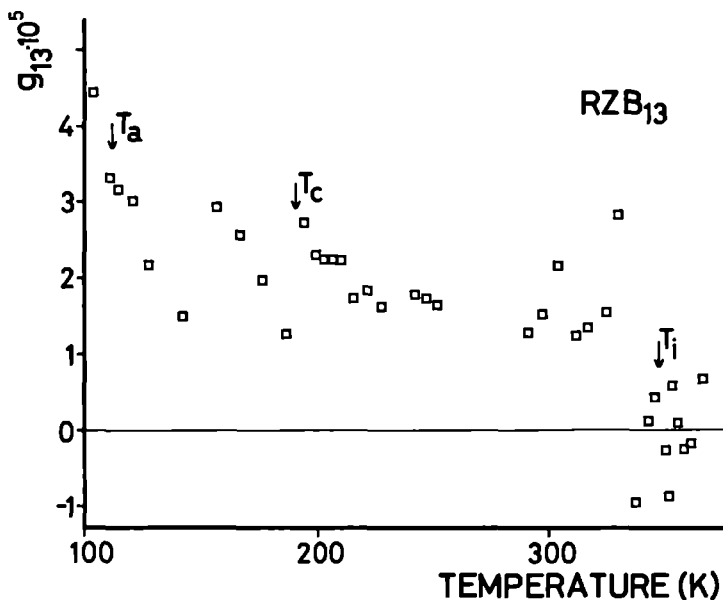


Figure 3.5-c. The gyration tensor element (g_{13}) as a function of temperature for RZB_{13} . Indicated are the different phase transitions.

The non-zero value of g_{13} in the incommensurate phase is in agreement with the predictions of section 3.4.3. Moreover, the fact that g_{11} and g_{12} stay relatively small indicates that in Rb_2ZnBr_4 the contributions to the optical activity of the Fourier component $\mathbf{h} = (0,0,1,3)$ are far more important than those of the next one (cf. (3-26)).

The fact that g_{13} has a non-zero value in the incommensurate phase was also observed in Rb_2ZnCl_4 , the only difference is that Sanctuary¹⁵ finds a nonzero value starting about 50 degrees below T_1 , while Uesu *et al.*¹⁴ find (as we do for Rb_2ZnBr_4) a nonzero value immediately below T_1 . On the other hand, in both Sanctuary's and our case g_{13} increases monotonically (almost linearly) with decreasing temperature, while Uesu and Kobayashi report a tendency for the gyration to go to zero at the lock-in transition and increase again on entering the lock-in phase. Kobayashi *et al.* reported this behaviour also for $[\text{N}(\text{CH}_3)_4]_2\text{ZnCl}_4$, for which they found another result, where g_{13} does not go to zero at T_c , but rather jumps to a larger value, in later measurements.⁴ Therefore the effect at T_1 seems to depend on the sample. This is consistent with the view of Saito *et al.*²⁷ that domain walls (solitons) represented by discommensuration regions between nearly commensurate domains have an influence on the gyration tensor. Pinning, due to defects, enhance these effects. This situation can also be described within the present approach, by including higher harmonics in the Fourier components considered. On the other hand, our measurements show very little variation with temperature within the full incommensurate phase, so that no appreciable difference is observed between the typical sinusoidal regime (near the incommensurate phase transition temperature) and the discommensuration regime, near the lock-in phase. This fact can be considered to support the present approach in terms of relevant nonzero Fourier waves. There is a possibility for a net rotation, despite the periodic spatial dependence of the gyration tensor considered, that is connected with the same periodic properties of the dielectric tensor, which influence the stabilisation of layers relevant for domains, defects and/or morphologically stable faces. Accordingly, not all gyration amplitudes are equally probable, leading to a net rotation which is possibly crystal dependent.

3.4.5.2. Other A_2BX_4 -compounds

As the incommensurate phases of all members of the A_2BX_4 family of dielectrics, studied up to now are believed to have as their symmetry the superspace group $Pcmn(00\gamma)(ss\bar{1})^1$, a generalisation of our results for Rb_2ZnBr_4 to the other members is appealing. This generalisation however, has to take into account the different continued fractions expansions of the modulation parameters γ , which are not the same for different compounds and can be temperature dependent. The Fourier wave vector corresponding to the first term in this expansion is not necessarily $(0,0,1,\frac{1}{3})$ or more general $(0,0,l,m)$ with both l and m odd. In Rb_2ZnBr_4 the modulation wave vector is independent of temperature for a large temperature range of the incommensurate phase; approximately ten degrees K above the lock-in phase transition, it starts to deviate from this constant value.

In Rb_2ZnCl_4 a comparable behaviour is observed. The value of the modulation wave vector is fairly constant ($\gamma \approx 0.31$).²⁸ Its continued fractions expansion starts with $1/3$, the next approximation being already $11/34$. A few degrees above T_c (190 K), the value of γ is approximately 0.32, with as its first two fractional approximations $1/3$ and $8/25$. This example shows that the contributions of the first Fourier wave vector $(0,0,1,\frac{1}{3})$ are expected to be the most prominent ones throughout the incommensurate phase. Of course the effect of higher harmonics, playing a more substantial role in the neighbourhood of the lock-in transition, can change this situation.

In $[N(CH_3)_4]_2ZnCl_4$ (TMAZC), however, the modulation wave vector is much more temperature dependent. Furthermore, its continued fractions expansion (of $\gamma = 0.42$ at $T = 290$ K) provides as first approximation $\mathbf{h} = (0,0,2,\frac{1}{5})$, thus predicting (see Table 3-III) the possibility of optical activity for every direction of \mathbf{k} . Unfortunately, the gyration effect in this compound has only been studied for the direction $\mathbf{k} = (k_1, 0, k_3)$,⁴ where a small (one hundred times smaller as compared to Rb_2ZnBr_4) effect was observed. Nevertheless, it would be interesting to measure the optical activity for other directions in TMAZC. One has to note however, that the relevant $\gamma_{i,j,k}$ can differ in magnitude. On the other hand, table III together with (3-43) shows that if g_{13} is observable (which is experimentally verified), also g_{11} or g_{33} and probably g_{12} or g_{23} should be observable and have the same order of magnitude as g_{13} . The change of γ as a function of temperature, however, makes it more difficult to find the appropriate continued fractions expansion. We realise that this variation of γ with temperature implies, within our model, that different tensor

components get bigger and smaller in value as the temperature is lowered. The correct interpretation and physical consequences of this behaviour will be disregarded here, but will certainly be a topic of future work.

3.4.6. Conclusion

We have measured the gyration coefficients g_{11} , g_{12} and g_{13} as well as the birefringence of the corresponding directions in Rb_2ZnBr_4 in its paraelectric phase, the incommensurate phase and the lock-in phase. g_{11} and g_{12} were also determined in the low-temperature monoclinic phase.

As far as the commensurate phases are concerned, the expected gyration effects, on ground of symmetry, are in agreement with the experimental results. The phase transition at T_a (112 K) between two orthorhombic phases with the same symmetry has no observable effects on the optical activity, nor on the birefringence. The existence of a low-temperature monoclinic phase ($T < 77$ K) is confirmed. The lock-in transition has very small influence on the optical properties. The linear dependence of the birefringence on temperature changes its slope slightly at T_c .

In the incommensurate phase optical activity was observed only for g_{13} . In order to explain the observed effect, we developed a phenomenological theory on the basis of the superspace symmetry of this phase. In this theory, the dielectric tensor and the gyration tensor are semi-microscopic (local) entities. Note that this is commonly also done for X-ray diffraction in the kinematic approximation. The Fourier components $\epsilon(\mathbf{h})$ and $\gamma(\mathbf{h})$ have decreasing contributions to the propagation of light, with increasing h , but also with increasing integral components of \mathbf{h} as element of a fourth rank Z -module. The choice of the relevant Fourier components must be based on phenomenological grounds as long as a microscopic theory is not available. For normal crystals the smallest non-zero Fourier wave vector is a reciprocal lattice vector, whose wave length is very small compared to the wave length of the light used. In the incommensurate structure, however, relatively long wave length structural information is present in the Fourier expansion which can contribute substantially to the spatial variation expressed by $\epsilon(\mathbf{r})$ and $\gamma(\mathbf{r})$. The allowed Fourier components and their tensor forms follow from the superspace symmetry. We used the first three Fourier components expected to be of importance in Rb_2ZnBr_4 to find the electric fields in the absence of optical activity,

for the three principal directions of propagation. In the case of optical activity, we determined the symmetry of the different Fourier components of the gyration tensor and used these results to explain the observed effect in the incommensurate phase.

Finally a generalisation of the theory to other incommensurate structures has been discussed.

Acknowledgements

The measurements were performed in the group of Prof. Dr. P. Günter, Laboratorium für Festkörperphysik, ETH Zürich, Switzerland. We gratefully acknowledge the kind hospitality and in particular would like to thank Dr. Herbert Looser and Mr. J. Hajfler for their contributions.

This work is part of the research program of the Stichting voor Fundamenteel Onderzoek der Materie (Foundation for Fundamental Research on Matter) and was made possible by financial support from the Nederlandse Organisatie voor Zuiver-Wetenschappelijk Onderzoek (Netherlands Organisation for the Advancement of Pure Research).

References

1. A.C.R. Hogervorst, thesis, Delft (1986).
2. A. Janner and T. Janssen, *Acta Cryst.* **A33**, 493 (1977) and A. Janner and T. Janssen, *Phys. Rev.* **B15**, 643 (1977).
3. T. Janssen and A. Janner, *Advances of Physics* (1987), to appear.
4. J. Kobayashi, H. Kumomi and K. Saito, *J. Appl. Cryst.* **19**, 377 (1986) and references therein.
5. A.C.R. Hogervorst and R.B. Helmholtz, to appear in *Acta Cryst. B*.
6. R.P.A.R. van Kleef, Th. Rasing, J.H.M. Stoelinga and P. Wyder, *Solid State Commun.* **39**, 433 (1981).
7. I.A. Belobrova, I.P. Aleksandrova and A.K. Moskalev, *Phys. Stat. Sol. (a)* **66**, K17 (1981).
8. Tokashi Ueda, Satoshi Iida and Hikaru Terauchi, *J. Phys. Soc. Japan* **51**, 3953 (1982).
9. M. Iizumi and K. Gesi, *J. Phys. Soc. Jap.* **52**, 2526 (1983).
10. Nye, *Physical Properties of Crystals* (Oxford University Press, 1985), chapter XIV.
11. A. Janner and B.W. van Beest, *Proceedings of the XIth International Colloquium on Group Theoretical Methods in Physics, Istanbul, August 23-28, 1982*.
12. B.W. van Beest and A. Janner, *Physica* **122A**, 263 (1983).
13. B.W. van Beest, A. Janner and R. Blinc, *J. Phys. C. Solid State Phys.* **16**, 5409 (1983).
14. Y. Uesu and J. Kobayashi, *Ferroelectrics* **64**, 115 (1985).
15. R.A. Sanctuary, thesis, E.T.H. Zürich (1985).
16. See for example A. Sommerfeld, *Vorlesungen über Physik IV, Optik*.
17. V.A. Golovko and A.P. Levanyuk, *Sov. Phys. JETP.* **50**, 780 (1979).
18. J. Fousek and J. Kroupa, *Czech. J. Phys. B* **36**, 1192 (1986).
19. P.M. de Wolff, *Easy and Uneasy Superspace Groups*, lecture during the International Conference on Advanced Methods in X-ray and Neutron Analysis of Materials, 5-9 oktober 1987, Karlovy Vary (Czechoslovakia), to be published.

20. B.W.H. van Beest, *Phys. Rev.* **B33**, 960 (1986).
21. Born, *Optik* (Springer, Berlin, 1985).
22. H. Meekes, thesis, Nijmegen (1987).
23. J.J.L. Horikx, thesis, Utrecht (1987).
24. W.J. Kusto, R. Struikmans and B. Willemsen, Proc. Sixth European Meeting on Ferroelectrics, (Poznań), 258 (1987), to appear in *Ferroelectrics*.
25. M. Régis, J.L. Ribet and J.P. Jamet, *J. Physique* **L43**, L333 (1982).
26. M. Quilichini and J. Pannetier, *Acta Cryst.* **B39**, 657 (1983).
27. K. Saito, T. Kawabe and J. Kobayashi, *Ferroelectrics*, **75**, 153 (1987).
28. H. Mashyama, S. Tanisaki and K. Hamano, *J. Phys. Soc. Jap.* **50**, 2139 (1981).

CHAPTER 4

POINT-CONTACT SPECTROSCOPY IN INCOMMENSURATE CHROMIUM

4. Point-contact spectroscopy in incommensurate chromium

H. Meekes

Research Institute for Materials
University of Nijmegen, Toernooiveld,
6525 ED Nijmegen, The Netherlands

Abstract

The effects of the incommensurate spin density wave on the current-voltage characteristic in pure chromium are investigated, using point-contact spectroscopy. A simple model is given to account for the changes in the Sharvin current as due to the additional gaps in the density of states for the electron. The results are compared with the experimental data which show a large increase in the resistivity for voltages smaller than the gap energy.

4.1. Introduction

Chromium represents a very special element among the metals. This is due to the spin density wave formed by the conduction electrons below its Néel temperature at $T_N = 312 \text{ K}$. This state is even more interesting because of its nearly-antiferromagnetic character. In other words, chromium is incommensurate for temperatures below T_N . The incommensurate spin density wave has been studied very intensively by neutron diffraction experiments.¹

Due to the incommensurate nature of the electron spin wave, the density of states of the electrons shows many additional gaps besides the ordinary gaps which are a result of the normal lattice periodicity. These additional gaps are present for $2\mathbf{k} = \pm N\mathbf{Q} \pm \mathbf{K}$, where $\mathbf{Q} = 2\pi/a(\alpha, 0, 0)$ ($\alpha \approx 0.962$ at $T = 300 \text{ K}$), is the incommensurate wave vector, $\mathbf{K} \in \Lambda^*$, a reciprocal lattice vector and N is an integer. The size of these gaps is expected to become smaller for higher values of N . This structure results in an increase of the bulk resistivity by 35 % when changing from currents parallel to \mathbf{Q} to currents perpendicular to bold \mathbf{Q} .²

A first order ($N = 1$) gap has been observed by many authors³⁻⁵ in infrared reflectance measurements and was found to have a width of approximately 1000 cm^{-1} or 124 meV . The higher order gaps are expected to appear for much lower energies.

We decided to find out whether these gaps influence the conductivity by measuring the energy dependent resistance by means of point-contact spectroscopy. This technique allows for a sensitive detection of non-linear relation between the current and voltage for energies up to the order of 100 meV .

The paper is organised as follows. In section 4.2, the spin density wave and its effect on the density of states of the electrons in chromium are described. Section 4.3 deals with the basic aspects of point-contact spectroscopy and especially the effect of gaps in the density of states on the current through a point-contact. The next section briefly summarises the experimental techniques used and in section 4.5, the results are discussed. We end with a conclusion.

4.2. The structure and density of states in chromium

4.2.1. The structure of chromium

Above the Néel temperature, chromium forms a b.c.c. paramagnetic structure. At the phase transition to the incommensurate state (phase AF_1), a spin density wave (SDW) is formed, with a wave vector $\mathbf{Q} = \alpha\mathbf{a}^*$ and a transverse polarisation resulting in an orthorhombic basic symmetry ($Immm$). The coefficient α varies from 0.963 to 0.952 between T_N and 4 K. In this phase, domains are formed with the polarisation and \mathbf{Q} -vector along the (original) cubic axes. On lowering the temperature, a second phase transition occurs at 122 K to phase AF_2 , where the spin direction is flipped resulting in a longitudinal SDW, forming a tetragonal basic structure ($I4/mmm$). In both phases (AF_1 and AF_2) a small induced longitudinal displacive modulation of the lattice is observed,⁶ with wave vector $2\mathbf{Q}$. The superspace symmetry⁷ of the two incommensurate phases was found to be $G(AF_1) = PImmm(2\alpha,0,0)(\bar{1},1,1)$ and $G(AF_2) = PI4/mmm(2\alpha,0,0)(1,\bar{1},1,1)$.

4.2.2. The origin of the SDW

The origin of the itinerant spin wave seems to lie in the fact that the electron band structure of chromium has electron and hole states in the neighbourhood of the Fermi level, which are very comparable as their shapes in \mathbf{k} -space are concerned. Loomer⁸ found that the octahedral sheets for the electrons around the $\Gamma(0,0,0)$ point in reciprocal space, though somewhat larger, resemble to a large extent the hole sheets of the $H(1,0,0)$ point in the paramagnetic phase. He pointed out that by a shift over $(0.96,0,0)$ the former coincide (nest) fairly well with the latter. He used this nesting and the coupling between the corresponding states to explain the observed incommensurate SDW. Fedders and Martin⁹ worked out this coupling in a two-band model which indeed predicts a phase transition to a SDW ground state. The interaction between the two states is provided by the Coulomb attraction between the electrons and the holes. The nesting seems to be the best for $(\alpha,\delta,0)$ or $(\alpha,0,\delta)$, where $\delta \neq 0$, i.e. at points some what away from the octahedron vertices.

4.2.3. Density of states

Besides the properties of the electron band structure discussed above, one can expect effects on the density of states (DOS) due to the additional wave vector of the crystal. If the SDW would be perfectly antiferromagnetic, the states at $\mathbf{Q}' = (\frac{1}{2}, 0, 0)$ and $-\mathbf{Q}'$ would interact, resulting in a gap halfway the Brillouin zone, in the direction of \mathbf{Q} . The consequence would be a doubling of the (magnetic) unit cell; the bands being folded back into the new Brillouin zone. In the case of an incommensurate wave, these gaps also open, but now at a general point in the Brillouin zone. Strictly spoken, the resulting crystal has lost its translational symmetry in the (1,0,0)-direction. This symmetry can, however, be restored, by using the forementioned superspace description. The mixing of states resulting in gaps, happens for wave vectors given by $\mathbf{k} = \pm N\mathbf{Q} \pm \mathbf{K}$, where $\mathbf{K} \in \Lambda^*$ and N integer; the gaps, however, becoming smaller for larger values of N . The resulting band structure shows an infinite number of gaps throughout the energy scale. Such a band structure was studied by de Lange *et al.*¹⁰ in a one-dimensional modulated Kronig-Penney model.

The higher order gaps become more important when higher harmonics of \mathbf{Q} play a more important role in the modulation. In chromium Pynn *et al.*¹¹ have found second and third harmonics in the SDW. The contribution of the second harmonic increases with decreasing temperature, while that of the third harmonic starts to saturate at 220 K. Hence, effects due to the higher order gaps can be expected to become more appreciable for low temperatures.

4.3. Point-contact spectroscopy

Point-contact spectroscopy (PCS) is a technique which has been proven to be very useful for studying the effects of excitations and their scattering processes with electrons.¹² For this purpose a very sharp point of one metal (or alloy) is brought into contact with another metal and the first or second derivative of the current through the contact with respect to the voltage across the contact is measured as a function of that voltage. The linear contact dimension is assumed to be small compared to the mean free path of the electrons. Therefore the transport through the contact is ballistic. Typical contact resistances are 0.1 - 10 Ω and voltages are

0 - 50 mV. For normal metals a constant density of states for the electrons can be assumed if one takes into account that the energies corresponding to the applied voltages are much smaller than the Fermi energy. If electron phonon scattering is dominant, the resulting spectra show an increase of resistance with voltage due to the back flow of electrons through the orifice, being scattered by acoustical phonons. The resistance shows large increases when the phonon density of states has a singularity, for instance for energies of states at the Brillouin zone boundary (Debye energy).

In our case, the technique is used to observe changes in the electron density of states. The singular effects of phonons can be neglected as long as we stay far away from the Debye energy, which is for chromium 38 meV for the longitudinal acoustical phonons and approximately 32 meV for the transverse acoustical phonons.¹³ We implicitly exclude effects due to gaps in the phonon density of states which result from a small induced modulation of the lattice, characterised by a wave vector $\mathbf{k} = 2\mathbf{Q}$. A comparable use of PCS has been made by Moser *et al.*¹⁴ to observe anomalies in the electron DOS in CePd₃ and related compounds. For our purpose it is sufficient to concentrate on the first order derivative $\partial V/\partial I$ as a function of the voltage V .

We will illustrate the effect of the SDW on the $\partial V/\partial I$ -spectrum in chromium by assuming that the electron band properties of the basic structure (no modulation) resemble those of the free electron gas. The effects of the additional wave vector of the SDW as given by \mathbf{Q} is to open gaps whenever two surfaces of constant energy in \mathbf{k} -space (spheres in our approximation) at $\mathbf{k} = \pm\mathbf{Q} \pm \mathbf{K}$, where $\mathbf{K} \in \Lambda^*$, cross each other. This can be understood if we use the full symmetry of the crystal as provided by the superspace description, where the reciprocal lattice vectors are labeled by four integers (h, k, l, m) . This 4D-vector corresponds in three dimensions to the vector $h\mathbf{a}^* + k\mathbf{b}^* + l\mathbf{c}^* + m\mathbf{Q}$. As the basic reciprocal lattice vectors ($m = 0$) are concerned, we can neglect the effect of the energy shift on the Fermi level, due to the voltage across the contact; the Fermi level is raised but the metal-like band structure is considered to be constant for the voltages applied. The wave vector \mathbf{Q} however, provides for gaps in the neighbourhood of or even centered on the Fermi level. Therefore, these gaps can be crossed by applying relatively small voltages. Moreover, as will be shown hereafter, all additional gaps below the Fermi-level contribute to the increment of the resistance. The above mentioned illustration will therefore be given for free electron energy levels, whose spheres do not touch the Brillouin zone boundary of the basic structure ($m = 0$), but do cross the

corresponding boundary in superspace. This is possible because h and m can be chosen as to result in a very small wave vector as compared to, say, $(1,0,0) \in \Lambda_3^*$. The crossing of the energy bands results in orbits that open and close as a function of the energy, as can be seen schematically in Fig. 4.1. The directions in \mathbf{k} -space, perpendicular to \mathbf{Q} , are in our approximation independent of the modulation. Therefore, one can use for example the results of the one-dimensional Kronig-Penney model of de Lange *et al.*¹⁰ for the band structure along the direction of \mathbf{Q} .

The contributions of the forementioned orbits to the current through the contact is calculated as follows. Because the linear dimensions (b) of the orifice of the contact are small compared to the mean free path (ℓ) of the electrons, $b \ll \ell$, the corresponding, so-called Sharvin current through the orifice is determined by the ballistic transport of electrons from the metal with the higher (V) potential, to the other metal.

$$J_{\text{SH}} = \frac{2e}{(2\pi)^3} \int_{\text{orifice}} d^2r \int' d^3k v_n f^\circ(\mathbf{r}, \mathbf{k}), \quad (4-1)$$

where v_n is the component of the electron velocity perpendicular to the orifice, f° is the electron distribution function and e is the electron charge. The integration in \mathbf{k} -space involves all \mathbf{k} -vectors that can contribute to the current, for which v_n is positive and the corresponding energy lies between ϵ_F and $\epsilon_F + eV$. These restrictions are denoted as a prime at the integral. At zero temperature this can be written as

$$J_{\text{SH}} = \frac{2e}{(2\pi)^3} (\pi b^2) \frac{1}{\hbar} \int' d^3k \frac{\partial \epsilon(\mathbf{k})}{\partial k_n}, \quad (4-2)$$

where we have assumed a circular orifice with radius b . $\epsilon(\mathbf{k})$ is the energy of the electron. For the unperturbed free electron gas (FEG) we have $\epsilon(\mathbf{k}) = \hbar^2 k^2 / 2m$, thus finding

$$J_{\text{SH}}^{\text{FEG}} = \frac{2e}{(2\pi)^3} (\pi b^2) \frac{2\pi m}{\hbar^3} \epsilon_F \int_{\epsilon_F}^{\epsilon_F + eV} d\epsilon = \frac{e^2 b^2}{2\pi} \frac{m}{\hbar^3} \epsilon_F V, \quad (4-3)$$

if we assume for the Fermi energy that $\epsilon_F \gg eV$. (For normal metals $eV/\epsilon_F \approx 10^{-3} - 10^{-4}$). The resistance is therefore independent of the energy of the electrons, resulting in a linear relation between the current and voltage. When we introduce the modulation to the problem, the factor ϵ in the integrand of (2) in general is no longer a continuous function of k_n , due to the additional gaps in the

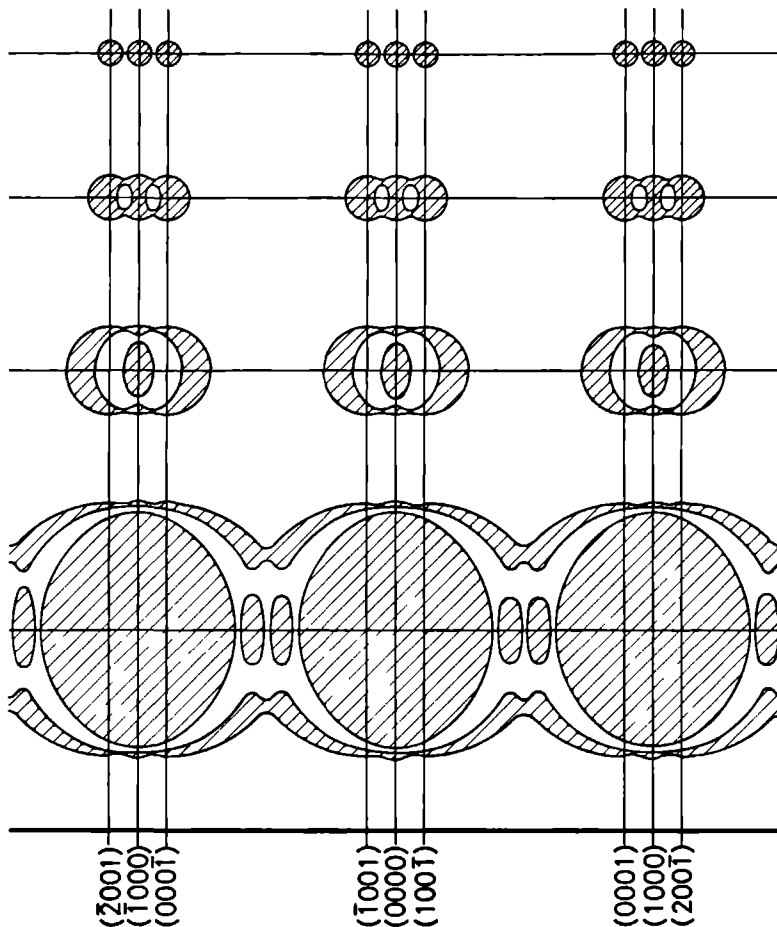


Figure 4.1 Schematic drawing of open and closed orbits on surfaces of constant energy for four different values. Each surface is drawn as a projection from 4-dimensional superspace in the (a^*, b^*) -plane in an extended zone scheme. Note that the directions along b^* and c^* are free-electron-like. The lattice vectors in reciprocal space are denoted by (h, k, l, m) . For the sake of clarity only the first order gaps are given. Shaded areas represent occupied surfaces. Each of the four energies lies in a different band within the conduction band.

spectrum; to the current (cf. the normal energy bands in a crystal field). Thus equation (4-2) becomes

$$J_{SH} = \frac{2e}{(2\pi)^3} (\pi b^2) \frac{1}{\hbar} \sum_s \int d^3k \frac{\partial \epsilon_s(\mathbf{k})}{\partial k_n} \quad (4-4)$$

If we replace the integral in \mathbf{k} -space by an integral over the energy, we find

$$J_{SH} = \frac{2e}{(2\pi)^3} (\pi b^2) \frac{1}{\hbar^2} \sum_s \int d\epsilon_s \int dS_{\mathbf{k}} (\mathbf{n}_{\mathbf{k}} \cdot \mathbf{s}_{\mathbf{k}}), \quad (4-5)$$

where $\mathbf{n}_{\mathbf{k}}$ is a unit vector in the direction of the velocity of the electron and $\mathbf{s}_{\mathbf{k}}$ is a unit vector perpendicular to the orifice. $S_{\mathbf{k}}$ is a surface of constant energy in \mathbf{k} -space. From (4-5) we conclude that for every energy ϵ_s the projection of the corresponding surface in \mathbf{k} -space on the plane of the contact determines the Sharvin current. We will distinguish between two different cases for which the orifice normal is either parallel or perpendicular to \mathbf{Q} . In the former case we need the projection along k_x , while in the latter situation the projection along k_z (or k_y) should be used. Fig. 4.1 can be an aid for a visualisation. As the exact band structure of chromium is too complicated, we will continue our simplification by splitting the energy in a part that depends on \mathbf{k} -vectors perpendicular to \mathbf{Q} and one depending on \mathbf{k} -vectors parallel to \mathbf{Q} :

$$\epsilon(\mathbf{k}) = \epsilon_{\perp}(k_y, k_z) + \epsilon_{\parallel}(k_x), \quad (4-6)$$

where $\epsilon_{\perp} = \frac{\hbar^2}{2m}(k_y^2 + k_z^2)$ and $\epsilon_{\parallel}(k_x)$ depends on the actual modulation amplitude. Then equation (4-4) reduces to

$$J_{SH}^{\parallel} = \frac{2e}{(2\pi)^3} \frac{(\pi b)^2}{\hbar^3} \sum_s \int_{\epsilon = \epsilon_{\perp} + \epsilon_{\parallel}} \int d\epsilon_{\perp} \int d\epsilon_{\parallel/s} \quad (4-7)$$

The summation over s involves all bands between $\epsilon = \epsilon_F$ and $\epsilon = \epsilon_F + eV$. In Fig. 4-2 the area, relevant for the integrals is shaded. Using this figure, we find

$$J_{SH}^{\parallel} = \frac{e^2 b^2}{2\pi} \frac{m}{\hbar^3} v \sum_s \int d\epsilon_{\parallel/s} \quad (4-8)$$

Analogously, we find for the current when the orifice normal (say \mathbf{z}) is

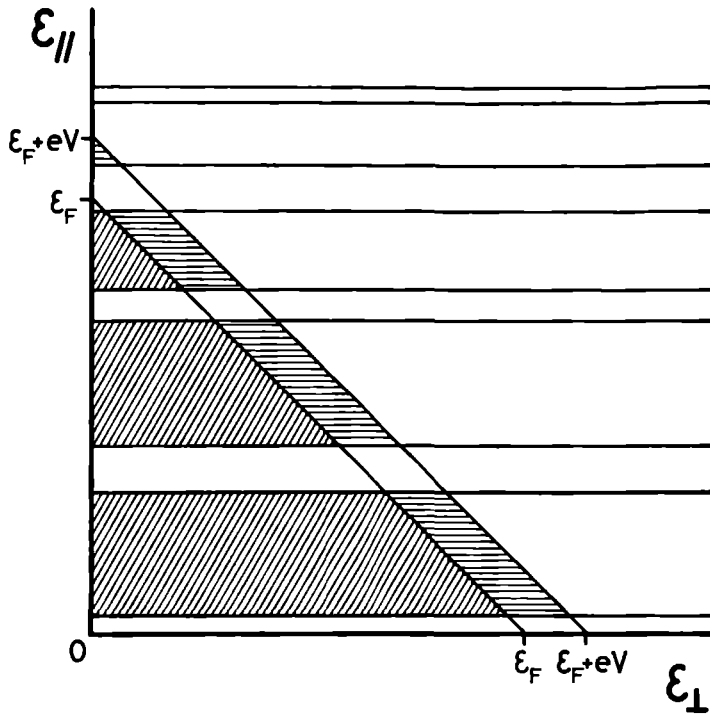


Figure 4.2. Schematic drawing of the surface of constant energy as a function of the applied voltage in energy space. Note that $\epsilon = \epsilon_{\perp} + \epsilon_{\parallel}$. For directions parallel to \mathbf{Q} the energy bands (shaded areas indicate filled bands) are present, while in the perpendicular direction the electrons are assumed to be free

perpendicular to \mathbf{Q}

$$J_{\text{SH}}^{\perp} = \frac{e^2 b^2}{2\pi} \frac{1}{\pi \hbar} \left\{ \frac{2m}{\hbar^2} \epsilon_F \right\}^{1/2} V \sum_s \int d k_{xs}, \quad (4-9)$$

where we have used $\epsilon_z = \hbar^2 k_z^2 / 2m$. From the last two equations we conclude that whenever $\epsilon(V)$ crosses a gap, the Sharvin resistance stays constant. Between two gaps, the conductivity increases linearly for a contact with its normal parallel to \mathbf{Q} , while for the case perpendicular to \mathbf{Q} , the band structure at the edges determines the conductivity. This result is schematically drawn in Fig. 4.3.

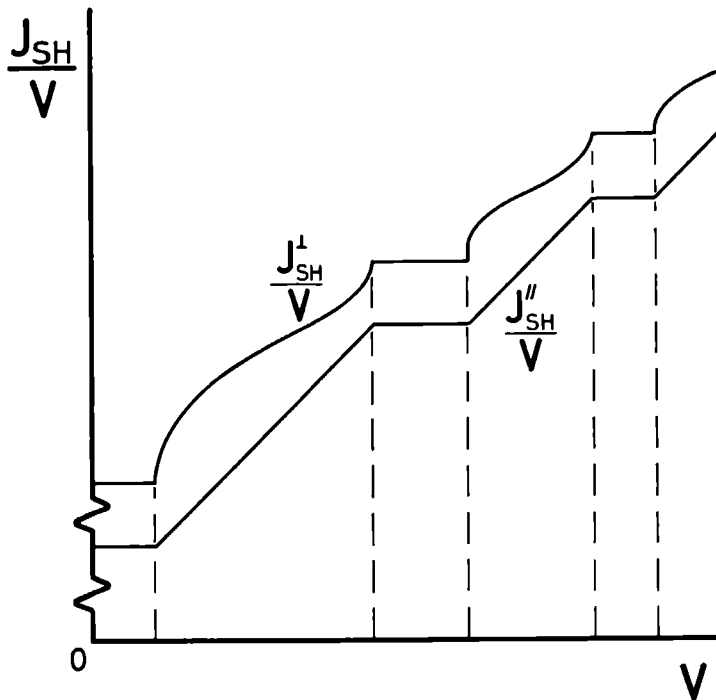


Figure 4.3. The Sharvin conductivity, schematically, as a function of the applied voltage for point-contacts parallel and perpendicular to Q . The constant regions in J_{SH}/V represent the gaps. It should be noted that for normal applied voltages only one gap is traversed.

An important result is that the structure due to the gaps, in the $\partial V/\partial I$ -spectra is roughly the same for all orientations of the point-contact.

Up to now, only the gaps at $\mathbf{k} = \pm N\mathbf{Q} \pm \mathbf{K}$ with $N = 1$ have been considered. Higher harmonics of Q can (and in chromium do¹¹) play a role, the corresponding gaps being smaller. The effect of these higher order gaps on the Sharvin resistance is analogous to what was described for the first order gaps. At this point it is worthwhile to make an estimation of the size of the change in the Sharvin current due to these gaps. An essential difference between chromium and a normal metal is

the contribution of all gaps between occupied bands s (see Fig. 4.2) decreasing the current in chromium. The Fermi-energy in antiferromagnetic chromium is approximately 7 eV according to the band structure calculations of Asano and Yamashita.¹⁵ The first order gap in the neighbourhood of the Fermi-level is of the order of 100 meV. Therefore, this single gap already causes a 1.4 % decrease of the current for contact normals parallel to Q , at least in our model. If we also take into account the effect of the other gaps in the conduction band (see de Lange and Janssen¹⁰) we can expect larger decreases of the current.

4.4. Experimental

A single crystal of chromium was obtained from a Czochralski growth. The resulting crystal ($\approx 7 \times 7 \times 4$ mm³) was oriented by means of X-rays and spark cut, to obtain specimens with faces perpendicular to the cubic axes. The crystals were then etched electro chemically. At first, point-contacts were made between these samples using the Kharkow configuration, for which two fairly sharp edges of the samples are gently pressed against each other. In later experiments these samples were forced to single- Q domains by applying a magnetic field of 8 T above the Néel temperature and thus slowly cooling down (0.5-1 K/minute) to room temperature. Afterwards they were immediately cooled down to 4.2 K in a He-bath cryostat. A third series of measurements was performed by placing a sharp etched tungsten needle on a chromium bulk sample which was also magnetically oriented as described above. All measurements were performed at 4.2 K or lower, down to 1.2 K. First derivatives $\partial V/\partial I$ versus V were measured with a four contact configuration in a compensating resistance bridge, using lock-in techniques.

4.5. Results and Discussion

All measurements showed an anomalous behaviour around zero bias voltage. For normal pure metals, the first derivative $\partial V/\partial I$ shows a minimum for zero bias voltage. The signal becomes bigger for higher voltage mainly due to electrons which, after being scattered by phonons, reenter the orifice, thus increasing the

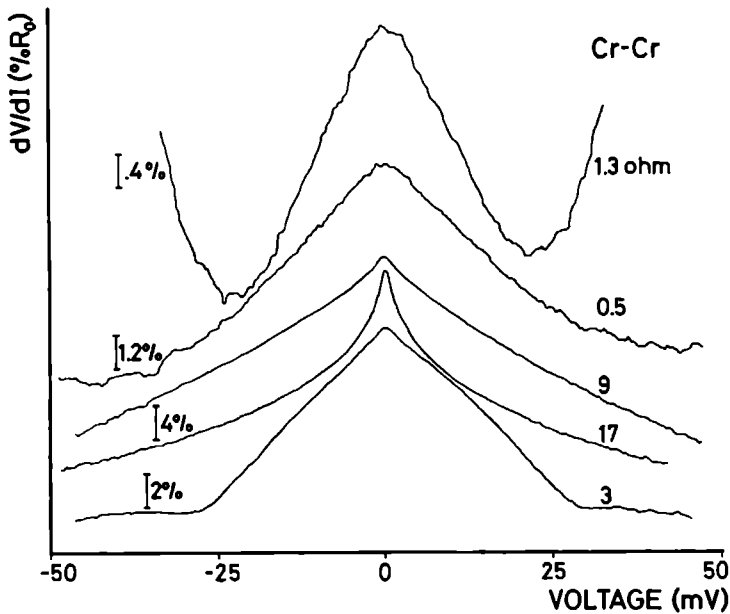


Figure 4.4. Some typical point-contact spectra for different Cr-Cr point-contacts. The percentages indicate the vertical scale with respect to the zero-bias resistance.

resistance. A comparable behaviour is observed in chromium, although a broad symmetric peak around zero indicates an additional increase of the resistivity for low voltages. The shape and height of this anomaly differs for different point-contacts. In Fig. 4.4 some shapes are given for several point-contacts. As can be seen in this figure, the fraction of the differential resistance of the anomaly, as compared to the zero bias point-contact resistance, varies from approximately 3 % to more than 25 %. The voltage for which an increasing resistivity becomes the main feature varies from 20 mV to approximately 100 mV, with a tendency for high-resistance point-contacts to start increasing at higher voltages. In order to find out whether this zero bias anomaly depends on the orientation of the modulation wave vector

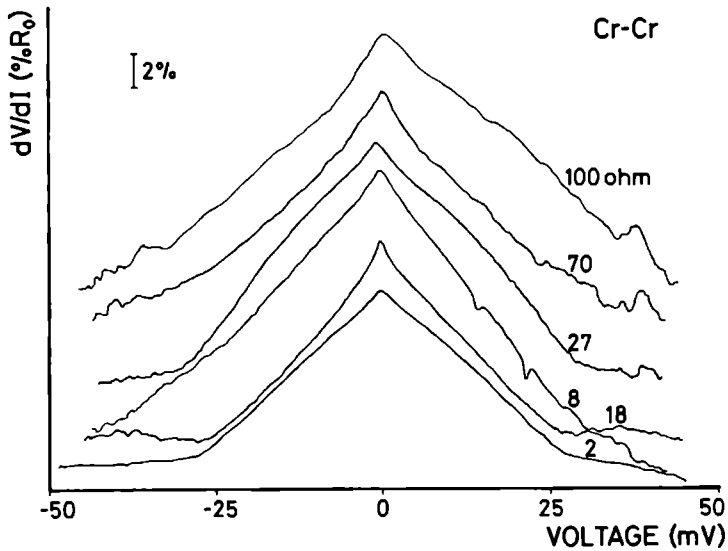


Figure 4.5. The zero-bias anomaly for one and the same contact but different zero-bias resistances.

with respect to the current through the contact, we measured the spectrum for samples which were oriented in a magnetic field of 8 T, either with Q parallel or with Q perpendicular to the point-contact. Experimentally there was no significant difference in spectra between these two conditions. This result did not change for a similar experiment using a tungsten spear on a chromium bulk sample. The latter configuration is expected to provide a more reliable orientation of the point-contact with respect to the crystal. Once a sample was magnetised, several point-contacts with the same orientation of the crystals, generally showed comparable peak shapes and heights.

For point-contacts, which allowed for high resistance contacts, it was possible to measure the resistance dependence of the anomaly height. A result of such a measurement is given in Fig. 4.5. This figure shows that the height of the anomaly is independent of the point-contact resistance over more than one decade, and

moreover, that the shape does not change for one and the same point-contact. From this result we can conclude that the size of the effect is linear in the contact resistance.

There was no observable temperature dependence of the anomaly between 4.2 K and 1.2 K.

Any dependence of the spectrum on magnetic field was not observable up to 15 T, neither for fields parallel to Q nor for perpendicular fields. The measurements using the tungsten spear turned out to be very sensitive to high magnetic fields, for which the noise increased drastically. This latter effect is probably due to magneto-mechanical effects.

Before explaining the observed zero bias anomaly in terms of the density of states for the electrons, changing the Sharvin current through the contact, we first will exclude an explanation in terms of heating effects. Heating is known to be often the cause of observed structure in point-contact spectra.¹⁶ The first derivative $\partial V/\partial I$ as a function of voltage then more or less resembles the bulk resistivity as a function of temperature $\rho(T)$. The link between temperature and voltage is achieved by Joule-heating effects, which have only appreciable contributions in the so-called dirty limit (thermal regime), for which both the mean free path of the electrons and the inelastic diffusion length are smaller than the linear contact dimension. These thermal effects can be disregarded in chromium for two reasons. First of all, the dirty limit is in pure metals normally met for high (>100 meV) voltages and secondly, the resistivity in chromium shows a normal metal-like (decreasing) behaviour at low temperatures, albeit that the antiferromagnetic part of the resistivity increases with decreasing temperature.¹⁷ Our results for low voltages, when interpreted as due to thermal effects, would suggest an increase of the resistivity at low temperatures. Therefore, heating effects can be disregarded.

An explanation based on the electronic density of states near the Fermi level is, given the results of section 4.3, appealing. The actual form of this function, however, is not very well known, surely, if one takes into account the influence of the modulation wave. Some remarks, though, can be made. First of all, the height of the anomaly is at most approximately 25 % of the zero-bias resistance. For a triangular shape this means a 13 % drop in the resistance. This is ten times as large as the value expected due to the single first order gap and is a measure for the effect of all additional gaps. Moreover, the possibility of obtaining such high-resistances as 100Ω with a stable contact, indicates also the intrinsic properties of chromium as compared to normal pure metals.

The sizes of the different gaps are too small to be predicted by band structure calculations. Experimental techniques as XPS and soft X-ray absorption, used to reveal the band structure, are not adequate for determining the low-energy effects which are relevant here. However, experiments, sensitive in the low-energy regime of the conduction electrons have been performed. These are infrared reflectance and inelastic neutron scattering measurements. The values for the energy gap reported by several authors varies considerably. We will first give an overview of the results reported and afterwards compare them with our measurements.

As the infrared reflectance experiments are concerned, Barker and Ditzenberger³ found an energy gap of 1000 cm^{-1} (124 meV) at 80 K. The same value was found by Lind and Stanford⁴ (30 K). These latter authors found an additional peak at 0.45 eV, which disappeared above T_N . Kirillova and Nomerovannaya⁵ found a value of 0.112 eV at 100 K. For all these measurements, the low-energy side of the spectrum was limited to approximately 60 meV. Inelastic neutron scattering experiments range to lower energy transfers. Using this technique, Ziebeck and Booth¹⁸ found a gap of 16.9 meV at 295 K. They used energy transfers up to 74 meV. The extrapolated value at 0 K, using a BCS-like temperature dependence of the gap, then yields 71 meV. This result is in agreement with that obtained by Moyer *et al.*¹⁹ who fitted magnetic susceptibility data to a theoretical model, thus finding 28 meV for the gap. Barker and Ditzenberger suggest that their result of 124 meV is a measure of the first order gap due to the SDW. Higher order gaps are expected to lie at lower energies. An important question for the interpretation of our results is which gaps enclose the Fermi level. For infrared reflectance measurements the effect of a gap, enclosed by or above the Fermi level, is seen as an absorption of radiation for energies higher than the gap, irrespective of its exact position. The only restrictions imposed are that the transition between the bands obeys momentum conservation and that the corresponding transition matrix element is not zero. In an incommensurate structure the equivalence between states at $\mathbf{k} = 0$ and $\mathbf{k} = \pm N\mathbf{Q}$ (N integer), allows for transitions from \mathbf{k} to $\mathbf{k} \pm N\mathbf{Q} \pm \mathbf{K}$. This additional transition scheme was used by Lind and Stanford to account for the absorption peak at 0.45 eV. In their explanation, both gaps (0.124 meV and 0.45 meV) are first order gaps corresponding to wave vectors \mathbf{Q} and $2\mathbf{a}^* - \mathbf{Q}$ respectively. They used band structure calculations of Asano and Yamashita,¹⁵ who also discussed the gap structure. The Fermi level lies in the low-energy first order gap. Addition of small amounts (<1 %) of Mn increases the value of \mathbf{Q} . The effect on the reflectivity is to

decrease the 0.1 eV absorption peak and increasing the peak at 0.4 eV. For higher percentages Mn, the SDW becomes commensurate and the two first order gaps merge to one gap at approximately 0.4 eV, as discussed by Bos and Lynch.²⁰ Second order gaps in the neighbourhood of the Fermi level are expected to occur on both sides of the first order gaps for a metal-like band and small first order gaps. On the other hand, it is possible that the second order gap lies inside the first order gap for a large enough value of that first order gap, resulting in an open orbit within the first order gap. In this latter case it is possible to find gaps at lower energies than that of the first order gap. This can account for the lower extrapolated value of 71 meV found by Ziebeck and Booth, although these authors interpret their result in terms of the first order gap.

As the aim of our measurements was to find gaps at lower energies (see Fig. 4.4), we also measured the far infrared reflectivity of our crystal in a non-single Q-state in the energy range 6.2 -37 meV at room temperature and at 30 K. We found no structure at all, probably because the instrument limited the sensitivity to approximately 1 %. For comparison, the first order gap at 124 meV generally causes a dip of 3 % in the reflectivity.³ Our instrumental resolution probably is too small to observe second order gaps because the corresponding transition probabilities are expected to be considerably smaller. A transition is allowed in principle, at least.

As the insensitivity of the anomaly to the direction of the point-contact with respect to the modulation wave vector is concerned, we have to distinguish between two possibilities. The first one is a direct consequence of the results of section 4.3. As already discussed, the difference in spectra for parallel and perpendicular currents is only due to the structure in the density of states near the band edges corresponding to the additional gaps (see Fig. 4.3). The other possible reason stems from the polarised reflectance measurements of Barker and Ditzenburger.³ These authors used single Q-state crystals (oriented in 2.5 T, resulting in 10-20 % higher bulk conductivity for directions perpendicular to Q) and found no difference in reflectivity for polarisations parallel or perpendicular to Q. They conclude that, given the infrared skin-depth, the modulation wave vector in at least the first 200 Å near the surface, lies in the surface. A magnetic field of 2.5 T would not be strong enough to change the direction of Q near the surface, due to the intrinsic defect of any surface, pinning the modulation wave. Although their conclusion is not unambiguous, the results clearly show a preference for the wave vector to have a fixed orientation with respect to the surface. Therefore, the point-contact spectra,

which measure the effect of the modulation over a distance of the mean free path of the electrons from the surface, are expected to show no appreciable dependence on the bulk orientation of \mathbf{Q} . Whether, despite the magnetic alignment procedure, our measurements involve only contact normals parallel or perpendicular to \mathbf{Q} is still an open question for us. Moreover, misalignment of the point-contact with respect to the surface normal can also account for differences in spectra of several contacts. And as was mentioned before, the first reason mentioned above, namely the results (4-8) and (4-9) of section 4.3, suggest already a small difference for currents parallel or perpendicular to \mathbf{Q} .

This brings us to the question why the zero bias anomaly manifests its minimum at different voltages for different contacts. To answer this question we have to distinguish between three different contributions to the Sharvin resistance of the contact: the gap structure in the density of states, the scattering by phonons and Joule-heating. The first reason has already been discussed in detail.

The increase of the resistance for higher voltages due to scattering by phonons normally is of the order of few percent of the zero bias resistance and is limited by the Debye energy. The increase of the resistance in our measurements, however, always continues up to voltages well above the Debye energy. (32 meV for the transverse acoustical phonons, which provide the main contribution to the scattering process). Furthermore, the increment in resistance is often far too big to be accounted for by phonon scattering only.

Heating effects, on the other hand, are more probable. As mentioned before, such effects normally occur in pure metals for voltages of the order of 100 meV. The size of the effect is expected to increase with decreasing point-contact resistance. This actually is what we on the average observe. Typical low-resistance point-contacts ($R_0 \leq 1 \Omega$) have spectra that increase already at 20-40 meV, while contacts with a relatively large resistance ($R_0 \geq 5 \Omega$) have a zero bias anomaly continuing up to maximal 110 meV. This latter category of contacts either shows an increase of resistance for higher voltages or even tends to saturate (see e.g. the 3 Ω -spectrum in Fig. 4.4). There are a few exceptions to this behaviour (see e.g. the 0.5 Ω -spectrum in Fig. 4.4, which does not increase until approximately 40 meV) but this abnormal behaviour can be attributed to the actual point-contact with all its unknown incidental peculiarities. In any way, the increasing resistance seemingly depends more on the point-contact itself, rather than on the structure of chromium.

The fact that for energies still inside the gap, the Sharvin current increases with increasing voltage, indicates that our model is too crude to predict the exact shape of the spectra. In particular, the assumption that the dispersion relations in mutually perpendicular directions are independent of each other, appears to be non-realistic. We expect for the gaps a k_y and k_z dependence too which, moreover, diminishes on approaching the gap edges. This can account for the decreasing resistance for increasing applied voltage.

4.6. Conclusion

In conclusion, we can say that in our Cr-Cr point-contact spectra, the zero bias anomaly is a measure for the gaps in the density of states due to the modulation wave, which, depending on the point-contact resistance, is diminished by heating effects, causing an increase of the resistance. The origin of the anomaly is probably mainly due to the first order gap, because the maximal voltage for which the anomaly is observed is approximately 110 meV, in fair agreement with the results obtained by infrared spectroscopy and inelastic neutron scattering. The actual form of the anomaly, triangle-shaped, rounded or even with a sharp cusp at zero bias voltage, probably depends on the orientation of the point-contact with respect to the surface of the crystal (and correspondingly to the modulation wave vector \mathbf{Q}). The effect of gaps lying at lower energies is intrinsically present, because the effect of the single first order gap is relatively big compared to the zero-bias resistance, which can become unusually high in the case of chromium. The actual shape of the anomaly can not be explained within our simple model. A more realistic approach for which e.g. the dependence of the gap structure on k_y and k_z is also taken into account, is required. The results as given in Fig. 4.5, where heating effects are not yet dominant, indicate that the height of the anomaly depends linearly on the resistance. This is in agreement with (4-8) and (4-9), the Sharvin resistance being inversely proportional to area of the point-contact orifice.

Acknowledgements

We gratefully acknowledge Prof. R. Griessen who provided the single crystal and the stimulating discussions with Dr. A.P. van Gelder. This work is part of the research program of the Stichting voor Fundamenteel Onderzoek der Materie (Foundation for Fundamental Research on Matter) and was made possible by financial support from the Nederlandse Organisatie voor Zuiver-Wetenschappelijk Onderzoek (Netherlands Organisation for the Advancement of Pure Research).

References

1. For a review see A. Arrott and S.A. Werner in *Magnetic and Inelastic Scattering of Neutrons*, ed. T.J. Rowland and P.A. Beck (Gordon & Breach, New York, 1968).
2. A.J. Arko, J.A. Marcus and W.A. Reed, *Phys. Letters* **23**, 617 (1966).
3. A.S. Barker and J.A. Ditzenberger, *Phys. Rev. B* **1**, 4378 (1970).
4. M.A. Lind and J.L. Stanford, *Phys. Letters* **39A**, 5 (1972).
5. N.M. Kirillova and L.V. Nomerovannaya, *Fiz. metal. metalloved.* **40**, 983 (1975).
6. Y. Tsunoda, M. Mori, N. Kunitomi, Y. Teraoka and J. Kanamori, *Solid State Comm.* **14**, 287 (1974).
7. A. Janner and T. Janssen, *Acta Cryst.* **A36**, 399 (1980).
8. W.M. Lomer, *Proc. Phys. Soc.* **80**, 489 (1962).
9. P.A. Fedders and P.C. Martin, *Phys. Rev.* **143**, 245 (1966).
10. C. de Lange and T. Janssen, *Phys. Rev. B* **28**, 195 (1983).
11. R. Pynn, W. Press, S.M. Shapiro and S.A. Werner, *Phys. Rev. B* **13**, 295 (1976).
12. A.G.M. Jansen, A.P. van Gelder and P. Wyder, *J. Phys. C: Solid State Phys.* **13**, 6073 (1980).
13. W.M. Shaw and L.D. Muhlestein, *Phys. Rev. B* **4**, 969 (1971).
14. M. Moser, F. Hulliger and P. Wachter, *Physica* **130B**, 21 (1985).
15. S. Asano and J. Yamashita, *J. Phys. Soc. Japan* **23**, 714 (1967).
16. I.K. Yanson, O.I. Shklyarevskii, *Fiz. Nizk. Temp.* **12**, 899 (1986) [*Sov. J. Low Temp. Phys.* **12**, 509 (1986)].
17. D.B. Mcwhan and T.M. Rice, *Phys. Rev. Letters* **19**, 846 (1967).
18. K.R.A. Ziebeck and J.G. Booth, *J. Phys. F: metal phys.* **9**, 2423 (1979).
19. C.A. Moyer, S. Aarjans and L. Hedman, *Phys. Rev. B* **14**, 1233 (1976).
20. W. Bos and D.W. Lynch, *Phys. Rev. B* **2**, 4567 (1970).

Summary

This thesis treats a number of experiments performed on modulated crystals, both commensurate and incommensurate. The results of these experiments are analysed, taking into account the superspace group symmetry of the structures.

In a modulated crystal the periodic pattern, which is characteristic for normal crystals, is disturbed. Nevertheless, they form structures which can be described in terms of the periodic variations of a given basic crystal. The unit cell is then generally enlarged due to that modulation. For commensurate modulation waves the translational symmetry is not lost but simply modified. The space group of such a crystal is in general different from that of the basic structure but still adequate for describing the (changed) physical properties. Well-known examples are (anti)ferroelectric crystal phases and ordered magnetic structures, when compared with their high-temperature phase.

Incommensurate structures, on the other hand, are characterised by additional periodicities which do not fit with the three basic ones of the underlying lattice. The result is that the lattice translational symmetry of the crystal along the direction of the modulation is lost and therefore, no space group symmetry is present. Consequently, the physical properties of an incommensurate crystal lose a very important mathematical characterisation and accordingly, their theoretical foundation. Nevertheless, many of these properties, such as the X-ray diffraction pattern and the morphology, have an appearance which actually indicates a long range crystalline order and the presence of a large degree of symmetry. This fact was taken into account by the introduction of so-called superspace groups to describe the symmetry of incommensurate phases. The essence of the superspace description is to treat the phase of the modulation waves as additional coordinates in a higher $(3 + d)$ -dimensional space. In case of a single modulation, one has $d = 1$. In this superspace the lattice translational symmetry is restored and one can even define again rotational and mirror operations. Thus, one gets $(3 + d)$ -dimensional space groups (so-called superspace groups) that characterise the symmetry of the modulated crystal. These groups turned out to be very useful for analysing the X-ray diffraction pattern of incommensurate crystals, and therefore, were capable of describing complex structural relations in such crystals very efficiently.

The success of the use of superspace groups in the determination of the structure of incommensurate crystals was an impulse for studying theoretically and experimentally the consequences of that symmetry for other physical properties.

This thesis, also, is a result of that impulse. It is divided in three chapters, where different physical properties concerning optical and dynamical aspects of modulated crystals are studied.

In chapter 2 the vibrational spectra are investigated by Raman and far-infrared spectroscopy. Both these techniques allow for measuring the long-wavelength ($\mathbf{k} = 0$) optical phonons of crystals. Due to the modulation characterised by a wave vector $\mathbf{k} = \mathbf{q}$, also the phonon-modes at $\mathbf{k} = n\mathbf{q}$, with n integer, can become active in the Raman or infrared spectra. These additional modes are studied both in commensurate and incommensurate phases, in two dielectric compounds namely Na_2CO_3 and $[\text{N}(\text{CH}_3)_4]_2\text{ZnCl}_4$.

In the case of Na_2CO_3 the complete Raman spectrum in the β , γ and δ -phase have been measured, as well as the far-infrared spectrum in the γ and δ -phase. These spectra are interpreted using both symmetry and phenomenological arguments. For the incommensurate γ -phase, the superspace group symmetry is used. In this latter phase additional modes are observed and interpreted. Furthermore, two soft modes have been found, one of which belongs to the monoclinic (β) to incommensurate (γ) phase transition and represents a so-called amplitudon. Finally, it is shown that the spectra of the δ -phase indicate the existence of a low-temperature commensurate (lock-in) phase.

A generalisation of the use of superspace groups to commensurate phases is examined in the case of $[\text{N}(\text{CH}_3)_4]_2\text{ZnCl}_4$. This compound has, as many other isomorphic members of the A_2BX_4 -family of dielectrics, besides an incommensurate phase, many commensurate phases for different temperatures. For some of these commensurate structures, the superspace group symmetry of the incommensurate phase is conserved to a very good approximation. The question arises whether that is reflected in the physical properties. In particular it is studied, whether this conservation also holds for the selection rules or intensities. Furthermore, the domains in the monoclinic commensurate phases are studied in more detail. The large rotations of the optical indicatrix in these phases are discussed in connection with the orthorhombic superspace group symmetry.

Chapter 3 treats the classical optical activity in the compound Rb_2ZnBr_4 . In contrast to the optical activity of chapter 2, here the gyration is meant, an effect for which the polarisation of light which passes the crystal is rotated around the direction of propagation. For the commensurate phases, the normal space groups are adequate for predicting the observed effects in Rb_2ZnBr_4 , while for the incommensurate phase the superspace group symmetry is needed. We present a

phenomenological theory for both the dielectric and the gyration properties in the incommensurate phase. In order to allow for long-wavelength structural properties, which are typical for incommensurate phases, to be reflected in the dielectric and gyration response, we write the corresponding tensors in a Fourier decomposition. The allowed components of the Fourier tensors and their symmetry are found with the help of the superspace group. In the case of the dielectric response the electric fields are determined in an approximation involving two Fourier components beside the macroscopic one. For the gyration effect, the form of the tensors is used to predict the conditions for the occurrence. The experimental results indicate which of the Fourier components are possibly the relevant ones.

In chapter 4, a study of the incommensurate spin density wave in chromium by means of point-contact spectroscopy is presented. We show that the current-voltage characteristics of a very small constriction (with a diameter of a few hundred angström, thus smaller than the mean free path of the electrons) between two metals is changed by small gaps in the density of states of the electrons in the neighbourhood of the Fermi energy. The origin of these new gaps at $2k = nq$ (n integer) lies again in the additional periodicity of the spin density wave. Their influence is here taken into account within the free electron approximation. The result is used to account for the experimentally observed decrease of the resistance with increasing voltage of a Cr-Cr point-contact for low applied voltages. The increasing resistance for higher voltages (≥ 50 meV) is interpreted as due to heating effects. The size of the observed gap (≈ 110 meV) is compared with results of other experiments.

Samenvatting

In dit proefschrift worden een aantal experimenten aan zowel commensurabel als incommensurabel gemoduleerde kristallen beschreven. De resultaten zijn geanalyseerd, rekening houdend met de superruimte-symmetrie van de betreffende structuren.

In een gemoduleerd kristal is het voor normale kristallen karakteristieke periodieke patroon verstoord. Desalniettemin kunnen dergelijke kristallen beschreven worden als periodieke variaties in een gegeven basisstructuur. In de meeste gevallen is de eenheidscel groter. In het geval van commensurabele modulatiegolven is de translatiesymmetrie niet verloren, maar slechts veranderd. De ruimtgroep van een dergelijk kristal is daardoor veranderd, maar nog steeds geschikt voor de beschrijving van de (nieuwe) fysische eigenschappen. Bekende voorbeelden zijn (anti-) ferroelectrische fasen en geordende magnetische structuren, als gemoduleerde vormen van een normale hoge temperatuur fase. Incommensurabele kristallen worden daarentegen gekarakteriseerd door additionele periodiciteiten die niet passen op het normale drie dimensionale rooster. Als gevolg is de translatiesymmetrie langs de richting van de modulatie verloren en hetzelfde geldt voor de ruimtgroep-symmetrie. De fysische eigenschappen verliezen dus een belangrijke mathematische beschrijving en bijgevolg een theoretische fundering. Desalniettemin suggereren vele van deze eigenschappen (bijvoorbeeld het röntgen diffractie patroon of de morfologie) de aanwezigheid van een belangrijke mate van symmetrie. Deze aanwijzing werd gebruikt bij de introductie van de zogenoemde superruimte-groepen die de symmetrie van incommensurabele fasen beschrijven. De essentie van de superruimte-beschrijving is een behandeling van de fase van de modulatie als aanvullende coördinaten in een hogere ($3 + d$) dimensionale ruimte. In het geval van een enkele modulatie geldt $d = 1$. De translatiesymmetrie van het rooster is hersteld in de superruimte en het is zelfs mogelijk om rotatie en spiegel symmetrieën te beschrijven. Op deze manier verkrijgt men ($3 + d$)-dimensionale ruimtgroepen (de zogenaamde superruimtegroepen) die de symmetrie van het kristal karakteriseren. Deze groepen blijken zeer geschikt om het röntgen diffractie patroon van dergelijke kristallen te beschrijven. Dit houdt in, dat ze in staat zijn om de complexe, structurele relaties in incommensurabele kristallen zeer efficiënt te beschrijven.

Het succes van het gebruik van superruimtegroepen voor de bepaling van de structuur van incommensurabele kristallen was een stimulans voor de bestudering van de consequenties voor andere fysische eigenschappen, zowel vanuit theoretisch als experimenteel oogpunt. Ook dit proefschrift is een gevolg hiervan. Het is verdeeld in drie hoofdstukken waarin verschillende fysische eigenschappen inzake optische en dynamische aspecten van gemoduleerde kristallen worden bestudeerd.

Hoofdstuk 2 behandelt de vibratie spectra met behulp van Raman en ver-infrarood spectroscopie. Deze beide technieken geven de mogelijkheid om de lange golflengte ($\mathbf{k} = 0$) optische fononen van kristallen te bestuderen. Tengevolge van de modulatie met golfvector $\mathbf{k} = \mathbf{q}$, zijn ook de fononen met $\mathbf{k} = n\mathbf{q}$ (n is een geheel getal) mogelijk actief in de Raman of infrarood spectra. Deze additionele modes zijn bestudeerd zowel in commensurabele als incommensurabele fasen, in twee diëlectrica namelijk Na_2CO_3 en $[\text{N}(\text{CH}_3)_4]_2\text{ZnCl}_4$.

Voor Na_2CO_3 is het volledige Raman spectrum in de β , γ en δ -fase bepaald. Daarnaast is het ver-infrarood spectrum in de γ en δ -fase gemeten. De spectra zijn geïnterpreteerd op grond van symmetrie en fenomenologische overwegingen. Voor de incommensurabele γ -fase is de superruimtegroep-symmetrie gebruikt. In deze fase zijn nieuwe modes gevonden en geanalyseerd. Bovendien zijn twee soft modes gemeten, waarvan er een tot de monoclien (β) naar incommensurabel (γ) faseovergang behoort. Deze mode is een zogenaamd amplitudon. Tenslotte is aangetoond dat de spectra van de δ -fase het bestaan van een lage temperatuur commensurabele (lock-in) fase impliceren.

Een generalisering van het gebruik van superruimtegroepen naar commensurabele fasen is bestudeerd in het geval van $[\text{N}(\text{CH}_3)_4]_2\text{ZnCl}_4$. Deze verbinding heeft evenals vele andere isomorfe A_2BX_4 verbindingen, naast een incommensurabele fase, verscheidene commensurabele fasen voor verschillende temperaturen. Voor sommige van deze commensurabele fasen is de superruimtegroep-symmetrie van de incommensurabele fase tot in zeer goede benadering nog aanwezig. De vraag is derhalve, of deze bijna behouden symmetrie ook in andere fysische eigenschappen weerspiegelt. In het bijzonder is dit bestudeerd voor de selectie regels voor Raman en infrarood spectra. Verder is aandacht besteed aan de domeinen in de commensurabele monocliene fasen. De relatief grote rotaties van de optische indicatrix in deze fasen zijn besproken in samenhang met de orthorhombische superruimte-symmetrie.

Onderwerp van hoofdstuk 3 is de klassieke optische activiteit in de verbinding Rb_2ZnBr_4 . In tegenstelling tot de optische activiteit van hoofdstuk 2, wordt hier de gyratie bedoeld, een effect waarbij de polarisatie van licht dat door een kristal gaat, draait om de voortplantingsrichting. De normale ruimtegroepen kunnen worden gebruikt om de gemeten effecten in de commensurabele fasen van Rb_2ZnBr_4 te beschrijven, terwijl voor de incommensurabele fase de superruimte-symmetrie nodig is. Een fenomenologische theorie, die zowel de diëlectrische als de gyratie eigenschappen van de incommensurabele fase kan beschrijven, wordt hier gepresenteerd. Om langgolelige structurele eigenschappen, die typisch zijn voor incommensurabele fasen, een rol te laten spelen in het diëlectrische en gyratie probleem, zijn de relevante tensoren in een Fourier decompositie beschreven. De toegestane Fourier componenten en hun symmetrie zijn gevonden, met behulp van de superruimtegroep. In het geval van de diëlectrische tensor zijn de elektrische velden bepaald in een benadering waarvoor, behalve de macroscopische bijdrage, nog twee Fourier componenten zijn meegenomen. Voor het gyratie effect is de vorm van de tensoren gebruikt om het optreden van een effect te voorspellen. De experimentele resultaten laten vervolgens zien welke termen mogelijk relevant zijn.

Hoofdstuk 4 behandelt de bestudering van de incommensurabele spindichtheidsgolf in incommensurabel chroom. Aangetoond wordt dat de stroomspannings karakteristiek van een punt-contact (met een diameter die kleiner is dan de gemiddelde vrije weglengte van de electronen) tussen twee metalen verandert tengevolge van kleine gaps in de toestandsdichtheid van de electronen in de buurt van de Fermi energie. De oorzaak van deze nieuwe gaps bij $2k = nq$ (n weer geheel) vormt de additionele periodiciteit van de spin dichtheidsgolf. De invloed van de gaps is hier bekeken binnen het kader van de vrije electron benadering. Het resultaat is gebruikt om de experimenteel waargenomen afname in de weerstand van een Cr-Cr puntcontact bij toename van kleine aangelegde spanningen te verklaren. De voor hogere spanningen (≥ 50 meV) weer toenemende weerstand is een gevolg van opwarmingseffecten. De grootte van de gap (≈ 110 meV) is vergeleken met resultaten van andere experimenten.

CURRICULUM VITAE

H.L.M. Meekes

- 15 januari 1959 Geboren te Lichtenvoorde.
- 1965-1971 Lagere school, Lichtenvoorde.
- 1971-1977 Ongedeeld VWO, gemeenschappelijke
Scholengemeenschap Doetinchem.
- 1977-1983 Studie Natuurkunde, Katholieke
Universiteit Nijmegen.
- maart 1983 Doctoraalexamen Experimentele Natuurkunde,
specialisatie Vaste Stof Fysica.
- 1983-1987 Promotieonderzoek in dienst van de Stichting
voor Fundamenteel Onderzoek der Materie (FOM)
in de Faculteit der Wiskunde en Natuurweten-
schappen, Katholieke Universiteit Nijmegen;
lid van werkgroep VSDN-N o.l.v.
Prof. Dr. A.G.M. Janner;
experimenteel werk o.l.v. Prof. Dr. P. Wyder
en Prof. Dr. H. van Kempen.

STELLINGEN

behorende bij het proefschrift

Optical and dynamical properties of modulated crystals

I

Computersimulaties tonen aan dat bij een spelletje monopoly de frequentie waarmee Kalverstraat bezet wordt duidelijk lager ligt dan het gemiddelde over alle straten, terwijl de gehele stad Utrecht significant boven dat gemiddelde uitsteekt. De oorzaak van de argwaan van veel spelers ten aanzien van Kalverstraat dient derhalve gezocht te worden in financieel-psychische gronden.

II

Scheiden van ferromagnetische deeltjes naar grootte of magnetisatie wordt in de conventionele magnetische scheidingstechnieken sterk bemoeilijkt door magnetisch geïnduceerde aggregatie. Het verdient aanbeveling de toepassingsmogelijkheden van een stroomvoerend filter te onderzoeken, waarin dit probleem door afwezigheid van een extern veld nauwelijks speelt.

M.R. Parker, IEEE Trans. Magn. MAG-17, 2816 (1983).

III

Het gebruik van standaard AC-technieken om de signaal-ruis verhouding te verbeteren bij de bepaling van de magnetoweerstand van metalen in een corbino geometrie verlaagt de meetnauwkeurigheid.

IV

De rol van meer-foton-overgangen bij de infrarood predissociatie van NH_3 -trimeren, gesuggereerd door vergelijking van de metingen van Huisken *et al.* met die van Snels *et al.*, kan worden onderzocht door middel van een hole-burning experiment met twee CW CO_2 -lasers. Op grond van berekende bindingsenergieën is één-foton-dissociatie onwaarschijnlijk.

M. Snels, R. Fantoni, R. Sanders en W.L. Meerts, Chem. Phys. 115, 79 (1987).

F. Huisken en T. Pertsch, Abstracts of XI-th International Symposium on Molecular Beams, Edinburgh.

V

Ver-infrarood reflectiometingen aan $Ga_{1-x}Al_xAs$ laten twee gescheiden optische fononen zien. Om de magneetveldafhankelijke effectieve massa m^* van het 2D-electrongas in GaAs-AlGaAs-heterojuncties voor energieën in de buurt van deze optische fononen te bepalen verdient het aanbeveling om ook geïnverteerd gegroeide preparaten te gebruiken.

O K Kim en W G Spitzer, J Appl Phys 50, 4362 (1979)

VI

Gezien de enorme problemen die automatische spraakherkenners nog hebben met de variatie in spraak, mag het een wonder heten dat mensen elkaar verstaan.

D B Pisoni, J Acoust Soc Am 78, 381 (1985)

VII

Het aanvankelijk overdadige en vaak fatale gebruik van röntgenstraling in de medische wetenschap zou remmend moeten werken op het gebezigde enthousiasme inzake kernspinresonantie technieken in de medische diagnostiek.

VIII

In hun pleidooi voor het gebruik van het stuperspace formalisme hebben Gates *et al*, over het hoofd gezien dat hun vergelijking (3 14159) nauwelijks afwijkt van het oppervlak van de eenheidskrans. Dit resultaat volgt overigens ook direct wanneer op hun eerste vergelijking de Meekes- ∇ -operator (∇) en de hermitisch toegevoegde (∇^\dagger) wordt losgelaten, met als resultaat

$$\nabla \frac{\sigma}{\rho} (\mathcal{L}) \otimes \nabla \otimes \nabla \stackrel{\text{Kroes}}{\text{Smit}} B Y Z \otimes \nabla = \nabla \otimes (R1) \cdot \nabla \approx \pi$$

V Gates, Empty Kangaroo, M Roachcock en W C Gall, Physica 15D, 289 (1985)

IX

De regels 750 en 760 van het begeleidende programma bij een EPROM programmeerder van H Meekes, alsmede deze stelling, duiden op een niet geringe mate van ijdelheid aanwezig bij deze auteur.

H. Meekes, 'Eprom programmeerder voor de CBM 64', R B Elektronika-Computers, 56(4), 43 (1987).

X

Indien Bach nog notie had kunnen hebben van het begrip incommensurabele structuur, dan had hij ongetwijfeld een zeventiende (incommensurabele) fuga aan *Die Kunst der Fuge* toegevoegd

XI

Het (kerk)orgel is het meest veelzijdige en mede daardoor het prachtigste muziekinstrument van de westerse beschaving

XII

Het Midas-effect

Het proefschrift waaraan deze stellingen zijn toegevoegd bevat precies 222 maal het woord *symmetry*. Het opwindende van dit getal is dat het de puntgroep zou kunnen zijn van de lock-in phase van veel A_2BX_4 -verbindingen (222 in plaats van $m2m$). Deze opwindende is zelfs op zijn plaats wanneer we, door de stellingen bij het proefschrift te betrekken, het resultaat tot de puntgroep 223 brengen

XIII

Afgaand op de hoge mate van vervorming in het geluid geproduceerd door de gangbare transistorradio's in de bouwvakwereld, zou men ten onrechte kunnen concluderen dat de bezitters van deze apparaten audiofielen zijn. Dit, gegeven de te verwachten extreem lage transient intermodulatie (TIM) vervorming bij de toegepaste geringe mate van tegenkoppeling in de eindversterker

XIV

Fysici die de noodzaak van een beperkt autogebruik denken te kunnen weerleggen met het argument dat een toename van het fietsverkeer gepaard gaat met een toenemende voedselconsumptie en dus energieverbruik, hebben een bijscholingscursus biofysica alsmede een bewuster eetgedrag broodnodig. *Nederlands Tijdschrift voor Natuurkunde* **A49**, 141 (1983)

XV

De kracht en invloed van de milieubeweging stijgt met een toenemend publiekelijk besef van de reden van deze toename. De kritische drempel voor de inherente (schone) kettingreactie is helaas nog niet bereikt

Hugo Meekes

